공학박사 학위논문

Synthesis, Characterization, and Application of Extremely Small-sized Iron Oxide Nanoparticles

극소 산화철 나노입자의 합성, 분석 및 응용

2013년 2월

서울대학교 대학원

화학생물공학부

김 병 효

Abstract

Synthesis, Characterization, and Application of Extremely Small-sized Iron Oxide Nanoparticles

Byung Hyo Kim
School of Chemical and Biological Engineering
The Graduate School
Seoul National University

Extremely small-sized nanoparticles, of size < 3 nm, have become important because their optical, magnetic, and catalytic properties are distinguished from those of large sized nanoparticles or molecules. Their properties are strongly dependent on their dimension, so the size-controlled synthesis of extremely small-sized nanoparticles is essential for further applications. Iron oxide nanoparticles are very important materials because of their interesting size-dependent magnetic properties. Extremely small-sized iron oxide

nanoparticles exhibit weak magnetization, and can be applied to biomedical applications.

The present work focuses on the large scale synthesis, characterization, and application of extremely small-sized iron oxide nanoparticles (ESIONs). The ESIONs were synthesized by thermal decomposition of iron-oleate complexes, and were applied as T_1 magnetic resonance imaging (MRI) contrast agents. Sizes and size distribution of the nanoparticles were characterized in an easy and precise way through matrix-assisted laser desorption/ionization - time-of-flight (MALDI-TOF) mass spectrometry.

Firstly, gram-scale synthesis of (ESIONs) was achieved by thermal decomposition of iron oleate complex in the presence of oleyl alcohol. Magnetization of small iron oxide nanoparticles was much less than that of large-sized nanoparticles due to their small magnetic moment and the spin canting effect. The small magnetic moment of the ESIONs enables them to be used as T_1 MRI contrast agents. ESION-enhanced *in vivo* MR imaging showed bright T_1 image which is maintained for a long time attributed to their moderate size.

Secondly, a rapid and reliable method to determine the sizes and size distributions of extremely small-sized iron oxide nanoparticles is presented using mass spectrometrometry. The mass spectra obtained from MALDI-

TOF mass spectrometry could readily provide size information using a simple equation. The size distribution obtained from the mass spectrum is well-matched with the data acquired from transmission electron microscope (TEM) which requires long and tedious analysis work. The size distribution from mass spectrum is highly resolved and is capable of detecting a difference in size of even few Angstroms. The mass spectrum technique was used for the investigation of formation mechanism of iron oxide nanoparticles. From *ex situ* measurements, it was observed that iron-oxo clusters were produced from the iron precursor, and eventually 3 nm iron oxide nanoparticles were achieved. The mass-to-size estimation will be found as easy and accurate analytical tool for various purposes including the formation mechanism studies to develop new synthetic methods for various kinds of nanoparticles with desired characteristics.

Keywords: iron oxide, nanoparticles, magnetic resonance imaging, mass spectrometry, formation mechanism.

Student Number: 2006-21331

Contents

List of Tables

List of Figures

Chapter 1. Introduction: Extremely Small-sized Nanoparticles

1.1 Introduction

Nanostructured materials, whose dimensions are within the range of 2 to 100 nm, have attracted a lot of attention not only for their size-dependent characteristics but also for their potential applications (Figure 1.1).[1] Nanomaterials show manyinteresting properties which cannot be observed in their bulk counterparts. For example iron oxide shows superparamagnetism and semiconductors exhibit quantum confinement and finite size effects in the nanometer range which are not observed by their bulk materials or molecules.[2] Nanoparticles with a size range of 1 and 3 nm have further gathered a lot of interest due to their exquisite properties. A small change in the particle size in this range induces a dramatic change in the particle volume and surface area, leading to highly size dependent physical properties, and thus opening a new area of research as “extremely small sized nanoparticles (ESNs)”. The ESNs lie between molecules and nanomaterials and therefore show intermediate structural, optical, electrical, catalytic and magnetic properties which have not been exhibited in either of them. For example,

extremely small-sized iron oxide nanoparticles are no longer superparamagnetic, rather show nearly paramagnetic behavior.[3] Extremely small sized gold nanoparticles exhibit fluorescence.[4] These unique properties make this field very intriguing. Some of these unique properties and applications are summarized in Figure 1.2.

Because of their size-dependent properties, accurate measurement of their size and size distributions is very important for both their fundamental property characterizations and their many technological applications. Furthermore, understanding the nanoparticle formation mechanism is very important to synthesize nanoparticles with the desired characteristics, and for critical control of size distribution.[5] However, it is difficult to measure size in this range (< 2 nm) with various conventional methods, including TEM.[6] Consequently in order to measure the infinitesimal dimension of these particles, unique characterization techniques which have not been used frequently in nanomaterials are introduced.

This chapter focuses mainly on the introduction of extremely small-sized nanoparticles of metals, metal oxides, and metal chalcogenides. Firstly, we discuss properties of extremely small-sized nanoparticles, which are very different from larger nanoparticles followed by the methods utilized for their synthesis. The last section would deal with the characterization methods.

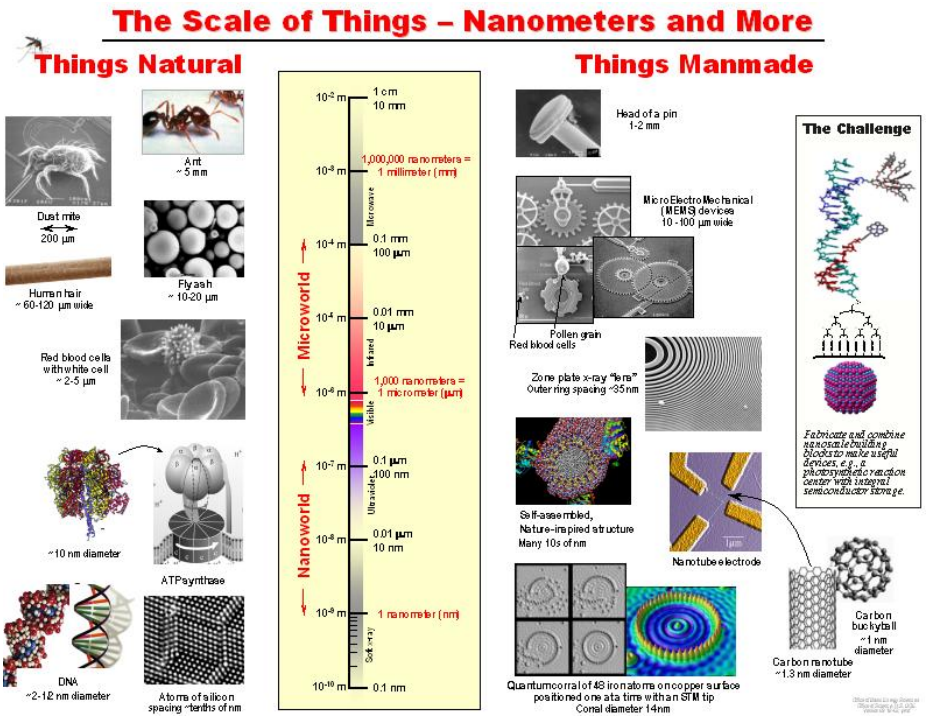

Figure 1.1 The scale of things. (National Nanotechnology Initiative, http://www.nano.gov)

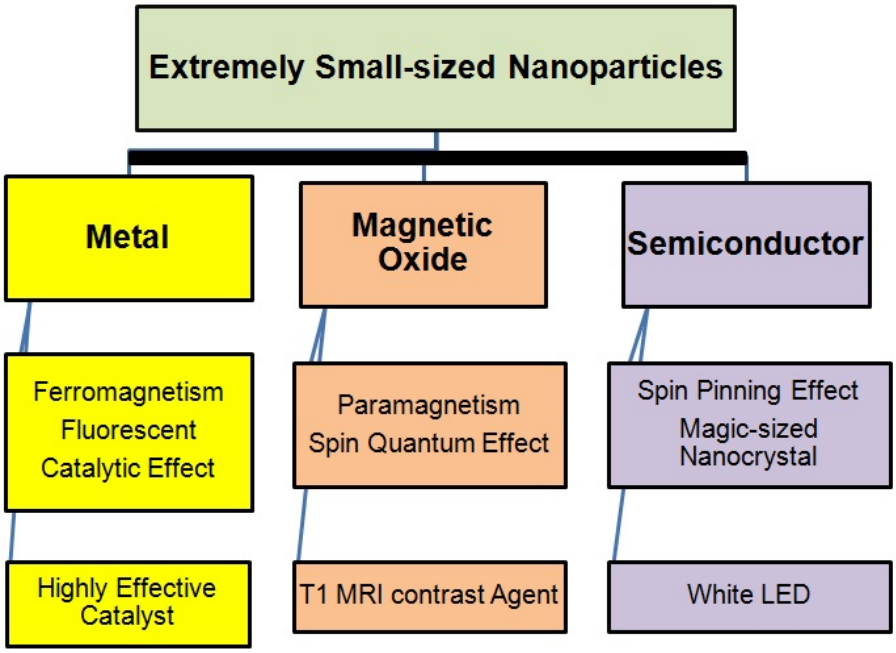

Figure 1.2 Schematic diagram of unique properties and application area of extremely small-sized nanoparticles.

1.2 Properties of Extremely Small-sized Nanoparticles

1.2.1 Volume Effect

When the size of a material decreases to 1 - 2 nm, which contains less than 200 atoms, it is regarded not only as small bulk materials, but also as large molecules.[7] Therefore, extremely small-sized nanoparticles (ESNs) lose their bulk properties, but the molecular properties or “quantum size effects” become dominant. The effects originate from the quantized energy level structure of the ESNs.[8] For example, extremely small-sized gold nanoparticles exhibit fluorescence instead of showing surface plasmon resonance;[4] extremely small iron oxide particles have quantized spin states.[9]

1.2.1.1 Fluorescence of Metal Nanoparticles

From ancient era, gold nanoparticles were used to create stained glasses for their beautiful color. It is only recently, after the development of nanoscience, that origin of the color was revealed, that is surface plasmon resonance. Coherent oscillation of conduction electrons in the metal nanoparticles induces surface plasmon resonance.[10] The plasmon energy depends on the size and shape of the nanoparticles.[11]However, extremely small-sized noble metal nanoparticles do not show surface plasmon resonance due to which they are no more classified as metals. When a metal is reduced to few nanometers, quatization of the energy levels takes place, leading to the formation of energy gap. Therefore, in the size range of 1 – 2 nm, metal nanoparticles exhibit optical activity.[12] The energy level spacing near the Fermi level for a nanoparticle were estimated by Kubo's statistical formula,[13]

$$\delta = \frac{E_F}{Nz} \qquad \text{(Eq. 1.1)}$$

where δ is energy level spacing near the Fermi energy, E_F is Fermi energy, N is the number of metal atoms in the particle, and z is the valency. In the case of gold, when number of atoms is less than 400 (D < 2.5 nm), the energy level spacing exceeds the thermal energy at room temperature.[14]

1.2.1.2 Spin Quantum Effect

Extremely small-sized iron oxide nanoparticles, in the size range of 1 - 3 nm, show a blocked magnetization at low temperature and a stepped magnetic hysteresis like molecular magnets (ex: Fe_8O_2, $Mn_{12}O_{12}$ oxo clusters).[15] The stepped magnetic hysteresis demonstrated that the spin states of extremely small-sized iron oxide nanoparticles are quantized due to their extremely small volume. (Figure 1.3) The phenomenon is the proof of coexistence of quantum and classical effects in the ESNs.

Recently, electron magnetic resonance (EMR) studies also confirmed spin quantum effect of extremely small-sized iron oxide nanoparticles.[16] The Gatteschi group synthesized extremely small-sized iron oxide nanoparticles in the cavity of ferritin type protein.[17] The EMR spectra of ESNs have a unique temperature behavior very similar to that of iron-oxo clusters.[18] As the temperature decreases, the width of the main resonance of ESNs increases due to reduced thermal averaging. Interestingly, the ESNs presented a half-field signal in the EMR spectrum which is known for iron-oxo clusters. The half-field signal cannot be explained by classical model, but can only be interpreted as a signature of discrete energy levels, showing spin quantum effect.

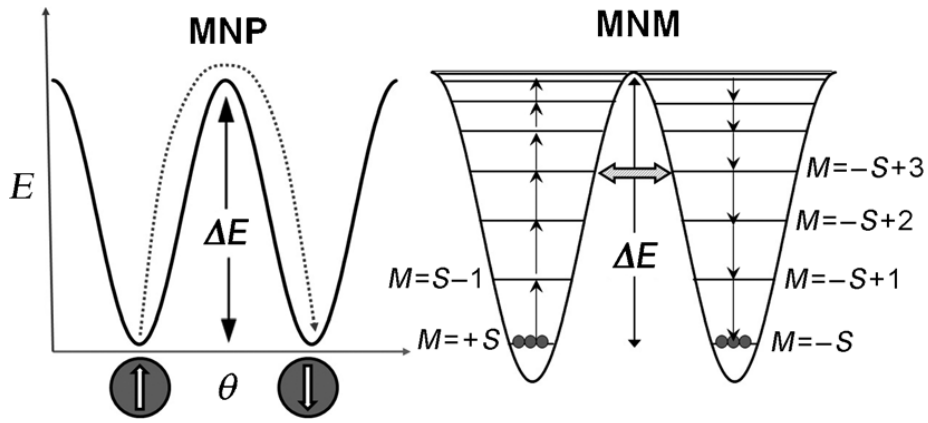

Figure 1.3 The relationship between the barriers to the magnetization reorientation of magnetic nanoparticles (left) and molecular nanomagnet (right). (from Ref. [14], Gatteschi, D.; Fittipaldi, M.; Sangrido, C.; Sorace, L. *Angew. Chem. Int. Ed.* **2012**, *51*, 4792)

1.2.2 Surface Effect

When the particle size is decreased to few nanometers, the surface area of the particle dramatically increases. In addition, surface to volume ratio (i.e. the ratio between the surface atoms and total atoms) increases dramatically with decreasing particle size. In Figure 1.4, the number of surface atoms in 1.2 nm palladium nanoparticles is 96% while that in 3.1 nm nanoparticle is only 31%.[19] The trend shows that the macroscopic properties of ESNs are highly affected by the properties of their surface.

Large portion of surface atoms in ESNs induces unique size-dependent physical properties. For example, extremely small-sized gold nanoparticles exhibit ferromagnetism[20] and extremely small-sized CdSe nanoparticles show white light emission by deep traps.[21] Moreover, the electronic structures of ESNs are different from the bulk because of their different surface local states .[22]

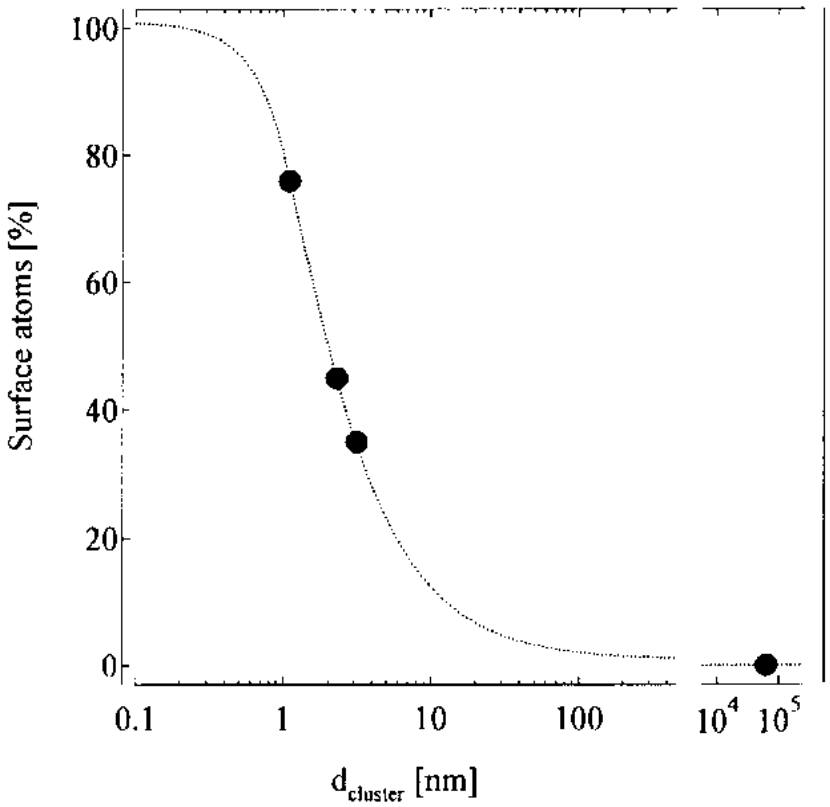

Figure 1.4 The percentage of surface atoms changes with the palladium particle diameter. (from Ref. [19], Neutzenadel, C.; Zuettel, A.; Chartouni, D.; Schmid, G.; Schlapbach L. *Eur. Phys. J. D* **2000,** *8*, 245)

1.2.2.1 Ferromagnetism at Metal Surface

Materials are categorized on the basis of their magnetic properties as diamagnetic, paramagnetic, ferromagnetic, antiferromagnetic, and ferrimagnetic.[23] In paramagnetic materials unpaired electrons are usually attracted to the direction of magnetic field because electron spin is likely to align in the direction of magnetic field by Zeeman effect. Ferromagnetic, ferrimagnetic, and antiferro-magnetic materials also have unpaired electrons but they show exchange coupling of spin element.[23] Spins of ferromagnetic materials are assembled parallel to each other so the materials have strong magnetic moment. Even after removal of magnetic field, the magnetic moments still remained on account of large exchange energy. Iron, cobalt, nickel and their alloys are representative ferromagnetic materials, and iron oxide (maghemite or magnetite) is ferrimagnetic material. On the other hand, the materials having lack of unpaired electrons show diamagnetic properties and so are repulsed by a magnetic field.

Group 11 metals (gold, silver, and copper) are well-known diamagnetic meterials. Recently, ferromagnetic properties are observed in extremely small-sized thiol-capped gold nanoparticles.[24-26] There are two different explanations for the phenomenon. One is quantum effect and the other is surface effect.

When the spin-orbit coupling is weak, the magnetic susceptibility of ESNs containing odd number of electrons follow Curie's law induced from an unpaired electron of highest occupied state.[8]

$$\chi = \frac{\mu^2}{kT} \qquad \text{(Eq. 1.2)}$$

where χ is susceptibility, μ is the Bohr magneton, k is Boltzman's constant, and T is temperature.

However, extremely small-sized gold nanoparticles stabilized by weak interactive surfactants are diamagnetic like bulk gold.[25] Consequently, surface effect is more plausible for explaination of ferromagnetism in metal nanoparticles. Ferromagnetism can be associated with thiol ligand which can induce 5*d* localized holes. These holes cause localized frozen magnetic moments due to the symmetry reduction from two types of bonding (Au-Au and Au-S) and strong spin-orbit coupling. The Fernandez group reported ferromagnetic properties of thiol capped 1.4 nm gold nanoparticles. The spin ordering is explained by local structure of gold-sulfur bond (Figure 1.4).[24] Extremely small silver and copper nanoparticles also exhibit ferromagnetism.[26] Likewise, extremely small-sized CdSe nanoparticles show paramagnetism.[27]

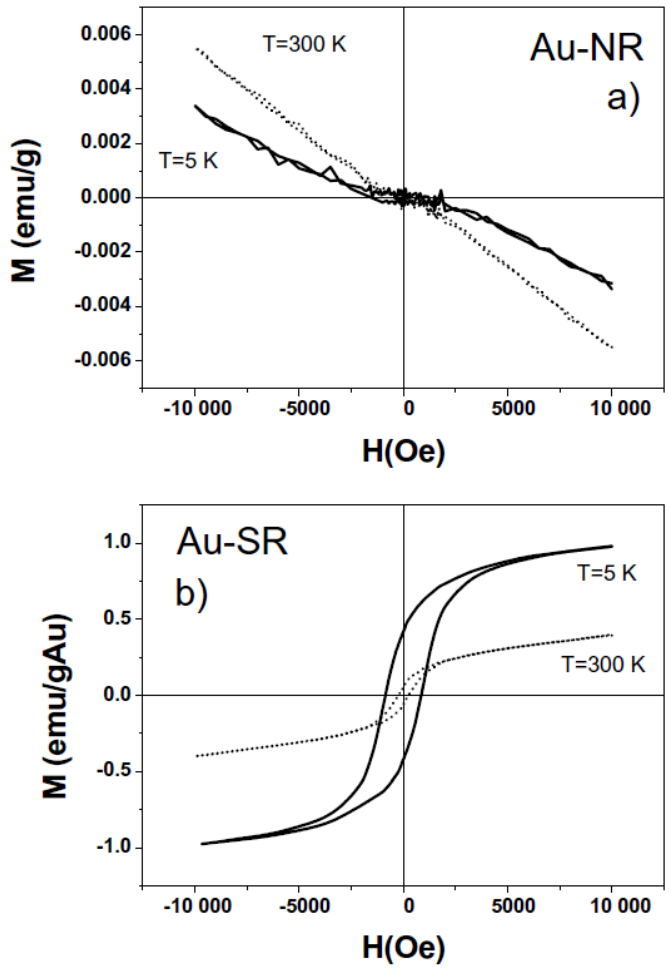

Figure 1.5 Magnetization curves of (a) 1.4 nm amine-capped-, and (b) thiol-capped gold nanoparticle, at 5 and 300 K. (from Ref. [25], Crespo, P.; Litran, R.; Rojas, T. C.; Multigner, M.; de la Fuentes, J. M.; Sanchez-Lopez, J. C.; Garcia, M. A.; Hernando, A.; Penades, S.; Pernandez, A. *Phys. Rev. Lett.* **2004,** *93,* 087204)

1.2.2.2 Paramagnetism of Magnetic Nanoparticles

Metal ferrite is one of the most widely used magnetic materials due to its abundance, low price, and ferrimagnetic properties. Nanosized iron oxide materials show size-dependent superparamagnetic properties by Neel and Brown relaxation induced by thermal fluctuation when the thermal energy exceeds anisotropic energy.[28,29] On the other hand, spins of surface atoms are disordered due to different state of surface atoms as compared to the bulk atoms (Figure 1.6). The effect is called 'spin canting effect' and the thickness at which the effect occurrs is about 0.5 ~ 0.9 nm for maghemite.[30-32] Therefore, magnetic nanoparticles can be considered core/shell structures which is composed of magnetic core and non-magnetic shell. Due to the small magnetic core fraction of entremely small-sized magnetic nanoparticles they have small saturation magnetization as compared to large sized nanoparticles. Assuming that the thickness of the spin canted layer is 0.9 nm,[31] extremely small-sized iron oxide nanoparticles of < 1.8 nm-size become almost paramagnetic because almost all spins of the particle are disordered. The new property of extremely small-sized iron oxide nanoparticles are expected to open up new application areas. The Hyeon group reported that 1.5, 2.2, and 3 nm-sized maghemite nanoparticles show

weak magnetic properties. Even at room temperature, 1.5 nm particles show paramagnetism.[3]

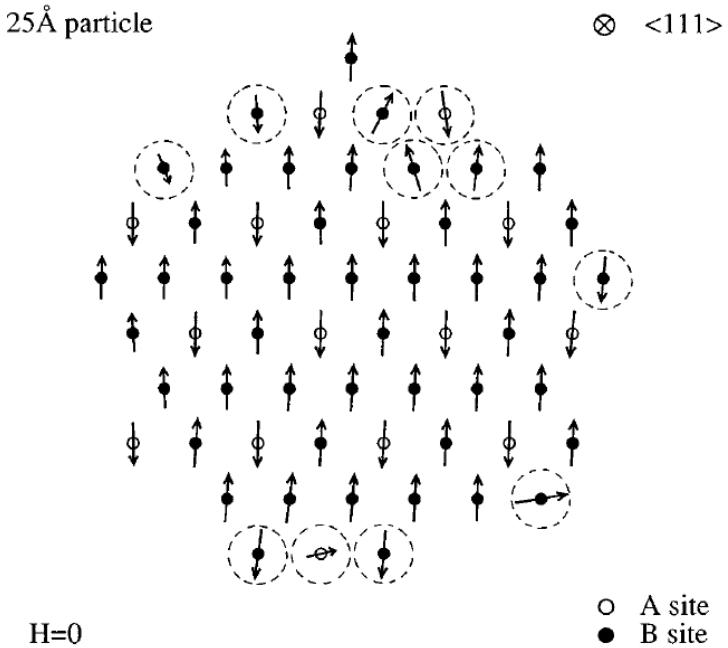

Figure 1.6 Calculated spin configuration at zero field for a cross section of a 2.5 nm nickel ferrite particle. Highly misoriented spins are circled. (from ref [32], Kodama, R. H.; Berkowitz, A. E.; McNiff, Jr, E. J.; Foner, S.; *Phys. Rev. Lett.* **1996,** *77*, 394)

1.2.2.3 Chemical Properties

ESNs can be used as catalysts because of their enormously large surface area.[33] In addition to their large surface area, their different electronic and molecular structures prove to be advantageous for catalytic applications.

Electronic structure of ESNs are different from larger sized nanoparticles, inducing different chemical reactivity.[34] Molecular structures of ESNs are also changed from their bulk counterparts. For example, gold in bulk and > 2 nm nanoparticles have face-centered cubic (fcc) structure. But this fcc structure collapses at sufficiently small size. Accordingly, their physicochemical properties will be altered.[35] Tuning the electronic structure by varying the size, catalytic effect can be optimized. Many catalytic studies revealed that the catalytic activity of metal nanoparticles of size < 2 nm is greatly enhanced.[34]

1.2.2.4 Ligand pinning Effect

The Rosenthal group reported that extremely small-sized quantum dots show a strong Stokes shift and broad emission covering the entire visible spectrum. These properties are due to extremely large surface area.[36] The white emission is originates from the interaction of electrons and holes at the nanocrystal surface. Therefore, these nanoparticles provide an ideal platform to study the nanocrystal-molecule transition. Furthermore, the combination of their intrinsic properties makes them an ideal material for solid state lighting applications.

1.3 Synthetic Methods of Extremely Small-sized Nanoparticles

The Smalley group found fullerene by cluster beam method which has size between 1 - 2 nm.[37] After the successful discovery of fullerene, many researchers found ESNs such as magic-sized gold clusters using the cluster beam method.[38] Theoretical calculations predicted the stable structure of the clusters and the result is well-matched with the experimental findings.[39] However, using cluster beam method very small amount of polydisperse clusters are generally produced.

In the extremely small-size regime, size dependency is more prominent. For example in the case of extremely small-sized gold nanoparticles, even adding one gold atom induces significant change in its structural, optical and electrical properties.[19] The extreme size-dependency shows the importance of size uniformity of ESNs. Collodial chemistry-based nanoparticle synthetic methods have been developed for the last two decades due to their advantages of monodispersity, controllability, and large scale production.[40] In this manner, uniform extremely small-sized nanoparticles of metals, metal oxides and semiconductors could be synthesized based on colloidal chemistry approach.

1.3.1 Extremely Small-sized Metal Nanoparticles

Many researchers found that bare gold clusters having closed shells are stable. The stable clusters were obtained using cluster beam method, such as Au_{13} (n=2), Au_{55} (n=3), Au_{147} (n=4).[41] However, the cluster beam method cannot produce uniform-sized clusters. Uniform extremely small-sized gold nanoparticles could be synthesized using phosphine ligands.[42] However, the synthetic method for the phosphine-stabilized gold particles was cumbersome, requiring rigorously inert conditions and use of labile diborane as a reducing agent. As a result, phosphine-stabilized gold nanoparticles are not used since the development of thiol-stabilized gold nanoparticles method, which is more convenient and scalable. This synthetic method is called Brust-Schiffrin methodin which gold precursor $HAuCl_4$ is reduced by $NaBH_4$ in the presence of dodecanethiol ligand, resulting in < 5 nm-sized gold nanoparticles (Figure 1.7).[43]

Since Brust and Schiffrin's pioneering work, tremendous scientific research on thiol-stabilized extremely small-sized gold nanoparticles has been carried out. Au_{25},[44] Au_{38},[45] Au_{40},[46] , Au_{68},[47] Au_{102},[48] Au_{144},[49] and Au_{333} (Figure 1.8)[50] were obtained by modifying Brust-Schiffrin's method.

The Crooks group reported the synthesis of nearly monodisperse gold nanoparticles by a dendrimer templating approach. Dendrimer-encapsulated

gold nanoparticles were prepared within poly(amidoamine) (PAMAM) dendrimers and had sizes of 1.3 or 1.6 nm.[51]

Contrary to gold nanoparticles, synthetic schemes for other extremely small-sized metal nanoparticles, such as silver, platinum, palladium, have been rarely reported.[52-56] The Hyeon group reported the synthesis of uniform extremely small-sized silver nanoparticles by reducing silver nitrate by oleylamine in the presence of oleic acid.[52] This method is simple and easy to scale-up to gram scale. The formation process of silver nanoparticles in this synthetic reaction was investigated by UV/Vis and fluorescence spectroscopy, TEM and MALDI-TOF mass spectrometry. The characterization data revealed that extremely-small-size could be achieved by kinetic control of the formation of silver clusters.

The Miyake group reported a simple synthetic method for extremely small-sized platimum nanoparticles by alcohol reduction in the presence of protective polymer, poly(*N*-vinyl-2-pyrrolidone) (PVP).[54] The size of the nanoparticles can be controlled from 1.9 to 3.3 nm by changing the type of alcohol or the concentration of reagents. Smaller nanoparticles can be achieved by increasing concentration of alcohol in water or increasing the amount of PVP. The Huang group reported the synthesis of monodisperse extremely small-sized platinum nanoparticles, in aqueous solution at room

temperature, with peptide molecules as stabilizers.[55] The specifically selected peptide molecule is able to bind to the surface of platinum nanoparticles and regulate nucleation and growth rate. Monodisperse platinum nanoparticles with a size from 1.7 to 3.5 nm were achieved. Palladium nanoparticles having 7-8 atom shells were achieved by reducing palladium(II) acetate by hydrogen in acetic acid solution in the presence of ligands.[56]

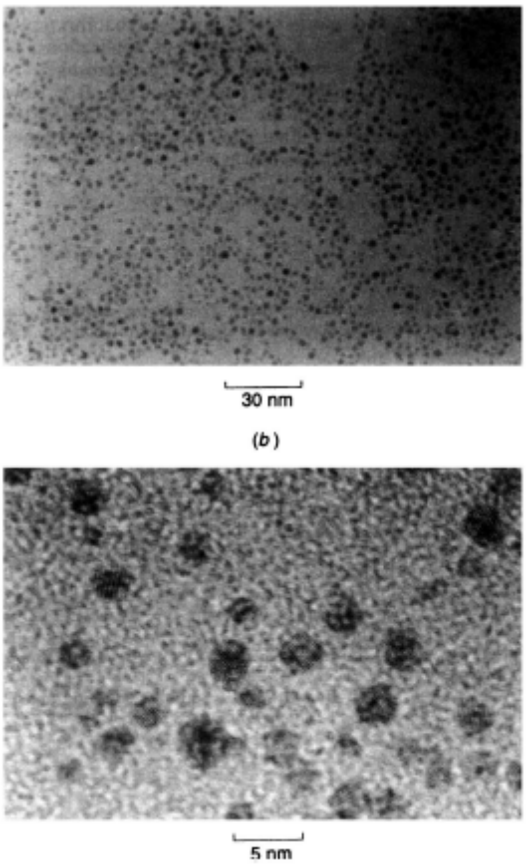

Figure 1.7 TEM pictures of the thiol-stabilized gold nanoparticles at (upper) low and (below) high magnification (from Ref. [43], Brust, M.; Walker, M.; Betheil, D.; Schiffrin, D. J.; Whyman, R. *J. Chem. Soc., Chem. Commun.* **1994**, 801)

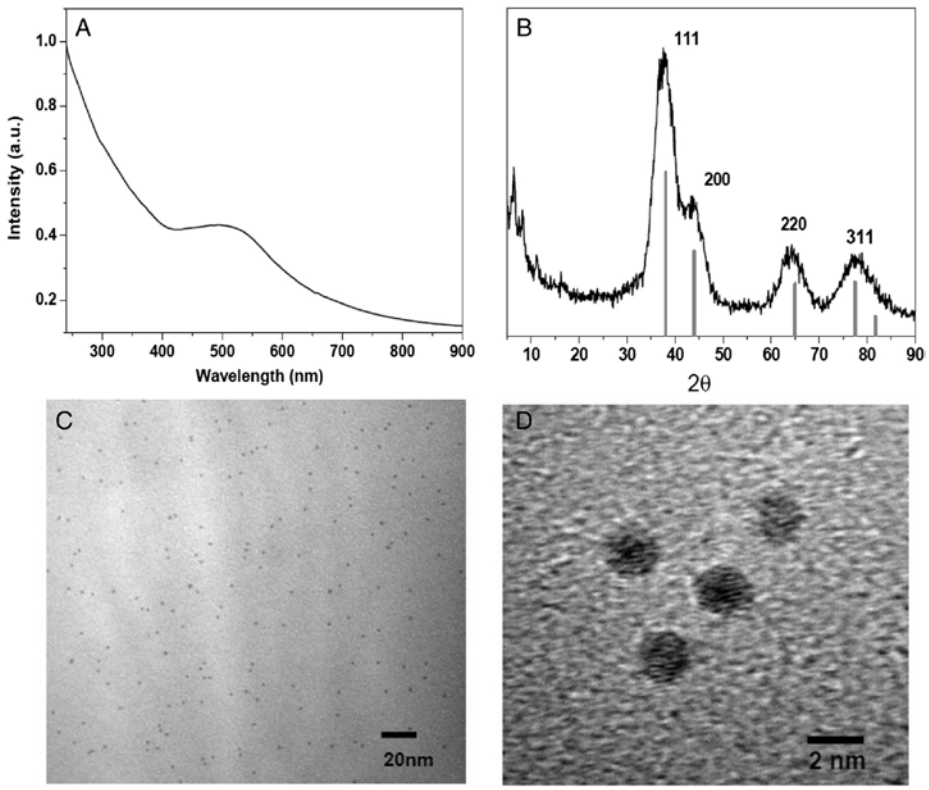

Figure 1.8 (a) UV-vis absorption spectrum, (b) powder X-ray diffraction pattern, (c) TEM, and (d) HRTEM images of $Au_{333}(SR)_{79}$ nanoparticles. (from Ref. [48], Qian, H.; Zhu, Y.; Jin, R. *Proc. Natl. Acad. Sci. U.S.A.* **2012,** *109*, 696)

1.3.2 Extremely Small-sized Metal Oxide Nanoparticles

There are very few reports on extremely small-sized iron oxide nanoparticles.[3,57-63] Several different procedures have been proposed, including the use of thermal decomposition,[3,57,58] polyol process,[59,60] precipitation in constrained media,[61] coprecipitation,[62] and reverse micelle method.[63] The Chaudret group reported a method in which, starting from an organometallic precursor [$Fe\{N(SiMe_3)_2\}_2$] and using amines as stabilizer, reasonably monodisperse maghemite particles of ~ 2.8 nm diameter were obtained.[57] The estimated dimensions correspond to approximately 420 iron ions for a spherical nanoparticle.

The Hyeon group reported synthetic method for large-scale and monodisperse extremely small-sized iron oxide nanoparticles by thermal decomposition of iron-oleate complexes in the presence of oleyl alcohol at relatively low temperature of about 250 ^oC.[3] When the thermal decomposition reaction occurred with only precursor and surfactant without oleyl alcohol, only large ~10 nm sized particles could be obtained. *Ex-situ* experiments revealed that alcohol acts as mild reductant and lower the reaction temperature, producing large amount of nuclei. The size reduction can be explained by the fact that one nuclei shares only small amount of monomers and the nuclei are abundant.

The Gatteschi group presented 1.8 nm-sized maghemite nanoparticles by precipitation in constrained media.[61] The extremely small-sized iron oxide nanoparticles were formed in the tiny oligosaccharide cyclodextrin and remain entrapped in the oligosaccharide host. HR-TEM image showed that the occurrence of nearly monodisperse particles with average diameter of 1.8 nm.

The Lee group developed a simple synthesis of extremely small-sized oxide nanoparticles with an average particle diameter of 1.7 nm in a polar organic solvent.[59-60] Nearly monodisperse 1.7 nm iron oxide[59] and 1.5 nm gadolinium oxide[60] nanoparticles were synthesized in triethylene glycol which were highly water-dispersible. The extremely small-sized oxide nanoparticles were tested for use as MRI contrast agents and showed high r_1 relaxivity.

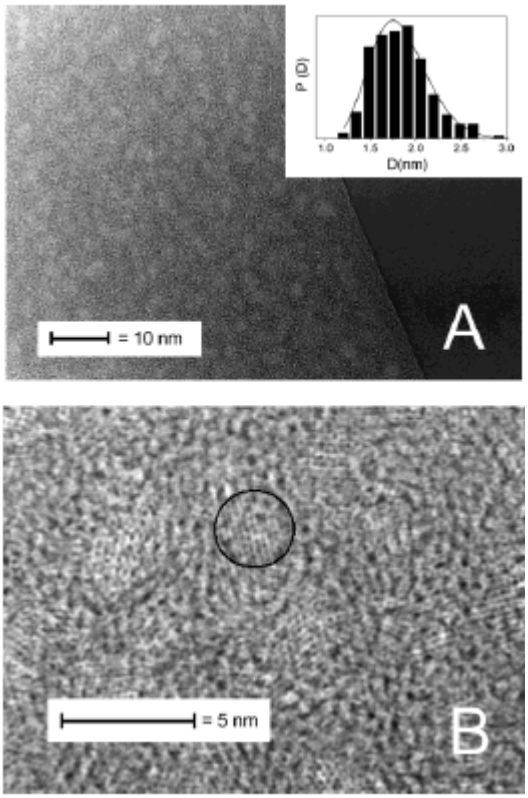

Figure 1.9 (a) HR-TEM micrographs showing the occurrence of a uniform distribution of almost identical, well-separated nanoparticles (b) andthe crystalline order of each particle. The size distribution obtained from a statistic over 210 particles is shown in the inset. (from Ref [61], Daniele Bonacchi, D.; Caneschi, A.; Dorignac, D.; Falqui, A.; Gatteschi, D.; Rovai, D.; Sangregorio, C. Sessoli, R. *Chem. Mater.* **2004**, *16*, 2016)

1.3.3 Extremley Small-sized Chalcogenide Nanoparticles

In the early stage of quantum dot growth, extremely small-sized chalcogenide nanoparticles, which have thermodynamically stable structure and are referred as magic-sized clusters, were generated and they tend to keep their morphology. [64] The remarkably stable energy of magic size nanocrystals make them having an narrow band width and exhibiting quantized growth. Recently, many kinds of magic-size nanoparticles have been synthesized.[65-67]

The Manna group reported the synthesis of CdSe magic sized nanocrystals by reacting mixture of cadmium oxide in dodecylamine and nonanoic acid with stock solution of selenium in trioctylphosphine. The temperature was kept low to ensure slow nucleation and growth. The optical spectra of aliquots taken during the synthesis showed well-defined discrete absorption peaks (Figure 1.6). The unique absorption spectra for magic-size CdSe indicated the existence of a pronounced nanocrystalline phase.[66] CdTe, PbSe, CdS magic-size nanocrystals were also observed during the slow formation process by *ex situ* optical spectroscopy.[67]

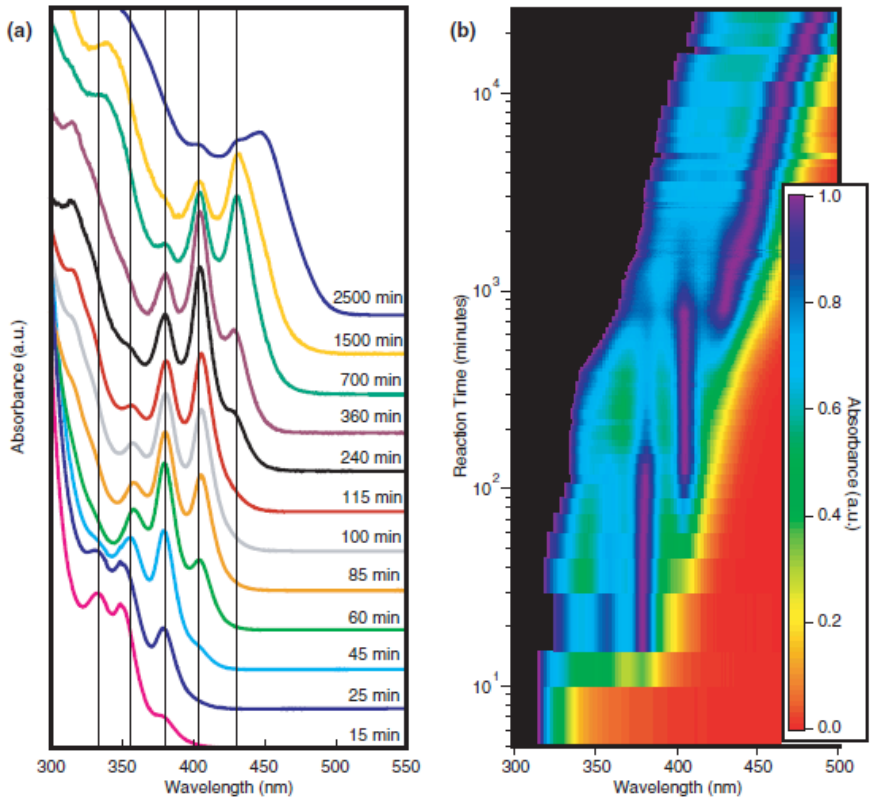

Figure 1.10 (a) Absorption spectra of the growth solution recorded at different times and containing different populations of magic-sized nanocrystals. (b) This graph is built by stacking several horizontal stripes on top of each other, each of which corresponds to a color-coded plot of an optical-absorption spectrum, which were collected at progressively longer reaction times. (from Ref. [65], Kudera, S.; Zanella, M.; Giannini, C.; Rizzo, A.; Li, Y.; Gigli, G.; Cingolani, R.; Ciccarella, G.; Spahl, W.; Parak, W. J.; Manna, L. *Adv. Mater.* **2007,** *19,* 548)

1.4 Characterization of Extremely Small-sized Nanoparticles

Precise measurment of nanoparticle sizes and their distributions is very important for both fundamental size-dependent property characterizations and many technological applications because nanoparticles exhibit characteristic size-dependent electrical, optical, magnetic, and chemical properties.[68] The spatial resolution of these techniques should be applicable to angstrom scale, but the accuracy of the generally used techniques has some deviations when used for the ESNs. There are not many reports on the determination of the exact size information of ESNs by enhancing spatial resolution.

1.4.1 Microscopy

TEM is the most popularly employed technique to measure the size of nanoparticles, but it is very difficult to obtain high-quality TEM images of nanoparticles of < 2 nm.[69] The Alivisatos group introduced a new type of liquid cell for *in situ* TEM based on entrapment of a solution between layers of graphene.[70,71] The graphene liquid cell facilitates atomic-level resolution

imaging. The liquid cell was employed to track the growth mechanism of platinum nanoparticles. (Figure 1.11) The Palmer group determined the size of thiol-capped extremely small gold nanoparticles via quantitative HAADF-STEM image.[72] In spite of the successful measurement by high resolution TEM, it is still difficult to obtain high-quality TEM images of nanoparticles of < 2 nm.

Scanning tunneling microscopy (STM) is a type of high-resolution scanning probe microscopy based on the concept of quantum tunneling.[73] Spatial information is acquired by scanning the quantum current with the position of tip. The STM shows a resolution as low as 0.1 nm. Individual atoms within nanomaterials can be routinely imaged with this resolution (Figure 1.12).[74] Atomic force microscopy (AFM) is another type of high-resolution scanning probe microscopy, which demonstrate resolution of the order of fractions of a nanometer. However, scanning probe microscopy, such as STM or AFM is a challenging instrument because it requires extremely stable and clean surfaces, stringent vibration control and sharp tips.

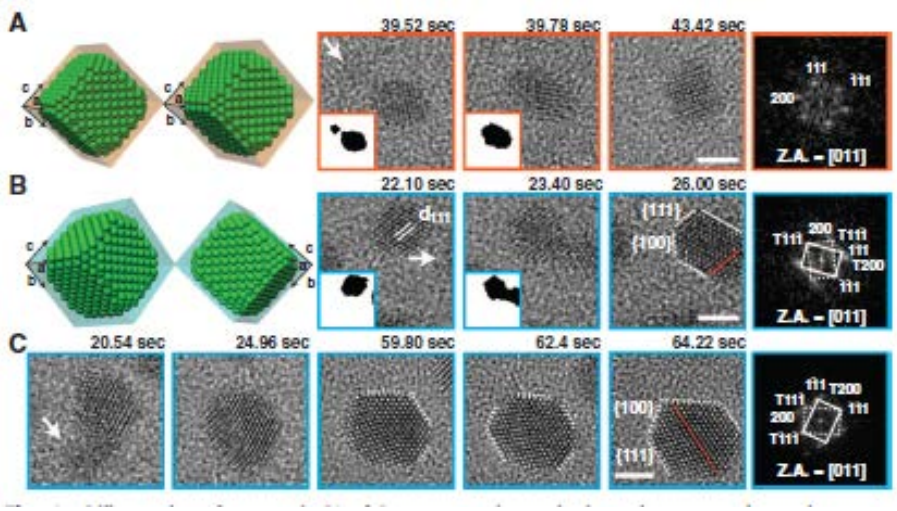

Figure 1.11 *In-situ* TEM images of Pt nanoparticle growth via coalescence and crystal-structure evolution observed with atomic resolution in a grapheme liquid cell. Schematic illustrations and corresponding TEM images exhibiting nanoparticle coalescence along the <111> direction, evolving into (a) a single crystalline face-centered cubic (fcc) structure or (b) a twinned (dotted line) fcc structure. (c) Shape evolution of the Pt nanoparticle by straightening of the twin boundary (dotted line) and evolution toward a hexagonal shape. The rightmost panel in each sequence shows a FFT of the panel adjacent to it. White arrows denote incoming small nanoparticles (as seen in insets). Scale bars, 2 nm. Z.A.: zone axis. (from Ref. [71], Yuk, J. M.; Park, J.; Ercius, P.; Kim, K.; Hellebusch, D. J.; Crommie, M. F.; Lee, J. Y.; Zettl, A.; Alivisatos, A. P. *Science* **2012**, *336*, 61)

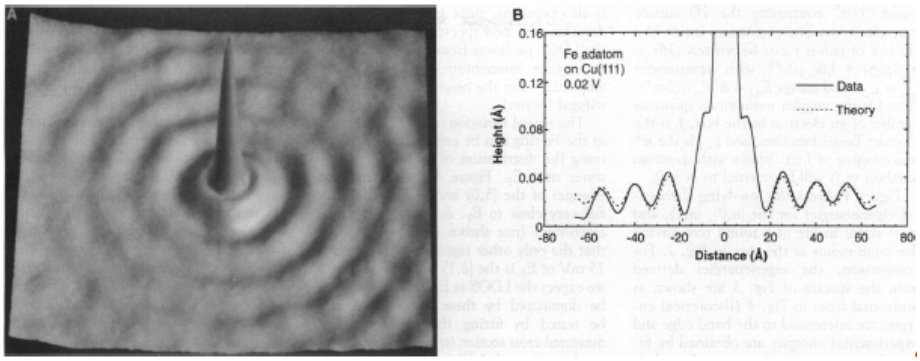

Figure 1.12 (a) Constant current 13 nm x 130 nm image of an iron adatom on the Cu(111) surface (V= 0.02 volt, I = 1.0 nA). The apparent height of the adatom is ~0.09 nm. The concentric rings surrounding the iron adatom are standing waves due to the scattering of surface state electrons with the iron adatom. (b) Average of three cross sections taken through the center of the iron adatom image in (a). (from Ref. [74], Crommie, M. F.; Lutz, C. P.; Eigler, D. M. *Science* **1996**, *262*, 218)

1.4.2 Mass spectrometry

Mass spectrometer (MS) is a widely used instrument for measuring accurate molecular mass by ionizing the sample and sorting by the mass-to-charge ratios.[75] Since particle size is proportional to cube root of mass, the size can be calculated from the mass measured with MS. To measure the mass of nanoparticles, nanoparticles should not decompose during the measurement and range of measurement should be able to cover heavy mass range. Matrix-assisted laser desorption/ionization (MALDI), laser desorption/ionization (LDI), and electro-spray ionization (ESI) techniques are so soft that the particles can be kept from fragmentation during the ionization step. Time-of-flight (TOF) analyzer can cover infinite mass range, theoretically. Taken the advantage of MALDI or ESI for ionization and TOF for detection, MALDI-TOF or ESI-TOF MS is the most appropriate method for characterizing extremely small-sized nanoparticles.

The Whetten group used laser desorption ionization mass spectrometry (LDI-MS) to identify the smallest fraction of gold nanoparticles obtained by the Brust-Schiffrin method (Figure 1.13).[76] After the pioneering work of the Whetten group, the extremely small-sized gold nanoparticles were characterized by MALDI-TOF, LDI-TOF, ESI-TOF mass spectrometry.[77]

The Strouse group presented a methodology for mass and size analysis by MALDI-TOF mass spectrometry of 2.5-3.7 nm ZnS nanoparticles. The results correlated with size information obtained from TEM and absorption spectroscopy.[78]

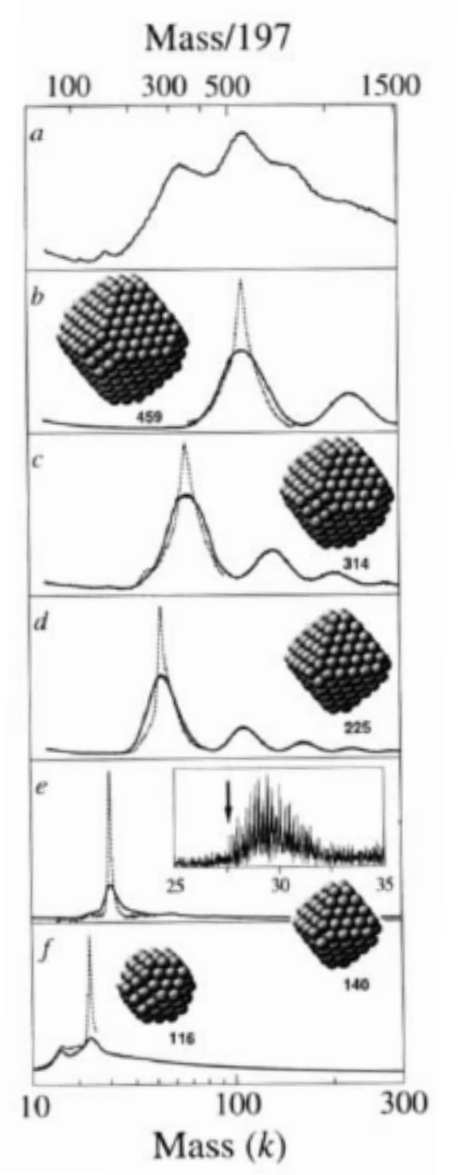

Figure 1.13 Mass spectra (mass, in k=10^3 Da, and in mass equivalent number *N* of gold atoms, m_{Au}= 197 Da) for crude (a) mixture and (b-e) separated fractions of gold nanoparticles passivated by dodecane-thiolate monolayers. The inset structures are predicted optimal core structures. (from Ref [76], Whetten, R. L. *et al. Adv. Mater.* **1996,** *8,* 428)

1.4.3 Other Characterization Methods

As seen in Figure 1.10, UV-vis absorption spectroscopy is most powerful instrument to characterize semiconductor materials. Since the band gap of semiconductor nanoparticles change with their size, size of the particles can be easily determined by their absorption and emission wavelength.[79] In this regard, sizes of the extremely small semiconductor nanoparticles are well-defined by UV-vis spectroscopy and photoluminescence.[64-67] Interestingly, the extremely small-sized metal nanoparticles also absorb visible light, not by the surface plasmon but by their semiconductor properties.[12]

The Wilcoxon group reported high-pressure liquid chromatography (HPLC) studies of the size distribution of extremely small-sized gold nanoparticles. HPLC is sensitive enough to distinguish changes in hydrodynamic diameter corresponding to metal core size changes of less than 0.4 nm.[69]

1.5 Dissertation Overview

Extremely small-sized nanoparticles, of < 3 nm, become important materials because the optical, magnetic, and catalytic properties of the nanoparticles are distinguished from those of molecules or large sized nanoparticles. Their properties are strongly dependent on their dimension, consequently synthesis of uniform-sized extremely small-sized nanoparticles is essential for further applications. Iron oxide nanoparticles are important materials because of versatile application area such as magnetic resonance imaging (MRI) by using their interesting size-dependent magnetic properties. The current thesis focuses on the large scale synthesis, characterization and application of extremely small-sized iron oxide nanoparticles (ESIONs). The ESIONs are synthesized by thermal decomposition of iron-oleate complex, and were applied to T1 MRI contrast agent. Sizes and size distributions of ESIONs were determined in easy and precise way through MALDI-TOF mass spectrometry.

Dissertation is composed of two parts. The first part (Chaper 2) represents the facile and large-scale synthesis of uniform, ESIONs and their successful applications to T1 MRI contrast agent and high resolution blood pool MR imaging. Gram-scale synthesis of ESIONs was achieved by thermal decomposition of iron oleate complexes in the presence of oleyl alcohol.

Magnetization of small nanoparticles was much less than that of typical iron oxide nanoparticles of > 5 nm due to spin canting effect. The small magnetic moment of the ESIONs enables to apply them as T_1 MRI contrast agent. ESION-enhanced *in vivo* MR imaging showed bright T_1 effect and maintained for a long time attributed to their moderate size.

The second part (Chapter 3) presents a rapid and reliable method to determine the sizes and size distributions of ESIONs through mass spectrometrical measurement. The mass spectra obtained from matrix-assisted laser desorption/ionization—time-of-flight (MALDI-TOF) mass spectrometry (MS) could be readily converted to size information using a simple equation. The size distribution converted from the mass spectrum is well matched with the data from TEM that requires long and tedious analysis work. The size distribution from mass spectrum is highly resolved and detecting the difference of only few angstrom in the size. The mass spectrum technique was investigated for the formation process of iron oxide nanoparticles. From *ex situ* measurements it was observed that iron-oxo clusters were produced from the iron precursors, and final 3 nm-sized iron oxide nanoparticles were achieved.

1.6 References

[1] (a) Klabunde, K. J. *Nanoscale Materials in Chemistry*, Wiley-Interscience, New York, **2001**. (b) Schmid, G. *Nanoparticles; From Theory to Application*, Wiley-VCH, Weinheim, Germany, **2004**. (c) Fendler, J. H. *Nanoparticles and Nanostructured Films*, Wiley-VCH, Weinheim, **1998**. (d) Fertman, V. E. *Magnetic Fluids Guide Book: Properties and Applications*; Hemisphere Publishing Co., New York, **1990**. (e) Berkovsky, B. M.; Medvedev, V. F.; Krakov, M. S. *Magnetic Fluids: Engineering Applications;* Oxford University Press, Oxford, **1993**. (f) Zhang, J. Z.; Wang, Z.-L.; Liu, J.; Chen, S.; Liu, G.-Y. *Self-Assembled Nanostructures*; Kluwer Academic/Plenum Publishers, New York, **2003.** (g) Pacholski, C.; Kornowski, A.; Weller, H. *Angew. Chem. Int. Ed.* **2002**, *41*, 1188. (h) Ashoori, R. C. *Nature* **1996**, *379*, 413.

[2] (a) Billas, I. M. L.; Chatelain, A.; de Heer, W. A. *Science* **1994**, *265*, 1682. (b) Vossmeyer, T.; Katsikas, L.; Giersig, M.; Popovic, I. G.; Diesner, K.; Chemseddine, A.; Eychmüller, Weller, H. *J. Phys. Chem.* **1994**, *98*, 7665. (c) Tolbert, S. H.; Alivisatos, A. P. *Science* **1994**, *265*, 373.

[3] Kim, B. H.; Lee, N.; Kim, H.; An, K.; Park, Y. I.; Choi, Y.; Shin, K.; Lee, Y.; Kwon, S. G.; Na, H. B.; Park, J.-G.; Ahn T.-Y.; Kim, Y.-W.; Moon, W. K.; Choi, S. H.; Hyeon T. *J. Am. Chem. Soc.* **2011**, *133*, 12624.

[4] Xie, J.; Zheng, Y.; Ying, J. Y. *J. Am. Chem. Soc.* **2009**, *131*, 888.

[5] (a) Talapin, D. V.; Rogach, A. L.; Shevchenko, E. V.; Kornowski, A.; Haase, M.; Weller, H. *J. Am. Chem. Soc.* **2002**, *124*, 5782. (b) Peng, X.; Wickham, J.; Alivisatos, A. P. *J. Am. Chem. Soc.* **1998**, *120*, 5343. (c) Kwon, S. G.; Piao, Y.;

Park, J.; Angappane, S.; Jo, Y.; Hwang, N.-M.; Park, J.-G.; Hyeon, T. *J. Am. Chem. Soc.* **2007**, *129*, 12571.

[6] Kim, B. H.; Shin, K.; Kwon, S. G.; Jang, Y.; Lee, H.-S.; Lee, H.; Jun, S. W.; Lee, J.; Han, S. Y.; Yim, Y.-H.; Kim, D.-H.; Hyeon, T. *J. Am. Chem. Soc.* **2013**, *135*, ASAP.

[7] Gatteschi, D.; Fittipaldi, M.; Sangregorio, C.; Sorace, L. *Angew. Chem. Int. Ed.* **2012**, *51*, 4792.

[8] Schaaff, T. G.; Shafigullin, M. N.; Khoury, J. T.; Vezmar, I.; Whetten, R. M.; Cullen, W. G.; First, P. N.; Gutierrez-Wing, C.; Ascensio, J.; Jose-Yacaman, M. J. *J. Phys. Chem. B* **1997**, *101*, 7885.

[9] Ceci, P.; Chiancone, E.; Kasyutich, O.; Bellapadrona, G.; Castelli, L.; Fittipaldi, M.; Gatteschi, D.; Innocenti, C.; Sangregorio, C. *Chem. Eur. J.* **2010,** *16*, 709.

[10] Willets, K. A.; van Duyne, R. P. *Annu. Rev. Phys. Chem.* **2007**, *58*, 267.

[11] (a) Niu, W.; Zheng, S.; Wang, D.; Liu, X.; Li, H.; Han, S.; Chen, J.; Tang, Z.; Xu, G. *J. Am. Chem. Soc.* **2009**, *131*, 697. (b) Kim, D. Y.; Yu, T.; Cho, E. C.; Ma, Y.; Park, O O.; Xia, Y. *Angew. Chem. Int. Ed.* **2011**, *50*, 6328. (c) Park, K.; Koerner, H. Vaia, R. A. *Nano Lett.* **2010**, *10*, 1433.

[12] (a) Schaaff, T. G.; Whetten, R. M. *J. Phys. Chem. B* **2000**, *104*, 2630. (b) Alvarez, M. M.; Khoury, J. T.; Schaaff, T. G.; Shafigullin M. N.; Vezmar, I.; Whetten, R. L. *J. Phys. Chem. B* **1997**, *101*, 3706.

[13] Kawabata, A.; Kubo, R. *J. Phys. Soc. Jpn*. **1966**, *21*, 1765.

[14] Link, S.; Beeby, A.; FitzGerald, S.; El-Sayed, M. A.; Schaaff, T. G.; Whetten, R. L. *J. Phys. Chem. B* **2002**, *106*, 3410.

[15] Kodama, R. H.; Berkowitz, A. E. *Phys. Rev. B* **1999**, *59*, 6321.

[16] (a) Noginova, N.; Weaver, T.; Giannelis, E. P.; Bourlinos, A. B.; Atsarkin, V. A.; Demidov, V. V. *Phys. Rev. B* **2008,** *77*, 014403. (b) Li, H.; Klem, M. T.; Sebby, K. B.; Singel, D. J.; Young, M.; Douglas, T.; Idzerda, Y. U. *J. Magn. Magn. Mater.* **2009**, *321*, 175.

[17] Fittipaldi, M.; Innocenti, C.; Ceci, P.; Sangregorio, C.; Castelli, L.; Sorace, L.; Gatteschi, D. *Phys. Rev. B* **2011**, 83, 104409.

[18] Castelli, L.; Fittipaldi, M.; Powell, A. K.; Gatteschi, D.; Sorace, L. *Dalton Trans.* **2011,** *40*, 8145.

[19] Nuetzenadel, C.; Zuettel, A.; Chartouni, D.; Schmid, G.; Schlapbach L. *Eur. Phys. J. D* **2000,** *8*, 245.

[20] Zhu, M.; Aikens, C. M.; Hendrich, M. P.; Gupta, R,; Qian, H.; Schatz, G. C.; Jin, R. *J. Am. Chem. Soc.* **2009**, *131*, 2490.

[21] McBride, J. R.; Dukes III, A. D.; Schreuder, M. A.; Rosenthal. S. J. *Chem. Phys. Lett.* **2010**, *498*, 1.

[22] (a) Garzon, I. L.; Michaelian, K.; Beltrán, M. R.; Posada-Amarillas, A.; Ordejón, P.; Artacho, E.; Sánchez-Portal, D.; Soler, J. M. *Phys. Rev. Lett.* **1998,** *81*, 1600. (b) Cleveland, C. L.; Landman, U.; Schaaff, T. G.; Shafigullin, M. N.; Stephens, P. W.; Whetten, R. L. *Phys. Rev. Lett.* **1997,** *79*, 1873.

[23] Jiles, D. *Introduction to Magnetism and Magnetic Materials, 2nd Ed.*; Chapman & Hall: London, **1998**.

[24] Crespo, P.; Litran, R.; Rojas, T. C.; Multigner, M.; de la Fuentes, J. M.; Sanchez-Lopez, J. C.; Garcia, M. A.; Hernando, A.; Penades, S.; Fernandez, A. *Phys. Rev. Lett.* **2004,** *93*, 087204.

[25] Suda, M.; Kameyama, N.; Suzuki, M.; Kawamura, N.; Einaga, Y. *Angew. Chem. Int. Ed.* **2008**, *47*, 160.

[26] Garitaonandia, J. S.; Insausti, M.; Goikolea, E.; Suzuki, M.; Cashion, J. D.; Kawamura, N.; Ohsawa, H.; de Muro, I, G.; Suzuki, K.; Plazaola, F.; Rojo, T. *Nano Lett.* **2008**, *8*, 661.

[27] Meulenberg, R. W.; Lee, J. R. I.; McCall, S. K.; Hanif, K. M.; Haskel, D.; Lang, J. C.; Terminello, L. J.; van Buuren, T. *J. Am. Chem. Soc.* **2009**, *131*, 6888.

[28] (a) Sun, S.; Zeng, H. *J. Am. Chem. Soc.* **2002,** *124*, 8204. (b) Sun, S.; Zeng, H.; Robinson, D. B.; Raoux, S.; Rice, P. M.; Wang, S. X.; Li, G. *J. Am. Chem. Soc.* **2004,** *126*, 273. (c) Peng, S.; Sun, S. *Angew. Chem., Int. Ed.* **2007,** *46*, 4155.

[29] (a) Redl, F. X.; Black, C. T.; Papaefthymiou, G. C.; Sandstrom, R. L.; Yin, M.; Zeng, H.; Murray, C. B.; O'Brien, S. P. *J. Am. Chem. Soc.* **2004,** *126*, 14583. (b) Rockenberger, J.; Scher, E. C.; Alivisatos, A. P. *J. Am. Chem. Soc.* **1999,** *121*, 11595. (c) Kim, D.; Lee, N.; Park, M.; Kim, B. H.; An, K.; Hyeon, T. *J. Am. Chem. Soc.* **2009,** *131*, 454. (d) Hyeon, T.; Lee, S. S.; Park, J.; Chung, Y.; Na, H. B. *J. Am. Chem. Soc.* **2001,** *123*, 12798. (e) Cheon, J.; Kang, N.-J.; Lee, S.-M.; Lee, J.-H.; Yoon, J.-H.; Oh, S. J. *J. Am. Chem. Soc.* **2004,** *126*, 1950. (f)

Laurent, S.; Forge, D.; Port, M.; Roch, A.; Robic, C.; Elst, L. V.; Muller, R. N. *Chem. Rev.* **2008,** *108*, 2064. (g) Park, J.; An, K.; Hwang, Y.; Park, J.-G.; Noh, H.-J.; Kim, J.-Y.; Park, J.-H.; Hwang, N.-M.; Hyeon, T. *Nat. Mater.* **2004,** *3*, 891. (h) Jana, N. R.; Chen, Y.; Peng, X. *Chem. Mater.* **2004,** *16*, 3931. i) Yu, W. W.; Falkner, J. C.; Yavuz, C. T.; Colvin, V. L. *Chem. Commun.* **2004,** 2306. (j) Park, J.; Lee, E.; Hwang, N.-M.; Kang, M.; Kim, S. C.; Hwang, Y.; Park, J.-G.; Noh, H.-J.; Kim, J.-Y.; Park, J.-H.; Hyeon, T. *Angew. Chem., Int. Ed*. **2005,** *44*, 2872. (k) Kovalenko, M. V.; Bodnarchuk, M. I.; Lechner, R. T.; Hesser, G.; Schäffler, F.; Heiss, W. *J. Am. Chem. Soc.* **2007,** *129*, 6352.

[30] (a) Coey, J. M. D. *Phys. Rev. Lett.* **1971,** *27*, 1140. (b) Yang, H.; Ogawa, T.; Hasegawa, D.; Takahashi, M. *J. Appl. Phys.* **2008,** *103*, 07D526.

[31] Linderoth, S.; Hendriksen, P. V.; Bødker, F.; Wells, S.; Davies, K.; Charles, S. W.; Mørup, S. *J. Appl. Phys.* **1994,** *75*, 6583.

[32] Kodama, R. H.; Berkowitz, A. E.; McNiff, Jr, E. J.; Foner, S.; *Phys. Rev. Lett.* **1996,** *77*, 394.

[33] Qian, H.; Zhu, M.; Wu, Z.; Jin, R. *Acc Chem. Res.* **2012,** *45*, 1470.

[34] Jin, R. *Nanoscale* **2010**, *2*, 343.

[35] Chen, W.; Chen, S. *Angew. Chem. Int. Ed.* **2009,** *48*, 4386.

[36] Bowers II, M. J.; McBride, J. R.; Rosenthal, S. J. *J. Am. Chem. Soc.* **2005**, *127*, 15378.

[37] Kroto, H. W.; Heath, J. R.; O'Brien, S. C.; Curl, R. F.; Smalley, R. E. *Nature* **1985**, *318*, 162.

[38] Glib, S.; Weis, P.; Furche, F.; Ahlrichs, R.; Kappes, M. M. *J. Chem. Phys.* **2002**, *116*, 4094.

[39] (a) Schmid. G. Klein, N.; Morun, B.; Legnert, A. *Pure Appl Chem.* **1990.** *62*, 1175. (b) Michaelian, K.; Rendon, N.; Garzon, I. L. *Phys. Rev. B* **1999**, *60*, 2000.

[40] (a) Hyeon, T. *Chem. Commun*. **2003,** 927. (b) Park, J.; Joo, J.; Kwon, S. G.; Jang, Y.; Hyeon, T. *Angew. Chem. Int. Ed.* **2007**, *46*, 4630. (c) Gu, H.; Xu, K.; Xu, C.; Xu, B. *Chem. Commun.* **2006**, 941. (d) Sun, S. *Adv. Mater*. **2006**, *18*, 393. (e) Jeong, U.; Teng, X.; Wang, Y.; Yang, H.; Xia, Y. *Adv. Mater.* **2007**, *19*, 33. (f) Jun, Y.-w.; Choi, J.-s.; Cheon, J. *Angew. Chem. Int. Ed.* **2006**, *45*, 2. (g) Jun, Y.-w.; Choi, J.-s.; Cheon, J. *Chem. Commun.* **2007**, 1203. (h) Lu, A.-H.; Salabas, E. L.; Schüth, F. *Angew. Chem. Int. Ed.* **2007**, *46*, 1222.

[41] Schmid. G. *Polyhedron* **1988.** *7*, 2321.

[42] Weare, W. W.; Reed, S. M.; Warner, M. G.; Hutchison, J. E. *J. Am. Chem. Soc.* **2000**, *122*, 12890.

[43] Brust, M.; Walker, M.; Betheil, D.; Schiffrin, D. J.; Whyman, R. *J. Chem. Soc., Chem. Commun.* **1994**, 801.

[44] Zhu, M.; Lanni, E.; Garg, N.; Bier, M. E.; Jin, R. *J. Am. Chem. Soc*. **2008**, *130*, 1138.

[45] (a) Toikkanen, O.; Ruiz, V.; Ronnholm, G.; Kalkkinen, N.; Liljeroth, P.; Quinn, B. M. *J. Am. Chem. Soc*. **2008**, *130*, 11049. (b) Balasubramanian, R.; Guo, R.; Mills, A. J.; Murray R. W. *J. Am. Chem. Soc*. **2005**, *127*, 8126.

[46] Qian, H.; Zhu, Y.; Jin, R. *J. Am. Chem. Soc*. **2010**, *132*, 4583.

[47] Dass, A. *J. Am. Chem. Soc.* **2009**, *131*, 11666.

[48] (a) Jadzinsky, P. D.; Calero, G.; Ackerson, C. J.; Bushnell, D. A.; Konberg, R. D. *Science* **2007**, *318*, 430. (b) Levi-Kalisman, Y.; Jadzinsky, P. D.; Kalisman, N.; Tsunoyama, H.; Tsukuda, T.; Bushnell, D. A.; Kornberg, R. D. *J. Am. Chem. Soc.* **2011**, *133*, 2976.

[49] Qian, H.; Jin, R. *Nano Lett.* **2009**, *9*, 4083.

[50] Qian, H.; Zhu, Y.; Jin, R. *Proc. Natl. Acad. Sci. U.S.A.* **2012,** *109,* 696.

[51] Kim, Y.-G.; Oh, S.-K.; Crooks, R. M. *Chem. Mater.* **2004,** *16,* 167.

[52] Park, J.; Kwon, S. G.; Jun, S. W.; Kim, B. H.; Hyeon T. *ChemPhysChem* **2012**, *13*, 2540.

[53] Maretti, L.; Billone, P. S.; Liu, Y.; Scaiano, J. C. *J. Am. Chem. Soc.* **2009**, *131*, 13972.

[54] Teranish, T.; Hosoe, M.; Tanaka, T.; Miyake, M. *J. Phys. Chem. B* **1999**, *103*, 3818.

[55] Li, Y.; Whyburn, G. P.; Huang, Y. *J. Am. Chem. Soc.* **2009**, *131*, 15998.

[56] Schmid, G.; Harms, M.; Malm, J.-O.; Bovin, J.-O.; van Ruitenbeck, J.; Zandbergen, H. W.; Fu, W. T. *J. Am. Chem. Soc.* **1993**, *105*, 2046.

[57] Glaria, A.; Kahn, M. L.; Falqui, A.; Lecante, P.; Colliere, V.; Respaud, M.; Chaudret, B. *ChemPhysChem* **2008,** *9*, 2035.

[58] Teng, X.; Yang, H. *J. Mater. Chem.* **2004,** *14*, 774.

[59] Park, J. Y.; Choi, E. S.; Baek, M. J.; Lee, G. H.; Woo, S.; Chang, Y. *Eur. J. Inorg. Chem.* **2009,** 2477.

[60] Park, J. Y.; Baek, M. J.; Choi, E. S.; Woo, S.; Kim, J.; Kim, T. J.; Kim, J. C.; Chae, K. S.; Chang, Y.; Lee, G. H. *ACS NANO* **2009,** *3*, 3663.

[61] Bonacchi, D.; Caneschi, A.; Dorignac, D.; Falqui, A.; Gatteschi, D.; Rovai, D.; Sangregorio, C.; Sessoli. R. *Chem. Mater.* **2004,** *16*, 2016.

[62] Morales, M. P.; Bomati-Miguela, O.; de Alejo, R. P.; Ruiz-Cabellob, J.; Veintemillas-Verdaguera, S.; O′Grady, K. *J. Magn. Magn. Mater.* **2003,** *266*, 102.

[63] Lee, Y.; Lee, J.; Bae, C. J.; Park, J.-G.; Noh, H.-J.; Park, J.-H.; Hyeon, T. *Adv. Funct. Mater.* **2005,** *15*, 503.

[64] Barnett, R. N.; Cleveland, C. L.; Hakkinen, H.; Luedtke, W. D.; Yannouleas, C.; Landman, U. *Eur. Phys. J. D* **1999**, *9*, 95.

[65] Peng, Z. A.; Peng, X. *J. Am. Chem. Soc.* **2002**, *124*, 3343.

[66] Kudera, S.; Zanella, M.; Giannini, C.; Rizzo, A.; Li, Y.; Gigli, G.; Cingolani, R.; Ciccarella, G.; Spahl, W.; Parak, W. J.; Manna, L. *Adv. Mater.* **2007,** *19*, 548.

[67] (a) Kasuya, A. et al., *Nat. Mater.* **2004,** 3, 99. (b) Jose, R.; Zhanpeisov, N. U.; Fukumura, H.; Baba, Y.; Ishikawa, M. *J. Am. Chem. Soc.* **2006,** *128*, 629. (c) Riehle, F. S.; Bienert, R.; Thomann, R.; Urban, G. A.; Kruger, M. *Nano Lett.* **2009**, *9*, 514. (d) Dagtepe, P.; Chikan, V.; Jasinski, J.; Leppert, V. J. *J. Phys. Chem. C* **2007,** *111*, 14977. (e) Evans, C. M.; Guo, L.; Peterson, J. J.; Maccagnano-Zacher, S.; Krauss T. D. et al. *Nano Lett.* **2008,** *8*, 2896. (f) Yu, Q.; Liu, C.-Y. *J. Phys. Chem. C* **2009,** *113*, 12766.

[68] (a) Murray, C. B.; Norris, D. J.; Bawendi, M. G. *J. Am. Chem. Soc.* **1993**, *115*, 8706. (b) Alivisatos, A. P. *Science* **1996**, *271*, 933. (c) Talapin, D. V.; Lee, J.-S.; Kovalenko, M. V.; Shevchenko, E. V. *Chem. Rev.* **2010**, *110*, 389. (d) Joo, S. H.; Park, J. Y.; Renzas, J. R.; Butcher, D. R.; Huang, W.; Somorjai, G. A. *Nano Lett.* **2010**, *10*, 2709.

[69] Wilcoxon, J. P.; Martin, J. E.; Provencio, P. *J. Chem. Phys.* **2001**, *115*, 998.

[70] Zheng, H.; Smith, R. K.; Jun, Y.-w.; Kisielowski, C.; Dahmen, U.; Alivisatos, A. P. *Science* **2009**, *324*, 1309.

[71] Yuk, J. M.; Park, J.; Ercius, P.; Kim, K.; Hellebusch, D. J.; Crommie, M. F.; Lee, J. Y.; Zettl, A.; Alivisatos, A. P. *Science* **2012**, *336*, 61.

[72] Wang, Z. W.; Toikkanene, O.; Yin, F.; Li, Z. Y.; Quinn, B. M.; Palmer, R. E.; *J. Am. Chem. Soc.* **2010**, *132*, 2854.

[73] Bai, C. *Scanning tunneling microscopy and its applications*. New York: Springer Verlag, **2000**.

[74] Crommie, M. F.; Lutz, C. P.; Eigler, D. M. *Science* **1996**, *262*, 218.

[75] Skoog, D. A.; Holler, F. J.; Nieman, T. A. *Principles of Instrumental Analysis*, 5th ed.; Harcourt College Publishers: Orlando, **1998**.

[76] Whetten, R. L.; Khoury, J. T.; Alvarez, M. M.; Murthy, S.; Vezmar, I.; Wang, Z. L.; Stephens, P. W.; Cleveland, C. L.; Luedtke, W. D.; Landman, U. *Adv. Mater.* **1996,** *8*, 428.

[77] (a) Tracy, J. B.; Crowe, M. C.; Parker, J. F.; Hampe, O.; Fields-Zinna, C. A.; Dass, A,; Murray, R. W. *J. Am. Chem. Soc.* **2007**, *129*, 16209. (b) Navin, J. K.; Grass, M. E.; Somorjai, G. A.; Marsh, A. L. *Anal. Chem.* **2009**, *81*, 6295.

[78] Khitrov, G. A.; Strouse, G. F. *J. Am. Chem. Soc.* **2003**, *125*, 10465.

[79] (a) Talapin, D. V.; Rogach, A. L.; Shevchenko, E. V.; Kornowski, A.; Haase, M.; Weller, H. *J. Am. Chem. Soc.* **2002**, *124*, 5782. (b) Peng, X.; Wickham, J.; Alivisatos, A. P. *J. Am. Chem. Soc.* **1998**, *120*, 5343. (c) Peng, Z. A.; Peng, X. *J. Am. Chem. Soc.* **2002**, *124*, 3343.

Chapter 2. Large-scale Synthesis of Uniform and Extremely Small-sized Iron Oxide Nanoparticles for MRI Application

2.1 Introduction

The synthesis and application of monodisperse nanoparticles has been intensively researched for various applications because of their interesting size dependent physical properties. Iron oxide nanoparticles is one of the most fascinating materials because they exhibit magnetic properties and can be applied to various area such as magnetic separation, magnetic resonance imaging (MRI) contrast agents, magnetic carriers for drug targeting, and catalyst. The iron oxide nanoparticles show highly size-dependent magnetic properties.[1] As the particle size decreases, magnetization of iron oxide nanoparticles decreases due to spin canting effect, which results from the lack of full alignment of the spins in surface atoms.[2,3] The thickness of magnetically disordered shell of maghemite is known to be one unit cell length.[2,3] Assuming that the thickness of the spin canted layer is 0.9 nm, iron oxide nanoparticles of < 1.8 nm-size become almost paramagnetic. The

new property of the small iron oxide nanoparticles will be expected to open up new application area and we will refer them as extremely small-sized iron oxide nanoparticles (ESIONs).

MRI is one of the most powerful diagnostic tools because it can provide excellent anatomical images and functional information.[4-6] Contrast agent in MRI is a magnetic chemical compound which enhances the signal of the region of interest.[7,8] The magnetic property of contrast agents lead to enhancement of the spin relaxation of water proton. MRI contrast agents are distinguished according to relaxation mode, longitudinal (T_1) and transversal (T_2) relaxation. T_1 relaxation results in bright image whereas T_2 relaxation exhibits dark MR images. Effectiveness of relaxation is denoted as relaxivity (r_1, r_2).

T_2 relaxation is mainly influenced by magnetic inhomogeneity.[8] Superparamagnetic iron oxide nanoparticles (SPIO) such as Feridex are commonly used as T_2 contrast agents because the high magnetic moment of the nanoparticles induces inhomogeneity. T_2 MR imaging is not preferred in clinical area for several reasons. Intrinsic dark signal in the T_2 image make region of interest confused with other hypointense areas, such as bleeding, metal deposition, or calcification.[4] Moreover, the high magnetic moment of iron oxide nanoparticles causes blooming effect, so blurred images are often

obtained.[9] For these reasons, T_1 MRI contrast agent is preferred as T_2 agent in clinical settings.[5]

T_1 relaxation is enhanced by the interaction between electron spins of the contrast agents and protons of water.[10] Therefore, paramagnetic compounds with many unpaired electrons are appropriate materials for T_1 contrast agents. Gadolinium complexes have been used as T_1 contrast agents because they have 7 unpaired electrons in their Gd^{3+} core.[10] However, gadolinium-based MR contrast agents are highly toxic for patients with severe kidney failure because free Gd^{3+} ions released from gadolinium complexes induces nephrogenic system fibrosis (NSF).[11] To overcome these problems, Gd or Mn nanoparticle-based T_1 contrast agents have been developed in recent years.[12-14] However, toxicity problem of these contrast agents has not been completely solved yet.[15] Consequently, development of new-nontoxic T_1 MRI contrast agents is still highly required.

Ideal T_1 contrast agents should have high r_1 value and low r_2/r_1 ratio to maximize the T_1 contrast effect and low toxicity. Iron oxide is more biocompatible than Gd or Mn-based materials because the iron species are abundant in human body, which are mostly stored in iron containing protein such as ferritin. Moreover, Fe^{3+} ions in iron oxide nanoparticles have 5 unpaired electrons. However, common iron oxide nanoparticles are not

appropriate for the T_1 MRI contrast agents because the high r_2 of iron oxide nanoparticles derived from innate high magnetic moment prevents them from being used as T_1 MRI contrast agents.

As we have seen earlier, extremely small-sized iron oxide nanoparticles (ESIONs) have weak magnetic moment due to small volume magnetic anisotropy and spin canting effect.[16-17] ESIONs are potential candidates for T_1 contrast agents because the nanoparticles can enhance T_1 effect by their large surface area with 5 unpaired electrons and suppress T_2 effect by their small magnetic moment. Moreover, the nanoparticles are advantageous for functionalization and long term imaging. Previous reports showed that small-sized iron oxide nanoparticles have a potential to be utilized as T_1 MRI contrast agents.[18] However, the nanoparticles in the previous reports still exhibited high magnetic moment because the particle sizes were larger than 4 nm.

It is important to synthesize size-controlled uniform iron oxide nanoparticles because the MR relaxivity is strongly dependent on the dimension of nanoparticles.[19] Although many papers regarding synthetic methods of uniform iron oxide nanoparticles were published,[20,21] synthesis of iron oxide nanoparticles smaller than 3 nm have been rarely reported.[22] Moreover, the previous synthetic methods have several limitations for large-

scale synthesis due to high cost of reagents and low yield. In this thesis, we report the synthesis of uniform and extremely small-sized iron oxide nanoparticles (ESIONs) of size ~1.5 nm using the heat-up method. The synthetic procedure is simple, cost-effective, and easy to scale up. Furthermore, the nanoparticles were successfully used as T_1 MRI contrast agents.

2.2 Experimental Section

2.2.1 Chemicals

90% oleic acid, iron chloride hexahydrate ($FeCl_3 \cdot 6H_2O$), 1-octadecene, dioctyl ether and phosphoryl chloride ($POCl_3$) were purchased from Aldrich. Diphenyl ether, sodium oleate, and oleyl alcohol were purchased from TCI. Oleylamine was purchased from Acros. Poly(ethylene glycol) methyl ether 2000 (mPEG-2000) were purchased from Sunbio Co. 1,2-distearoyl-*sn*-glycero-3-phosphoethanolamine-N-[methoxy (polyethylene glycol)-2000] (mPEG-2000 PE) were purchased from Avanti Polar Lipids, Inc. Ethanol, *n*-heptane, chloroform ($CHCl_3$), and *n*-hexane were purchased from Samchun Chem.

2.2.2 Synthesis of Iron Oxide Nanoparticles

2.2.2.1 Synthesis of Iron-oleate Complexes

Iron-oleate complexes were synthesized based on our previously reported procedure.[20] Iron chloride (10.8 g; 40 mmol) and sodium oleate (36.5 g; 120 mmol) was dissolved in a mixture solvent which composed of ethanol (80 mL), distilled water (60 mL), and hexane (140 mL). The resulting solution was heated to 69 °C and kept at that temperature for 4 h. After completion of the reaction, the upper organic layer containing the iron–oleate complexes

was washed three times with 100 mL of distilled water using a separatory funnel. After washing, hexane was evaporated off, resulting in iron–oleate complex in a waxy solid form.

2.2.2.2 Large-scale synthesis of 3 nm Iron Oxide Nanoparticles

For the synthesis of large scale synthesis of 3 nm iron oxide nanoparticles, iron-oleate complex (36 g; 40 mmol) synthesized as described above, oleic acid (10.4 g; 40 mmol), oleyl alcohol (32.2 g; 120 mmol), and diphenyl ether (200 g) were mixed at room temperature in 1 L reactor. The reaction mixture was degassed at 90 °C under vacuum for 2 h and heated to 250 °C with a heating rate of 10 °C/min. The reaction mixture was aged at 250 °C for 30 min under Ar atmosphere. When the reaction occurred, the initial transparent brown solution became black. The resulting solution containing the nanoparticles was then rapidly cooled to room temperature, and 700 mL of acetone was added to the solution to precipitate the nanoparticles. The nanoparticles were separated by discarding supernatant and dispersed in hydrophobic solvent such as *n*-hexane or chloroform. 5.033 g of nanoparticles were obtained by large-scale synthesis. Mass fraction of iron was obtained by inductively coupled plasma atomic emission spectroscopy (ICP-AES; ICPS-7500 spectrometer, Shimadzu) and the result was 37.6%. Reaction yield was

calculated by substituting the iron mass fraction and the yield was 84.3%.

2.2.2.3 Synthesis of 2.2 nm Iron Oxide Nanoparticles

For the synthesis of 2.2 nm iron oxide nanoparticles, iron-oleate complex (1.8 g; 2 mmol), oleyl alcohol (3.22 g; 12 mmol), and diphenyl ether (10 g) were mixed at room temperature in 100 mL reactor. The reaction mixture was degassed and heated to 250 ^{o}C with a heating rate of 10 ^{o}C/min, and then aged at that temperature for 30 min under Ar atmosphere. The resulting solution containing the nanoparticles was then rapidly cooled to room temperature. The nanoparticles were separated from reaction mixture by adding excess acetone and dispersed in hydrophobic solvent such as *n*-hexane or chloroform.

2.2.2.4 Synthesis of 1.5 nm Iron Oxide Nanoparticles

For the synthesis of 1.5 nm iron oxide nanoparticles, iron-oleate complex (1.8 g; 2 mmol), oleyl alcohol (3.22 g; 12 mmol), and diphenyl ether (10 g) were mixed at room temperature in 100 mL reactor. The reaction mixture was degassed and heated to 200 °C with a heating rate of 10 ^{o}C/min, and then aged at that temperature for 30 min under Ar atmosphere. The resulting solution containing the nanoparticles was then rapidly cooled to room temperature. The nanoparticles were separated from reaction mixture by

adding excess acetone and dispersed in hydrophobic solvent such as *n*-hexane or chloroform.

2.2.2.5 Synthesis of 3.7 nm Iron Oxide Nanoparticles

For the synthesis of 3.7 nm iron oxide nanoparticles, iron-oleate complex (1.8 g; 2 mmol), oleyl alcohol (1.61 g; 6 mmol), oleic acid (0.57 g; 2 mmol), and 1-octadecene (10 g) were mixed at room temperature in 100 mL reactor. The reaction mixture was degassed and heated to 280 °C with a heating rate of 10 ^{o}C/min, and then aged at that temperature for 30 min under Ar atmosphere. The resulting solution containing the nanoparticles was then rapidly cooled to room temperature. The nanoparticles were separated from reaction mixture by adding excess acetone and dispersed in hydrophobic solvent such as *n*-hexane or chloroform.

2.2.3 Nanoparticle Characterization

Iron oxide nanoparticles were analyzed using JEOL-2010 and FEI Tecnai F20 electron microscopes. Powder X-ray diffraction (XRD) patterns were collected with a Rigaku D/Max-3C diffractometer, equipped with a rotating anode and a Cu Kα radiation source (λ = 0.15418 nm). Magnetic studies were carried out using a Vibrating Sample Magnetometer (VSM) equipped within

Physical Property Measurement System (PPMS®) manufactured by Quantum Design with fields up to 3 T and temperature ranging from 5 to 300 K. Fourier transform infrared (FT-IR) spectra of sample aliquots were obtained with a JASCO FT/IR 200. Hydrodynamic diameters of nanoparticles dispersed in water were analyzed with Otsuka ELS-Z particle size analyzer.

2.2.4 Surface modification of Iron Oxide Nanoparticles

2.2.4.1 Synthesis of PO-PEG

PEG-derivatized phosphine oxide (PO-PEG) were synthesized following a previously reported method.[23] In a typical synthetic procedure, 3 mmol of dry Poly(ethylene glycol) methyl ether 2000 (mPEG-2000) was dissolved in 7 ml of anhydrous THF. 1 mmol of phosphoryl chloride ($POCl_3$) was added to the mPEG THF solution and stirred at room temperature for 1 day. Colorless gel was obtained by evacuation of the resulting product stayed at 100 ºC under vacuum for 12 hour.

2.2.4.2 Ligand Exchange of Iron Oxide Nanoparticles with PO-PEG

Procedures for ligand exchange with PO-PEG were adopted from previous works from Hyeon and van Veggel group with some modifications.[23,24] In a typical procedure, 3 nm iron oxide nanoparticles (8 mg) and PO-PEG (160

mg) were dispersed in a mixed solvent of ethanol (1 mL) and *n*-heptane (1 mL). The mixture was kept at 70 °C for 5 h in stirring. PO-PEG coated nanoparticles were precipitated from the product after addition of *n*-hexane. The hydrophilic iron oxide nanoparticles were collected by centrifugation and redispersed in ethanol. Centrifugation and redispersing steps were repeated three times for complete removal of residual PO-PEG and organic moiety. Distilled water was added to the washed PO-PEG capped iron oxide nanoparticles and final product were obtained by removal of remained ethanol via evaporation.

2.2.4.3 Encapsulation of Iron Oxide Nanoparticles with PEG-Phospholipid Ligands

PEG-phospholipid encapsulation of iron oxide nanoparticles were based on previously reported procedure.[14a,25] In a typical procedure, 3 nm iron oxide nanoparticles (10 mg) and mPEG-2000 PE (30 mg) were mixed in chloroform. Solvent of the mixture was evaporated and the mixture was incubated at 70 ºC in vacuum for 2 h. After then, 10 mL of water was added and a clear dispersion was formed. After filtration, excess PEG-phospholipid was removed by centrifugation.

2.2.5 Cell viability

The cellular toxicity of nanoparticles was evaluated using calcein-acetoxymethyl ester (AM)/propium iodide (PI) and 7-Aminoactinomycin D (7-AAD) assay.

For calcein-AM/PI assay, the cells were seeded into 200 μL of media and grown overnight. The cells were then incubated with 50 and 100 μg Fe/mL of 3 nm and 12 nm-sized iron oxide nanoparticles at 37 ^{o}C. After the overnight incubation, cells were incubated in media 10 μM calcein-AM and 3 μM PI for 30 min. Cell viability was evaluated by confocal microscopy.

For 7-AAD assay, the cells were incubated with iron oxide nanoparticles for 24 hr. Subsequently, the cells were trypsinizied, washed with PBS buffer, and treated with 7-AAD (BD Pharmingen) according to the manufacturer's protocol. The viability of cells were analyzed using flow cytometry (FACS Callibur, Becton&Dickinson). Untreated cells and H_2O_2-treated cells served as a negative control and positive control, respectively.

2.2.6. MRI Relaxation Properties of Iron Oxide Nanoparticles

Magnetic Resonance relaxivities of iron oxide nanoparticles were evaluated using a clinical 3 T MR scanner (Siemens, TrioTrim) with a wrist coil. The measurement parameters of T_1: T_R = 4000 ms, T_E = 14 ms, and T_I =

25~3500 ms. Measurement parameters of T_2: T_R = 5000 ms and T_E = 16~200 ms.

2.3 Result and Discussion

2.3.1 Synthesis of Extremely Small-sized Iron Oxide Nanoparticles

Extremely small-sized iron oxide nanoparticles (ESIONs) with their size below 4 nm were successfully synthesized by thermal decomposition of iron-oleate complex in the presense of long chain alcohol via heat-up process. The inexpensive and stable precursors, iron–oleate complexes, were prepared from simple reaction of iron chlorides and sodium oleate. For the synthesis of 3 nm ESIONs, 1.8 g (2 mmol) of iron-oleate complex, 1.61 g (6 mmol) of oleyl alcohol, and 0.57 g (2 mmol) of oleic acid and were mixed in 10 g of diphenyl ether. The mixture was heated to 250 °C with a heating rate of 10 °C/min, and maintained for 30 min. The resulting nanoparticles were washed several time with acetone and redispersed in chloroform.

Transmission electron microscopy (TEM) image of the uniform 3 nm ESIONs is shown in Figure 2.1. Hexagonal ordered array of ESIONs indicate their size uniformity. The synthetic method can be easily scaled up. For example, 5 g of 3 nm ESIONs could be prepared from a single batch reaction using 40 mmol of iron-oleate complex in 1 L reactor (Figure 2.2). ESIONs were highly stable in nonpolar solvents such as chloroform for several months without any precipitation.

The size of nanoparticles can be controlled from 1.5 nm to 3.7 nm by varying concentration and aging temperature as shown in Figure 2.3. When 1.8 g (2 mmol) of iron-oleate complex, 1.61 g (6 mmol) of oleyl alcohol, and 0.57 g (2 mmol) of oleic acid were reacted in 10 g of diphenyl ether, 3 nm nanoparticles were synthesized (Figure 2.4b). In the absence of oleic acid, 2.2 nm iron oxide nanoparticles were produced (Figure 2.4d). The size of ESIONs can also be controlled by varying the aging temperature. When the reaction mixure for the synthesis of 3 nm ESIONs were aged at 200 ^{o}C, 1.9 nm nanoparticles were synthesized (Figure 2.4a). When the reaction mixture for 2 nm ESIONs was aged at 200 ^{o}C, 1.5 nm nanoparticles were obtained (Figure 2.4c). When the reaction mixure for the synthesis of 3 nm ESIONs were dissolve in 1-octadecene and aged at 280 ^{o}C or 310 ^{o}C, 3.4 and 3.7 nm nanoparticles were obtained, respectively (Figure 2.5). When dioctyl ether or dibenzyl ether were used as the solvent, polydisperse nanoparticles were obtained (Figure 2.6). When the heating rate was lowered from 10 ^{o}C/min to 5 ^{o}C/min and other variables were fixed, a mixture of 3.5 and 6 nm nanoparticles was obtained instead of monodisperse 3 nm particles (Figure 2.7a,b). When the heating rate was raised to 20 ^{o}C/min, 2.7 nm particles were obtained (Figure 2.7c). The result demonstrates that fast heating rate is responsible for the size uniformity.

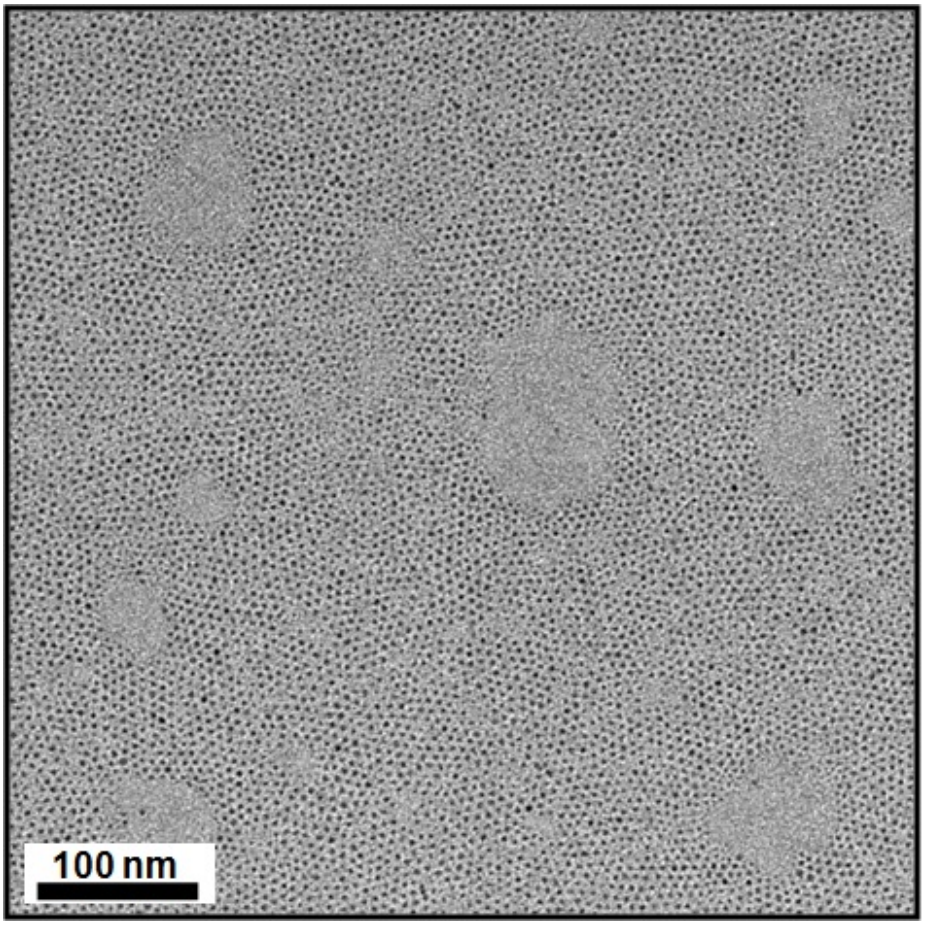

Figure 2.1 TEM images of 3 nm iron oxide nanoparticles at the magnifications of 40k.

Figure 2.2 Large scale synthesis of 3 nm iron oxide nanoparticles and (inset) TEM image of the nanoparticles.

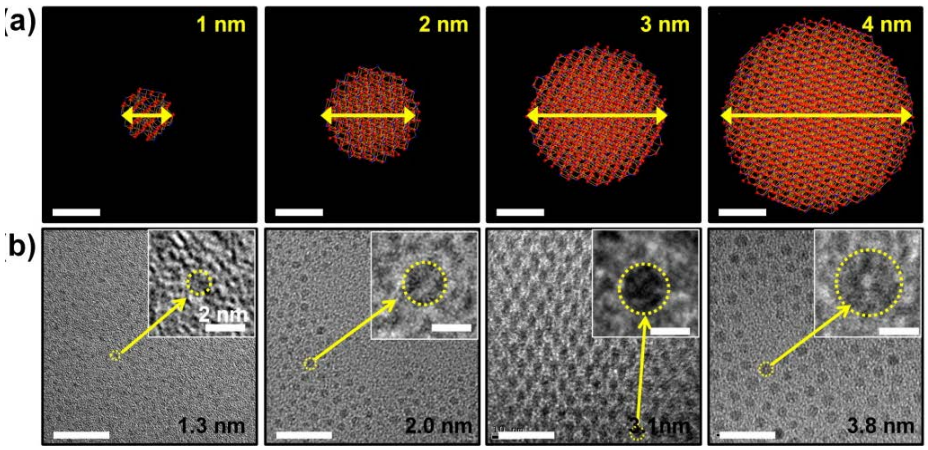

Figure 2.3 (a) Ball-and-stick model and (b) corresponding TEM images of 1, 2, 3, and 4 nm iron oxide nanoparticles.

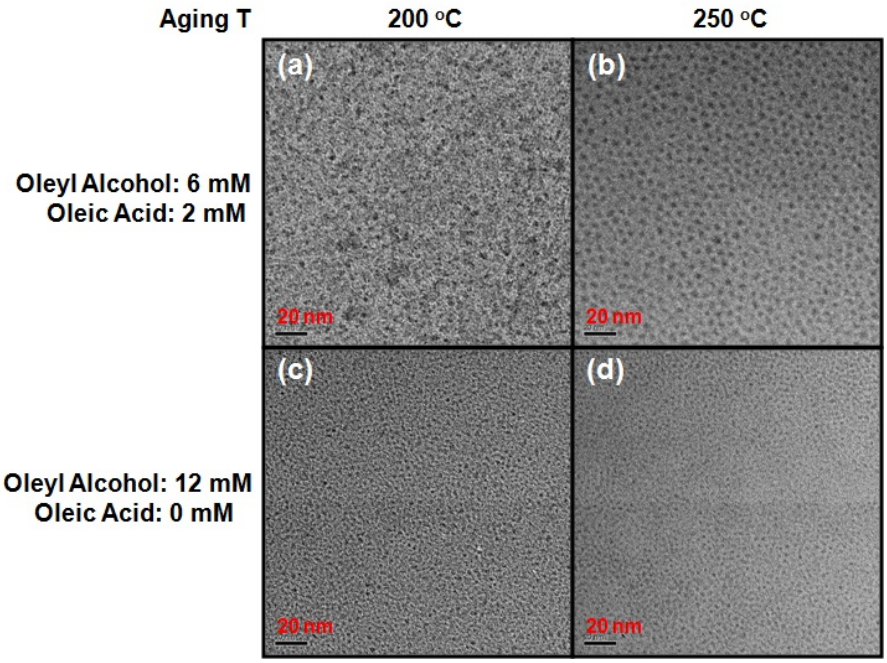

Figure 2.4 TEM images of various sized ESIONs. Their sizes were controlled by changing the aging temperature and concentration of reactant. [Sizes: (a) 1.9 nm, (b) 3 nm, (c) 1.5 nm, and (d) 2.2 nm]

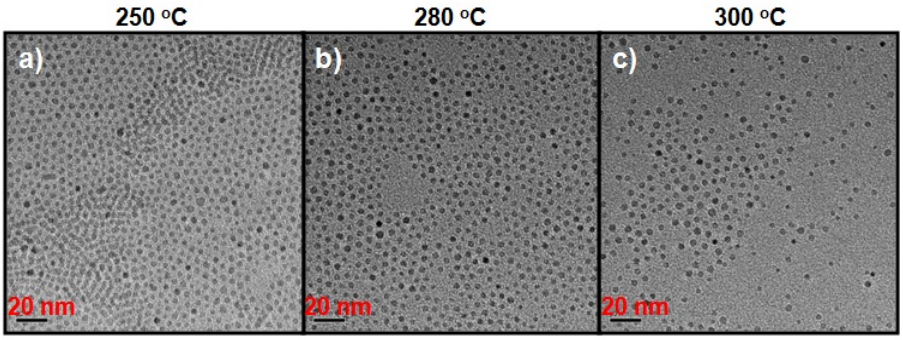

Figure 2.5 TEM images of (a) 3 nm, (b) 3.4 nm, and (c) 3.7 nm iron oxide nanoparticles using 1-octadecene as solvent. The size was controlled by varying the aging temperature (a) 250 ^{o}C, (b) 280 ^{o}C, and (c) 300 ^{o}C.

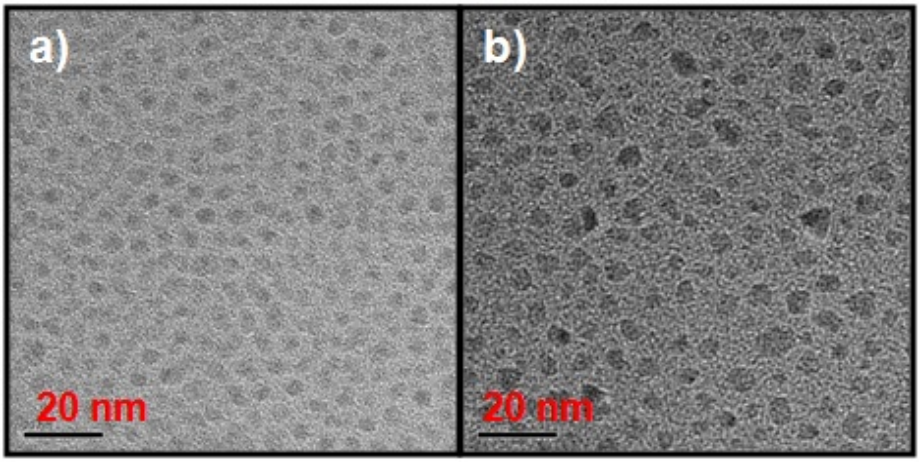

Figure 2.6 TEM images of polydisperse iron oxide nanoparticles using (a) dioctyl ether and (b) dibenzyl ether as solvent.

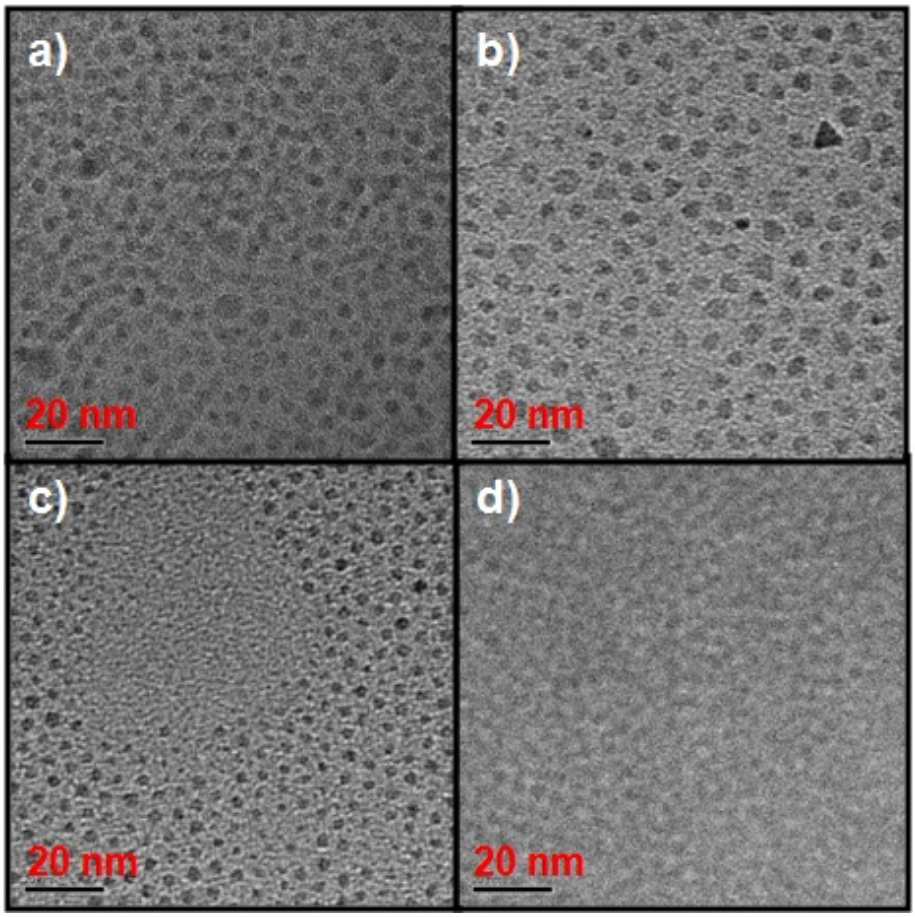

Figure 2.7 TEM images of (a), (b) polydisperse, (c) 2.7 nm iron oxide nanoparticles controlled by heating rate control. [Heating rate: (a) 3.3 ^{o}C/min; (b) 5 ^{o}C/min; (c) 20 ^{o}C/min; (d) 40 ^{o}C/min]

2.3.2 Mechanism

Although the exact formation mechanism is not clear, there are several evidences that the presence of oleyl alcohol plays a critical role in the synthesis of the nanoparticles smaller than 3 nm. FT-IR spectra of the sample aliquots drawn from the reaction mixture during the heating procedure clearly showed that oleyl alcohol was oxidized to aldehyde during the reaction (Figure 2.8), indicating that oleyl alcohol acts as a mild reductant. Reduced iron atoms seem to be released from the iron-oleate complex and can lead to subsequent nucleation and growth of the nanoparticles.[26] No particle was formed in the absence of oleyl alcohol while keeping all the other reaction conditions unchanged (Figure 2.9a). When other mild reductants such as 1,2-hexadecanediol or oleylamine were used in the synthesis, the small sized nanoparticles could also be obtained at the aging temperature of 250 ^{o}C, but they were not as uniform as those synthesized using oleyl alcohol (Figure 2.9b,c). The role of oleyl alcohol in the synthesis of ESIONs can be explained as follows. In the previous heat-up process for the synthesis of iron oxide nanoparticles, thermal decomposition of iron-oleate complex, which commenced at ~300 ^{o}C, led to the formation of nanoparticles.[20,27] When the aging temperature was decreased to < 250 ^{o}C, the thermal decomposition reaction was too slow to control

nucleation and growth processes, consequently resulting in polydisperse nanoparticles.[20] On the other hand, when oleyl alcohol was used as the reductant, an additional reaction pathway was provided for the release of iron atoms from the iron-oleate complex at much lower temperature. The lowered reaction temperature has a positive effect on the synthesis of the smaller nanoparticles. During the nucleation process for the synthesis of colloidal nanoparticles, a significant portion of generated nuclei dissolve back into the solution because the supersaturation level is lowered by the nucleation.[27,28] When the reaction temperature is lowered, the dissolution of nuclei is thermodynamically suppressed, increasing the number of nuclei in the reaction mixture. Given that the crystallization yield is the same, as more particles are generated, the particle size will decrease. To verify the assumption that smaller nanoparticles are synthesized at lower reaction temperatures, a fixed amount of oleyl alcohol was injected into the solution containing iron-oleate complex at the temperatures $\leq$ 280 ^{o}C, where the thermal decomposition of iron-oleate complex is very slow. When oleyl alcohol was injected into the reaction mixture at the temperatures of 250, 260, and 280 ^{o}C, 3, 5, and 11 nm nanoparticles were generated, respectively (Figure 2.10). This result provides a strong evidence for our hypothesis that the synthetic temperature can be lowered by introducing a reduction pathway,

resulting in the formation of the nanoparticles smaller than 3 nm, which was very hard to obtain in the previous synthetic methods.

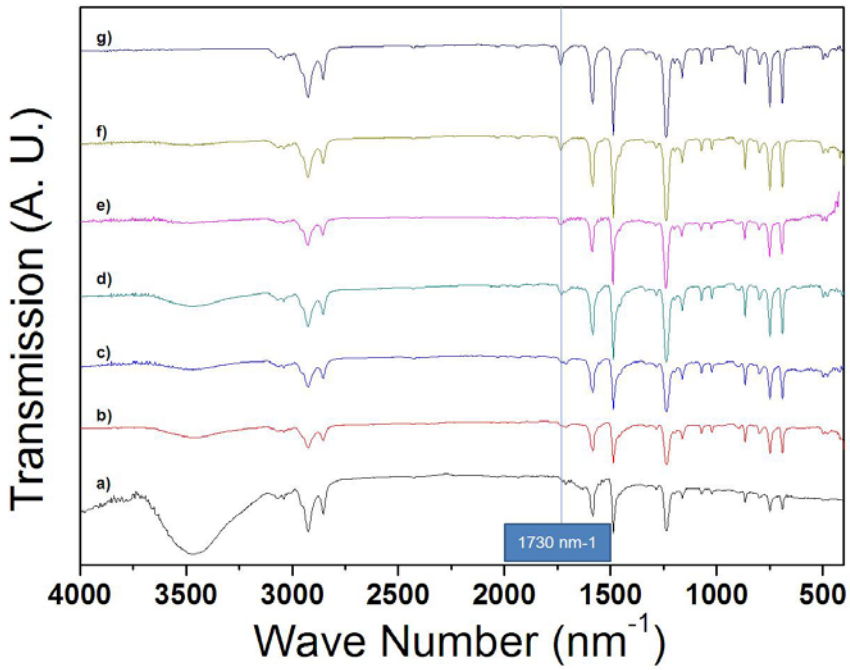

Figure 2.8 FT-IR data of aliquots taken at temperature (a) 70 ^{o}C, (b) 140 ^{o}C, (c) 170 ^{o}C, (d) 200 ^{o}C, (e) 230 ^{o}C, (f) 250 ^{o}C, at 0 min, and (g) 250 ^{o}C, at 5 min during the synthesis. 1710 cm^{-1} peak is assigned to carboxylic acid, and 1730 cm^{-1} peak is assigned to aldehyde. Aldehyde peak begins to appear at 170 ^{o}C, which means that alcohol started to oxidize to aldehyde around 170 ^{o}C.

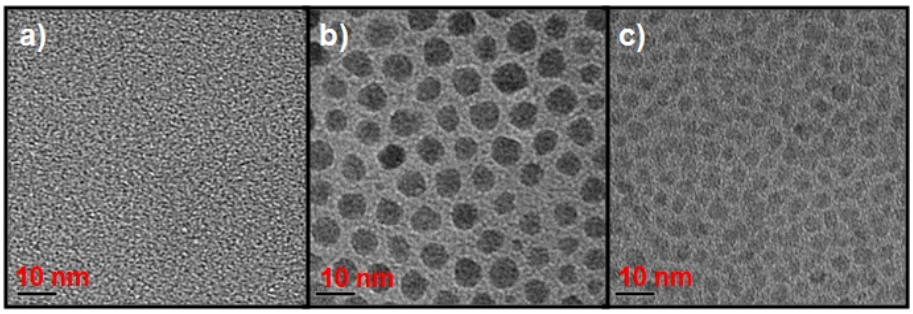

Figure 2.9 TEM images of iron oxide nanoparticles, which were synthesized using the same reaction conditions but varying the reductants; (a) without reductant, (b) oleyl amine, and (c) 1,2-hexadecanediol.

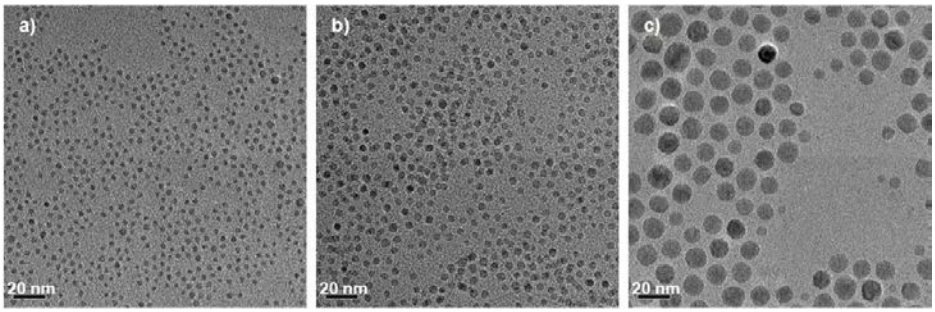

Figure 2.10 Iron oxide nanoparticles synthesized by injecting oleyl alcohol into the mixture composed of iron-oleate complex, oleic acid, and 1-octadecene at the injection temperatures of (a) 250 ^{o}C, (b) 260 ^{o}C, and (c) 280 ^{o}C.

2.3.3 Characterization

2.3.3.1 Structure

XRD pattern of 3 nm nanoparticles revealed maghemite (γ-Fe_2O_3; JCPDS no. 39-1346) crystal structure (Figure 2.11). Although a clear distinction between magnetite and maghemite is difficult because XRD patterns of these two crystal structures are very similar, the XRD pattern matched well with maghemite (Table 2.1). The previous structural characterizations of 4 nm iron oxide nanoparticles using X-ray absorption spectroscopy (XAS) and X-ray magnetic circular dichroism spectroscopy (XMCD) showed that the nanoparticles are predominantly maghemite.[20,21j] When the XRD pattern was compared with that of 12 nm-sized nanoparticles, the peaks of the 3 nm-sized nanoparticles were shifted to higher angles and were broader.[29] The particle size of the nanoparticles calculated by Debye-Scherrer equation from (311) peak was 3.0 nm, which matched very well with that obtained from the TEM image. It means that the nanoparticles are highly crystalline, which can also be identified by HRTEM (Figure 2.12a). Selected area electron diffrantion (SAED) patterns were also assigned to the (311), (440) diffraction of the inverse spinel structure (Figure 2.12b).

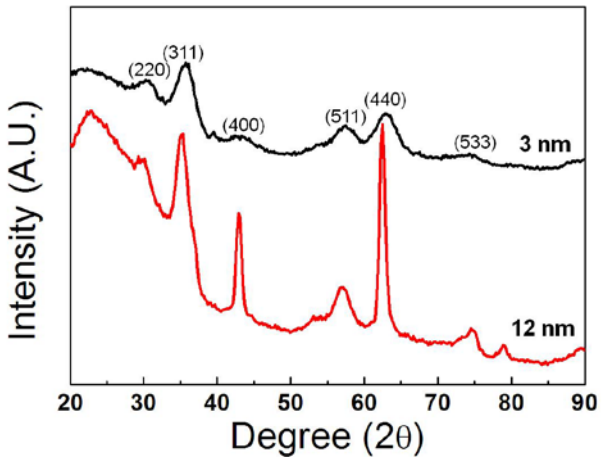

Figure 2.11 XRD patterns of 3 nm and 12 nm iron oxide nanoparticles.

	d-spacing (Å)			
	3 nm-sized Iron Oxide	Maghemite (JCPDS)	Magnetite (JCPDS)	12nm-sized Iron Oxide
(220)	2.952	2.953	2.967	2.975
(311)	2.514	2.518	2.532	2.545
(400)	2.090	2.089	2.099	2.106
(511)	1.606	1.607	1.616	1.616
(440)	1.479	1.476	1.485	1.487
(533)	1.277	1.273	1.281	1.281

Table 2.1 d-spacing values of 3 nm and 12 nm sized iron oxide nanoparticles based on XRD spectra.

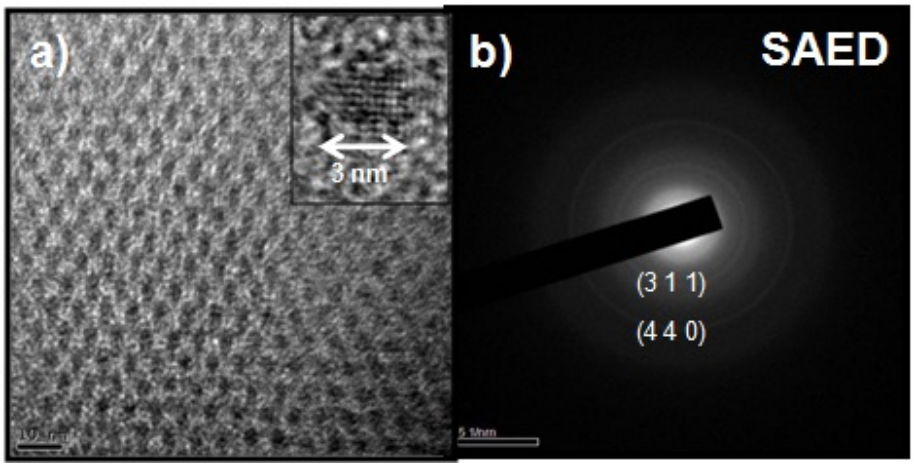

Figure 2.12 HRTEM image and SAED pattern of 3 nm iron oxide nanoparticles.

2.3.3.2 Magnetic Properties

Magnetic properties of 1.5, 2.2, 3, 3.7, and 12 nm iron oxide nanoparticles were measured using vibrating sample magnetometer (VSM). 12 nm nanoparticles were synthesized by following previous reports for the comparison.[20] Magnetic properties of magnetic nanoparticles are strongly dependent on the particle size.[30] Blocking temperature (T_B) is the characteristic temperature where the thermal energy surpasses magnetic anisotropy energy. Peak position in temperature dependent magnetization curve after zero-field-cooling (ZFC M-T) is regarded as T_B. The blocking temperatures of the 12, 3, and 2.2 nm iron oxide nanoparticles were 197, 8, and < 5 K, respectively, measured from ZFC M-T curves (Figure 2.13). The ESIONs had extremely low T_B due to the size dependency of the T_B. Since the magnetic anisotropy energy is related to particle volume, the T_B is proportional to the particle volume as a following equation (Eq. 2.1).[20]

$$KV = 25k_BT_B \qquad \text{(Eq. 2.1)}$$

where K is anisotropy constant, k_B is the Boltzmann's constant and V is the volume of single nanoparticle. The anisotropy constant was calculated by Eq. 2.1 and the results are shown in Figure 2.14. The anisotropy constant increased with decreasing particle size. The results are explained by high surface anisotropy of small sized particles.[20] Size uniformity can also be

confirmed by zero-field-cooling and field-cooling (FC) M-T curves. Conformity between ZFC M-T and M-T curve above T_B demonstrates absence of larger sized particles (Figure 2.13).

Field dependent magnetization (M-H) curves of the 1.5, 2.2, 3, and 12 nm iron oxide nanoparticles are shown in Figure 2.15. Hysteresis was observed in M-H curve of 12 nm particles measured at 5 K but it was not observed forESIONs. Coercivity and remanence of ESIONs are negligible even at 5 K due to their very low crystal anisotropy. The M-T data of ESIONs supported low T_B.

The magnetic properties at room temperature are of importance due to the fact that MRI diagnosis is always conducted at room temperature. For the comparison purpose, M-H curves (measured at 300 K) of 1.5, 2.2, 3 and 12 nm iron oxide particles are superimposed in Figure 2.16. As the size of iron oxide nanoparticles decreases, the magnetization at 300 K tends to dramatically decrease (Figure 2.16). Magnetization of 1.5 nm ESIONs exhibited linear relationship with applied field, which is characteristic of paramagnetic material. The tendancy can be explained by high surface area and small particle volume.

The spin canting effect is the phenomenon of the lack of full alignment of the spins in surface atoms due to the difference of alignment of surface states

as compared to bulk.[2,3] Extremely large surface area of ESIONs leads to enourmous spin canting effect on the ESIONs. According to the provious report, depth of spin canted layer is presumed to be 0.9 nm.[3] Then, 93.6% of spins in 3 nm ESIONs are expected to be canted while only 38.6% of spins are canted in 12 nm nanoparticles. In the case of 2.2 nm ESIONs, 99.4% of the spins are canted. The extremely small magnetizations of ESIONs are attributed to the small portion of magnetic core.[31]

The unique magnetic properties of ESIONs can also be explained by small magnetic moment. The magnetic moment of nanoparticles were calculated by Eq. 2.2,

$$m = M\rho V \qquad \text{(Eq. 2.2)}$$

where M is the mass magnetization of the particle (emu g^{-1}) and ρ is the density of particles (4.87 g cm^{-3} for maghemite), taking the particles as spherical, the magnetic moment at room temperature of 1.5, 2.2, 3, and 12 nm iron oxide nanoparticles were 3.91, 83.9, 273, and 24800 μ_B, respectively.[32] If the particles are uniform, the magnetization follows the Langevin function (Eq. 2.3),[32]

$$M/M\text{s} = cot\ \alpha - 1/\alpha\ (\alpha = \mu_0 mH/k_B T) \qquad \text{(Eq. 2.3)}$$

where μ_0 is the permeability of empty space, H is the magnetic field, and m is the magnetic moment of single particle. According to the Langevin

function, the particles having low magnetic moment is expected to exhibit low magnetization.

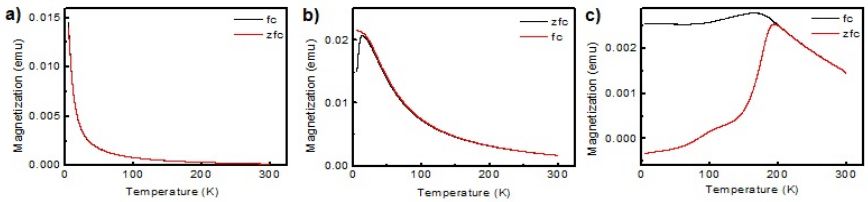

Figure 2.13 Temperature dependent magnetization curves (M-T) for (a) 2.2 nm, (b) 3 nm, and (c) 12 nm iron oxide nanoparticles measured after zero-field-cooling (ZFC) and field-cooling (FC) at the applied field of 100 Oe. The magnetization data were normalized with the value at the maximum of ZFC magnetization.

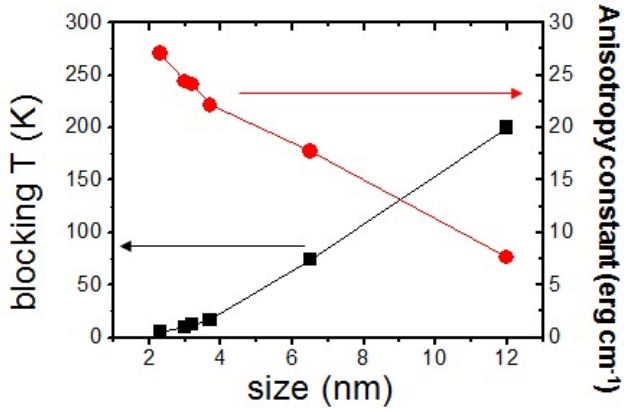

Figure 2.14 Size-dependancy of blocking temperature (squares) and anisotropy constant (dots).

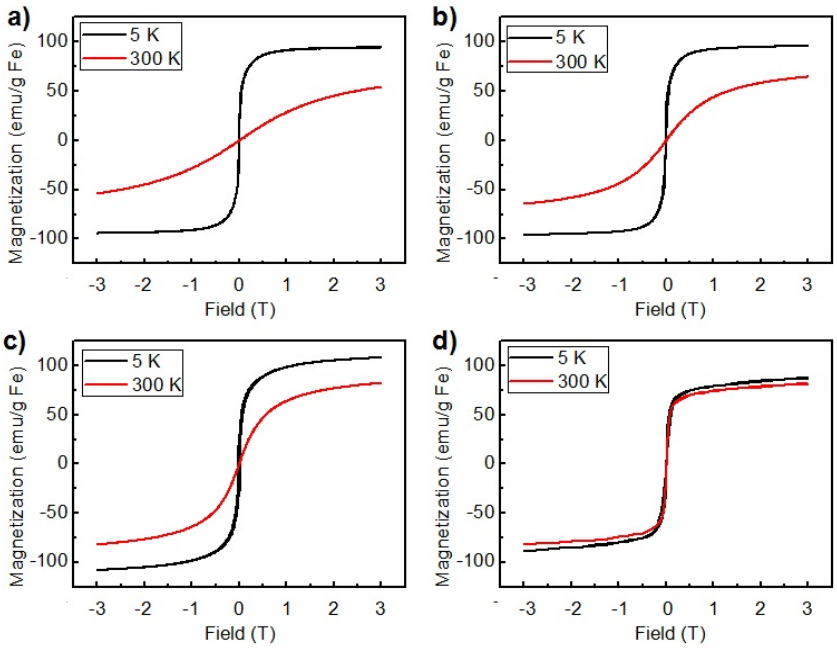

Figure 2.15 Field dependence of magnetization curves (M-H) at 5 K and 300 K for (a) 1.5, (b) 2.2, (c) 3, and (d) 12 nm iron oxide nanoparticles. The weight fractions of iron oxide core were estimated by TGA.

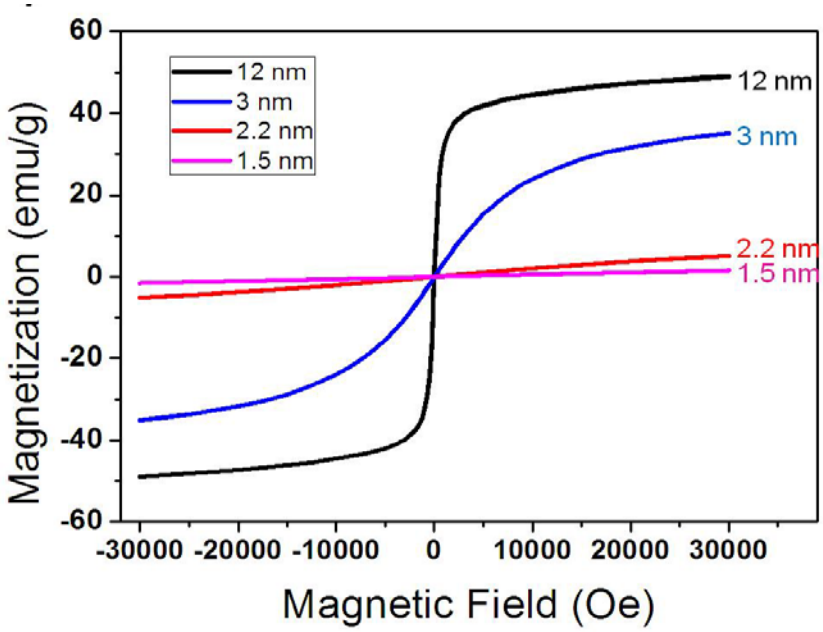

Figure 2.16 Field dependent magnetization curves (M-H) at 300 K for 1.5, 2.2, 3, and 12 nm iron oxide nanoparticles.

2.3.4 Water Transfer

Since as-synthesized ESIONs are capped by long chain oleic acid, surface modification of the hydrophobic particles is required for further biomedical application. Surface modification of ESIONs can be achieved by encapsulation or ligand exchanging reaction with poly ethyleneglycol (PEG)., During the surface modification, aggregation of particle has to be minimized since the aggregation can cause T_2 enhancement.[33]

To endow water compatibility, ESIONs were encapsulated by phospholipid-PEG using reported method.[25] Excess amount of phospholipids-PEG were reacted to cover extremely large surface area.[13c] Hydrodynamic diameter of phospholipids-PEG capped 3 nm nanoparticles was 9.0 nm (Figure 2.17c).

Hydrophillic ESIONs can also be obtained by exchanging oleic acid surfactant with phosphine oxide-derivatized PEG (PO-PEG).[23,24] To minimize particle aggregation, ligand exchange reaction was conducted in two phase. Nanoparticles were mixed with PO-PEG in ethanol and heptane (1:1) solvent and incubated at 70 °C. PO-PEG-stabilized ESIONs were dispersed in ethanol layer, while extracted oleic acid, which can induce aggregation of particles, was isolated in heptane layer. Hydrodynamic diameter of the PO-PEG capped 3 nm iron oxide nanoparticles were 15 nm

(Figure 2.17c). The water-dispersity is also confirmed by TEM (Figure 2.17a,b).

The in vitro cytotoxicity of water-compatible 3 nm iron oxide nanoparticles was evaluated by calcein-acetoxymethyl ester (AM)/ propium iodide (PI) (Figure 2.18) and 7-Aminoactinomycin D (AAD) (Figure 2.19) assays. No available toxic response was observed with iron concentration less than 100 mg/mL in MCF-7 cell. Since iron is known as nontoxic inorganic element, the water-compatible small size iron oxide nanoparticles have low toxicity even at significant concentrations.

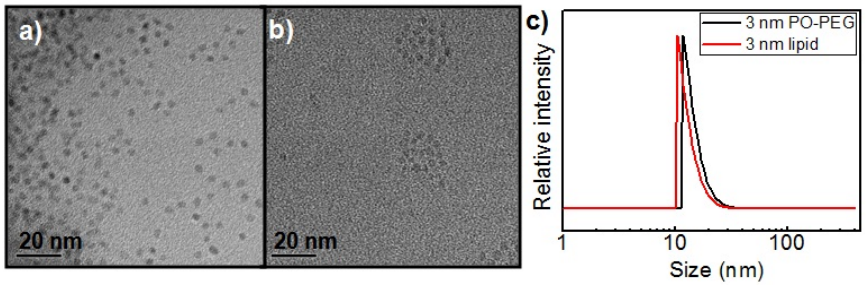

Figure 2.17 (a-b) TEM images of water-dispersible ESIONs stabilized by (a) phospholipid-PEG and (b) PO-PEG. (c) Number average hydrodynamic diameters of phospholipid-PEG- and PO-PEG-stabilized 3 nm ESIONs measured by DLS.

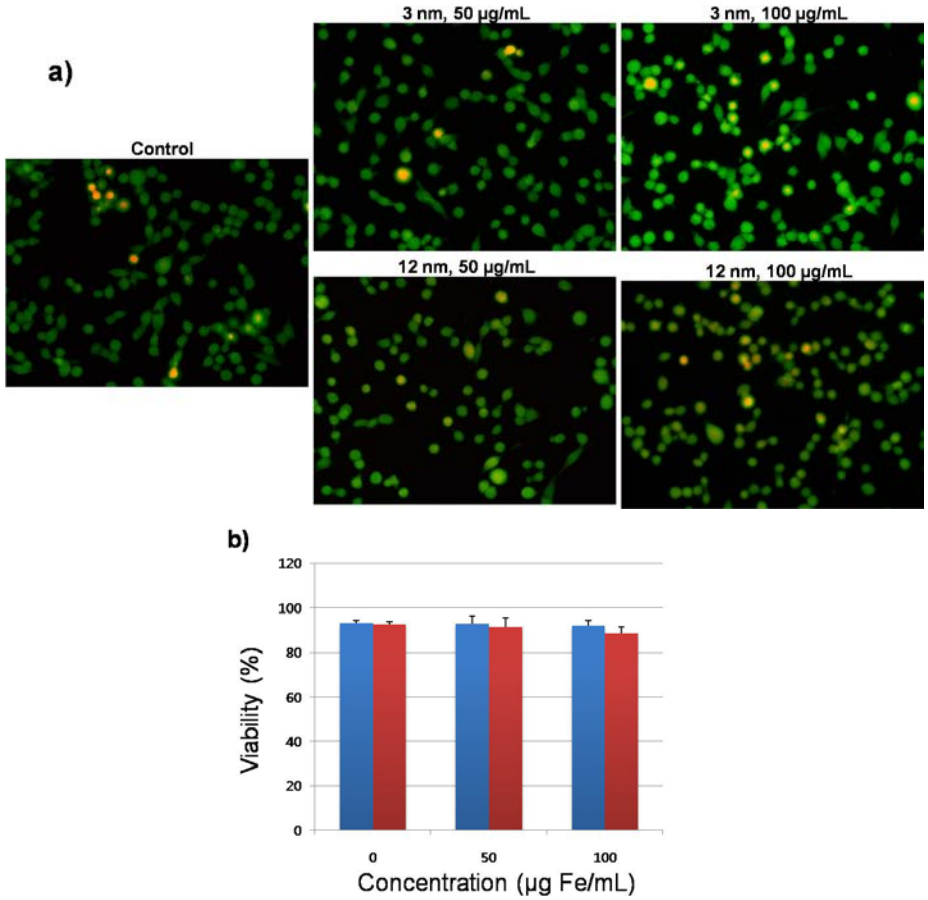

Figure 2.18 (a) Confocal microscopy images of calcein-AM/PI treated cells incubated with 3 and 12 nm iron oxide nanoparticles. Green colored cells represent live cells and red colored cells represent dead cells. (b) Cell viability of 3 (left; blue) and 12 nm (right; red) iron oxide nanoparticles with calcein-AM/PI assay.

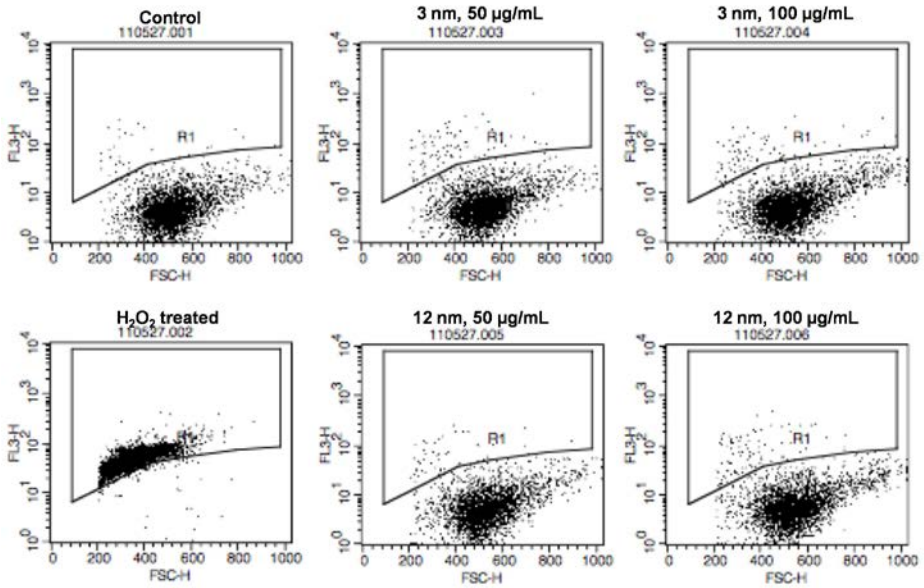

Figure 2.19 Flow cytometric analysis of cytotoxicity of 3 and 12 nm iron oxide nanoparticles through 7-AAD assays. Inner part of quadrangle represents dead cells and the outer part is live cells.

2.3.5 MRI Application

The hydrophilic ESIONs have a potential to be a good T_1 MRI contrast agent because they have low magnetic moment, 5 unpaired electrons, high surface area, and low toxicity. T_1 contrast agent should have both of low r_2/r_1 ratio of high r_1 relaxivity and low r_2.[23] To examine size dependency of relaxivity, various size (2.2, 3.0, 6.5, 12 nm) of the water-dispersible iron oxide nanoparticles were prepared. The relaxivity is defined as slope of inverse of relaxation time versus concentration (Eq. 2.2).[23]

$$1/T_i = 1/T_{i,0} + r_i \cdot C \qquad \text{(Eq.2.2)}$$

where T_i is relaxation time; i = 1 (longitudinal relaxivation) and i = 2 (transverse relaxation), and C is concentration of contrast agents.

Relaxivities of phospholipid-PEG-capped nanoparticles were obtained by relaxation time of various concentrations (0.9, 0.45, 0.22, 0.11, 0.056 mM of Fe) of nanoparticles. The r_1 relaxivities of 2.2, 3.0, 6.5, 12 nm iron oxide particles were 1.69, 1.77, 1.57, and 1.27 $mM^{-1}s^{-1}$, respectively (Table 2.2). As the particle size decreased, the r_1 values slightly increased because smaller particles have larger surface area. The r_2 values of 2.2, 3.0, 6.5, 12 nm iron oxide particles were 13.2, 28.1, 32.3, and 79.1 $mM^{-1}s^{-1}$, respectively. As the particle size increases, the r_2 values increases dramagically. The high magnetic moment of larger sized magnetic particles caused strong T_2 signal,

thus induced susceptibility effect. Combining the size-dependency of r_1 and r_2, we found that smaller sized iron oxide nanoparticles showed much low r_2/r_1 ratio.

The r_1 values of 2.2, 3.0, 6.5 and 12 nm PO-PEG-stabilized iron oxide particles were 6.02, 4.60, 4.64, and 3.14 $mM^{-1}s^{-1}$, respectively and the r_2 values of these particles were 16.1, 32.7, 48.6, and 89.6 $mM^{-1}s^{-1}$, respectively (Table 2.3). PO-PEG-stabilized iron oxide nanoparticles also showed size-dependent relaxation properties similar to relaxivity of phospholipid-stabilized particles. We also found that the r_1 values of PO-PEG-stabilized iron oxide nanoparticles were 2~4 times higher than those of phospholipid-PEG-stabilized particles. The result indicates that ligand is also important factor besides core particles. The high r_1 value of PO-PEG-stabilized ESIONs is caused by fast water exchange rate. Because T_1 relaxation process of water occurs dominantly in the inner sphere of contrast agents, water exchange rate has positive effect on r_1 relaxivity.[10] Water molecules can interact easily with PO-PEG-stabilized iron oxide nanoparticles because these particles have no hydrophobic layer. On the other hand the hydrophobic layer in phospholipids-PEG-stabilized nanoparticles act as a barrier to prevent water contact with nanoparticle surface.[33] Therefore, PO-PEG-stablized nanoparticles showed higher r_1

value about 4 ~ 6 $mM^{-1}s^{-1}$. The relaxivity is higher than the reported values of other T_1 contrast agents and similar to the value of commercial gadolinium complexes.[10] The r_2/r_1 ratios of 2.2 and 3 nm PO-PEG-stabilized ESIONs were 2.67 and 7.11, respectively. The low r_2/r_1 ratio demonstrated that the PO-PEG-stabilized ESIONs are appropriate T_1 contrast agents.

For *in vivo* MR imaging, 3 nm ESIONs were injected into a mouse through its tail vein. On ESION-enhanced T_1 weighted MR images, blood vessels were brightened which was maintained for more than 2 min. Various blood vessels including aortic arch, jugular vein, and carotid artery were observed by imaging (Figure 2.20a,b). On the other hand, on gadolinium complex (Gadovist)-enhanced MR image, bright signal of blood vessels were weakened within 2 min (Figure 2.20c,d). ESIONs have long circulation times since they are not taken up by reticuloendothelial system and excreted by kidney due to optimal hydrodynamic diameter of nanoparticles (15 nm).[34]

Table 2.2 Relaxation properties of the phospholipid-stabilized iron oxide nanoparticles.

Size	r_1 ($mM^{-1}s^{-1}$)	r_2 ($mM^{-1}s^{-1}$)	r_2/r_1
2.2 nm	1.69	13.2	7.81
3.0 nm	1.77	28.1	15.9
6.5 nm	1.57	32.3	20.6
12 nm	1.27	79.14	62.3

Table 2.3 Relaxation properties of the PO-PEG capped iron oxide nanoparticles.

Size	r_1 ($mM^{-1}s^{-1}$)	r_2 ($mM^{-1}s^{-1}$)	r_2/r_1
2.2 nm	6.02	16.1	2.67
3.0 nm	4.60	32.7	7.11
6.5 nm	4.64	48.6	10.5
12 nm	3.14	89.6	28.5

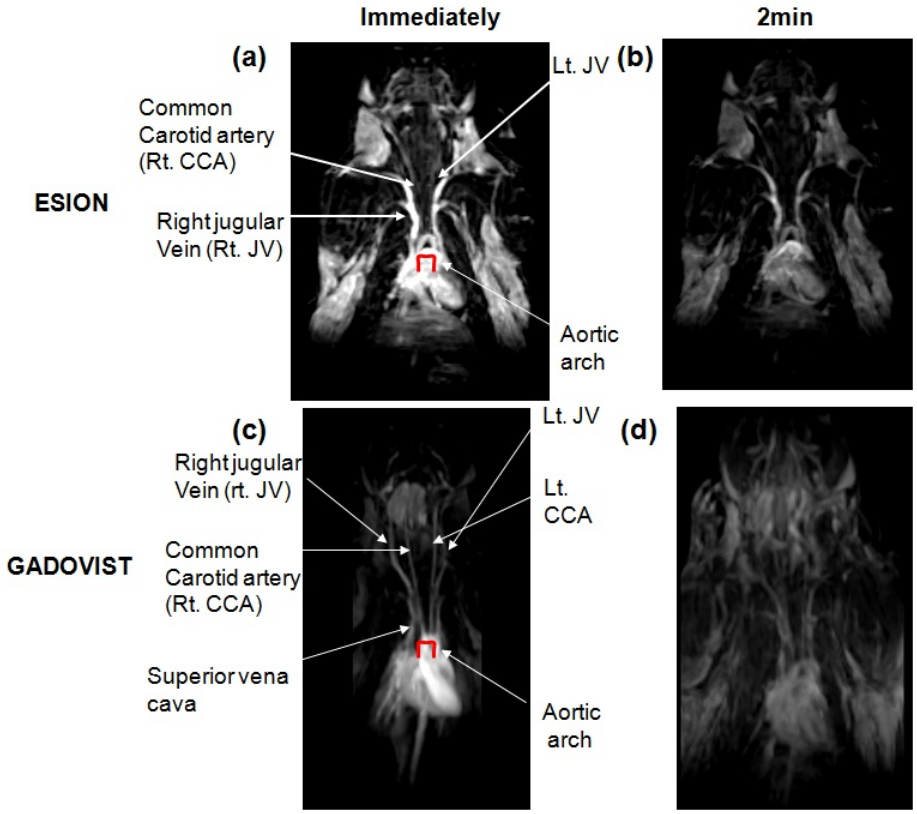

Figure 2.20 (a,b) ESION- and (c,d) gadovist-enhanced blood pool T_1 MR imaging.

2.4 Conclusion

In conclusion, extremely small-sized iron oxide nanoparticles (ESIONs) with the size ranges of 1.5 – 3.7 nm were synthesized by thermal decomposition of iron-oleate complexes in the presence of oleyl alcohol. The current synthetic procedure is very simple and can be easily scaled up to produce multigrams of nanoparticles. The resulting nanoparticles were highly uniform. XRD pattern of ESIONs revealed maghemite crystal structure. These nanoparticles exhibited very low magnetization due to low magnetic moment and spin canting effect. Surface of the hydrophobic nanoparticles were modified with phospholipid-PEG and PO-PEG to disperse in water. Calcein AM/PI staining and 7-AAD assays of ESIONs revealed that the nanoparticles are non-toxic up to high concentration. PO-PEG-stabilized ESIONs showed high r_1 relaxivities and low r_2/r_1 ratios. Various blood vessels could be observed in the ESION-enhanced T_1-weighted MRI. ESION have a potential to replace commonly used gadolinium complexes because of their high r_1 relaxivity, low r_2/r_1 ratio, low toxicity, long blood circulation time, and low synthetic cost.

2.5 References

[1] (a) Hyeon, T. *Chem. Commun*. **2003,** 927. (b) Park, J.; Joo, J.; Kwon, S. G.; Jang, Y.; Hyeon, T. *Angew. Chem. Int. Ed.* **2007**, *46*, 4630. (c) Gu, H.; Xu, K.; Xu, C.; Xu, B. *Chem. Commun.* **2006**, 941. (d) Sun, S. *Adv. Mater.* **2006**, *18*, 393. (e) Jeong, U.; Teng, X.; Wang, Y.; Yang, H.; Xia, Y. *Adv. Mater.* **2007**, *19*, 33. (f) Jun, Y.-w.; Choi, J.-s.; Cheon, J. *Angew. Chem. Int. Ed*. **2006**, *45*, 2. (g) Jun, Y.-w.; Choi, J.-s.; Cheon, J. *Chem. Commun.* **2007**, 1203. (h) Lu, A.-H.; Salabas, E. L.; Schüth, F. *Angew. Chem. Int. Ed.* **2007**, *46*, 1222. (i) Wang, X.; Li, Y. *Chem. Commun.* **2007**, 2901. (j) Niederberger, M.; Garnweitner, G. *Chem. Eur. J.* **2006**, *12*, 7282.

[2] (a) Coey, J. M. D. *Phys. Rev. Lett.* **1971,** *27*, 1140. (b) Yang, H.; Ogawa, T.; Hasegawa, D.; Takahashi, M. *J. Appl. Phys.* **2008,** *103*, 07D526.

[3] Linderoth, S.; Hendriksen, P. V.; Bødker, F.; Wells, S.; Davies, K.; Charles, S. W.; Mørup, S. *J. Appl. Phys.* **1994,** *75*, 6583.

[4] Na, H. B.; Hyeon, T. *J. Mater. Chem.* **2009,** *19*, 6267.

[5] Brown, M. A.; Semelka, R. C. *MRI: Basic Principles and Applications*; Wiley-Liss: New York, **2003**.

[6] Na, H. B.; Song, I. C.; Hyeon, T. *Adv. Mater.* **2009,** *21*, 2133.

[7] (a) Bulte, J. W. M.; Kraitchman, D. L. *NMR Biomed.* **2004,** *17*, 484. (b) Wang, Y.-X. J.; Hussain, S. M.; Krestin, G. P. *Eur. Radiol.* **2001,** *11*, 2319. (c) Reimer, P.; Tombach, B. *Eur. Radiol.* **1998,** *8*, 1198. (d) Jun, Y.-w.; Huh, Y.-M.; Choi, J.-s.; Lee, J.-H.; Song, H.-T.; Kim, S.; Yoon, S.; Kim, K.-S.; Shin, J.-S.; Suh, J.-S.; Cheon, J. *J. Am. Chem. Soc.* **2005,** *127*, 5732. (e) Jun, Y.-w.; Seo, J.-W.; Cheon, J. *Acc. Chem. Res.* **2008,** *41*, 179. (f) Gao, J.; Liang, G.; Cheung, J. S.; Pan, Y.; Kuang, Y.; Zhao, F.; Zhang, B.; Zhang, X.; Wu, E. X.; Xu, B. *J. Am. Chem. Soc.* **2008,** *130*, 11828. (g) Brooks, R. A. *Magn. Reson. Med.* **2002,** *47*, 388. (h) Weissleder, R.; Elizondo, G.; Wittenberg, J.; Rabito, C. A.; Bengele, H. H.; Josephson, L. *Radiology* **1990,** *175*, 489. (i) Weissleder, R.; Moore, A.;

Mahmood, U.; Bhorade, R.; Benveniste, H.; Chiocca, E. A.; Basilion, J. P. *Nat. Med.* **2000,** *6*, 351.

[8] Huh, Y.-M.; Jun, Y.-w.; Song, H.-T.; Kim, S.; Choi, J.-s.; Lee, J.-H.; Yoon, S.; Kim, K.-S.; Shin, J.-S.; Suh, J.-S.; Cheon, J. *J. Am. Chem. Soc.* **2005,** *127*, 12387.

[9] Lee, N.; Kim, H.; Choi, S. H.; Park, M.; Kim, D.; Kim, H.-C.; Choi, Y.; Lin, S.; Kim, B. H.; Jung, H. S.; Kim, H.; Park, K. S.; Moon, W. K.; Hyeon, T. *Proc. Natl. Acad. Sci. U.S.A.* **2011,** *108*, 2662.

[10] Caravan, P. *Chem. Soc. Rev.* **2006,** *35*, 512.

[11] Penfield, J. G.; Reilly, R. F. *Nat. Clin. Pract. Nephrol.* **2007**, *3*, 654.

[12] (a) Warsi, M. F.; Adams, R. W.; Duckett S. B.; Chechik, V. *Chem. Commun.* **2010,** *46*, 451. (b) Endres, P. J.; Paunesku, T.; Vogt, S.; Meade, T. J.; Woloschak, G. E. *J. Am. Chem. Soc.* **2007,** 129, 15760. (c) Taylor, K. M. L.; Kim, J. S.; Rieter, W. J.; An, H.; Lin, W.; Lin, W. *J. Am. Chem. Soc.* **2008,** 130, 2154. (d) Rieter, W. J.; Kim, J. S.; Taylor, K. M. L.; An, H.; Lin, W.; Tarrant, T.; Lin, W. *Angew. Chem., Int. Ed.* **2007,** *46*, 3680. (e) Kim, J. S.; Rieter, W. J.; Taylor, K. M. L.; An, H.; Lin, W.; Lin, W. *J. Am. Chem. Soc.* **2007,** *129*, 8962.

[13] (a) Hifumi, H.; Yamaoka, S.; Tanimoto, A.; Citterio, D.; Suzuki. K. *J. Am. Chem. Soc.* **2006,** *128*, 15090. (b) Park, Y. I. et al. *Adv. Mater*. **2009,** *21*, 4467. (c) Bridot, J.-L.; Faure, A.-C.; Laurent, S.; Rivière, C.; Billotey, C.; Hiba, B.; Janier, M.; Josserand, V.; Coll, J.-L.; Elst, L. V.; Muller, R.; Roux, S.; Perriat, P.; Tillement, O. *J. Am. Chem. Soc.* **2007,** *129*, 5076.

[14] (a) Na, H. B.; Lee, J. H.; An, K.; Park, Y. I.; Park, M.; Lee, I. S.; Nam, D.-H.; Kim, S. T.; Kim, S.-H.; Kim, S.-W.; Lim, K.-H.; Kim, K.-S.; Kim, S.-O.; Hyeon, T. *Angew. Chem., Int. Ed.* **2007,** *46*, 5397. (b) Yu, T.; Moon, J.; Park, J.; Park, Y. I.; Na, H. B.; Kim, B. H.; Song, I. C.; Moon, W. K.; Hyeon, T. *Chem. Mater.* **2009,** *21*, 2272. (c) Choi, S.-H.; Na, H. B.; Park, Y. I.; An, K.; Kwon, S. G.; Jang, Y.; Park, M.; Moon, J.; Son, J. S.; Song, I. C.; Moon, W. K.; Hyeon, T.

J. Am. Chem. Soc. **2008,** *130,* 15573. (d) An, K.; Kwon, S. G.; Park, M.; Na, H. B.; Baik, S.-I.; Yu, J. H.; Kim, D.; Son, J. S.; Kim, Y. W.; Song, I. C.; Moon, W. K.; Park, H. M.; Hyeon, T. *Nano Lett.* **2008,** *8,* 4252. (e) Gilad, A. A.; Walczak, P.; McMahon, M. T.; Na, H. B.; Lee, J. H.; An, K.; Hyeon, T.; van Zijl, P. C. M.; Bulte, J. W. M. *Magn. Reson. Med.* **2008,** *60,* 1. (f) Yang, H.; Zhuang, Y.; Hu, H.; Du, X.; Zhang, C.; Shi, X.; Wu, H.; Yang, S. *Adv. Funct. Mater.* **2010,** *20,* 1733. (g) Kim, T.; Momin, E.; Choi, J.; Yuan, K.; Zaidi, H.; Kim, J.; Park, M.; Lee, N.; McMahon, M. T.; Quinones-Hinojosa, A.; Bulte, J. W. M.; Hyeon, T.; Gilad, A. A. *J. Am. Chem. Soc.* **2011,** *133,* 2955.

[15] Limbach, L. K.; Wick, P.; Manser, P.; Grass, R. N.; Bruinink, A.; Stark, W. J. *Environ. Sci. Technol.* **2007,** *41,* 4158.

[16] Roch, A.; Muller, R. N.; Gillis, P. *J. Chem. Phys.* **1999,** *110,* 5403.

[17] (a) Kodama, R. H. *J. Magn. Magn. Mater.* **1999,** *200,* 359. (b) Moser A.; Takano, K.; Margulies, D. T.; Albrecht, M.; Sonobe, Y.; Ikeda, Y.; Sun, S.; Fullerton, E. E. *J. Phys. D: Appl. Phys.* **2002,** *35,* R157. (c) Jun, Y.-w.; Lee, J.-H.; Cheon, J. *Angew. Chem., Int. Ed.* **2008,** *47,* 5122.

[18] (a) Taboada, E.; Rodríguez, E.; Roig, A.; Oró, J.; Roch, A.; Muller, R. N. *Langmuir* **2007,** *23,* 4583. (b) Tromsdorf, U. I.; Bruns, O. T.; Salmen, S. C.; Beisiegel, U.; Weller, H. *Nano Lett.* **2009,** *9,* 4434.

[19] Ouakssim, A.; Roch, A.; Pierart, C.; Muller, R. N. *J. Magn. Magn. Mater.* **2002,** *252,* 49.

[20] Park, J.; An, K.; Hwang, Y.; Park, J.-G.; Noh, H.-J.; Kim, J.-Y.; Park, J.-H.; Hwang, N.-M.; Hyeon, T. *Nat. Mater.* **2004,** *3,* 891.

[21] (a) Sun, S.; Zeng, H. *J. Am. Chem. Soc.* **2002,** *124,* 8204. (b) Sun, S.; Zeng, H.; Robinson, D. B.; Raoux, S.; Rice, P. M.; Wang, S. X.; Li, G. *J. Am. Chem. Soc.* **2004,** *126,* 273. (c) Peng, S.; Sun, S. *Angew. Chem., Int. Ed.* **2007,** *46,* 4155. (d) Hyeon, T.; Lee, S. S.; Park, J.; Chung, Y.; Na, H. B. *J. Am. Chem. Soc.* **2001,** *123,* 12798. (e) Hyeon, T. *Chem. Commun,* **2003,** 927. (f) Laurent, S.; Forge, D.;

Port, M.; Roch, A.; Robic, C.; Elst, L. V.; Muller, R. N. *Chem. Rev.* **2008,** *108,* 2064. (g) Park, J.; Joo, J.; Kwon, S. G.; Jang, Y.; Hyeon, T. *Angew. Chem., Int. Ed.* **2007,** *46,* 4630. (h) Jana, N. R.; Chen, Y.; Peng, X. *Chem. Mater.* **2004,** *16,* 3931. (i) Yu, W. W.; Falkner, J. C.; Yavuz, C. T.; Colvin, V. L. *Chem. Commun.* **2004,** 2306. (j) Park, J.; Lee, E.; Hwang, N.-M.; Kang, M.; Kim, S. C.; Hwang, Y.; Park, J.-G.; Noh, H.-J.; Kim, J.-Y.; Park, J.-H.; Hyeon, T. *Angew. Chem., Int. Ed*. **2005,** *44,* 2872. (k) Jeong, U.; Teng, X.; Wang, Y.; Yang, H.; Xia, Y. *Adv. Mater.* **2007,** *19,* 33. (l) Kovalenko, M. V.; Bodnarchuk, M. I.; Lechner, R. T.; Hesser, G.; Schäffler, F.; Heiss, W. *J. Am. Chem. Soc.* **2007,** *129,* 6352. (m) Cheon, J.; Kang, N.-J.; Lee, S.-M.; Lee, J.-H.; Yoon, J.-H.; Oh, S. J. *J. Am. Chem. Soc.* **2004,** *126,* 1950. (n) Redl, F. X.; Black, C. T.; Papaefthymiou, G. C.; Sandstrom, R. L.; Yin, M.; Zeng, H.; Murray, C. B.; O'Brien, S. P. *J. Am. Chem. Soc.* **2004,** *126,* 14583. (o) Rockenberger, J.; Scher, E. C.; Alivisatos, A. P. *J. Am. Chem. Soc.* **1999,** *121,* 11595. (p) Kim, D.; Lee, N.; Park, M.; Kim, B. H.; An, K.; Hyeon, T. *J. Am. Chem. Soc.* **2009,** *131,* 454.

[22] (a) Teng, X.; Yang, H. *J. Mater. Chem.* **2004,** *14,* 774. (b) Lee, Y.; Lee, J.; Bae, C. J.; Park, J.-G.; Noh, H.-J.; Park, J.-H.; Hyeon, T. *Adv. Funct. Mater.* **2005,** *15,* 503.

[23] Na, H. B.; Lee, I. S.; Seo, H.; Park, Y. I.; Lee, J. H.; Kim, S.-W.; Hyeon, T. *Chem. Commun.* **2007,** 5167.

[24] Boyer, J.-C.; Manseau, M.-P.; Murray, J. I.; van Veggel, F. C. J. M. *Langmuir* **2010,** *26,* 1157.

[25] Dubertret, B.; Skourides, P.; Norris, D. J.; Noireaux, V.; Brivanlou, A. H.; Libchaber, A. *Science* **2002**, *298,* 1759.

[26] (a) Adireddy, S.; Lin, C.; Palshin, V.; Dong, Y.; Cole, R.; Caruntu, G. *J. Phys. Chem. C* **2009,** *113,* 20800. (b) Teranishi, T.; Miyake, M. *Chem. Mater.* **1998,** *10*, 594. (c) Zeng, Y.; Hao, R.; Xing, B.; Hou, Y.; Xu, Z. *Chem. Commun.* **2010,** *46,* 3920. (d) Wang, D.; Li, Y. *J. Am. Chem. Soc.* **2010,** *132,* 6280.

[27] Kwon, S. G.; Piao, Y.; Park, J.; Angappane, S.; Jo, Y.; Hwang, N.-M.; Park, J.-G.; Hyeon, T. *J. Am. Chem. Soc.* **2007,** *129,* 12571.

[28] van Embden, J.; Mulvaney, P. *Langmuir* **2005,** *21,* 10226.

[29] Cullity, B. D.; Stock, S. R. *Element of X-Ray Diffraction, 3rd Ed.*; Prentice Hall: New York, **2001**.

[30] (a) Chantrell, R. W.; Popplewell, J.; Charles, S. W. *IEEE Trans. Magn.* **1978,** *MAG-14,* 975. (b) Roca, A. G.; Marco, J. F.; Morales, M. P.; Serna, C. J. *J. Phys. Chem. C* **2007,** *111,* 18577. (c) Goya, G. F.; Berquó, T. S.; Fonseca, F. C.; Morales, M. P.; *J. Appl. Phys.* **2003,** *94,* 3520.

[31] Müller, R.; Hergt, R.; Dutz, S.; Zeisberger, M.; Gawalek, W. *J. Phys.: Condens. Matter* **2006,** *18,* S2527.

[32] Jiles, D. *Introduction to Magnetism and Magnetic Materials, 2nd Ed.*; Chapman & Hall: London, **1998**.

[33] (a) Roch, A.; Gossuin, Y.; Muller, R. N.; Gillis, P. *J. Magn. Magn. Mater.* **2005,** *293,* 532. (b) Perez, J. M.; Joshephson, L.; O'Loughlin, T.; Högemann, D.; Weissleder, R. *Nat. Biotechnol.* **2002,** *20,* 816. (c) Matsumoto, Y.; Jasanoff, A. *Magn. Reson. Imaging* **2008,** *26,* 994.

[34] Pouliquen, D.; Le Jeune, J. J.; Perdrisot, R.; Ermias, A.; Jallet, P. *Magn. Reson. Imaging* **1991**, *9,* 275.

Chapter 3. Sizing by Weighing: Characterizing Sizes of Extremely Small-sized Iron Oxide Nanoparticles Using MALDI-TOF Mass Spectrometry

3.1 Introduction

Precise measuring of the sizes and size distributions of ultra-small-sized nanoparticles is very important for both fundamental property characterizations and technological applications because nanoparticles exhibit characteristic size-dependent electrical, optical, magnetic, and chemical properties.[1] Transmission electron microscopy (TEM) is one of the most popularly employed techniques to measure the size of nanoparticles. However, obtaining TEM images and subsequent extraction of size information is a laborious and time-consuming process. Furthermore, it is very difficult to obtain high-quality TEM images of nanoparticles of < 2 nm, and it is nearly impossible to get TEM images of clusters of < 1 nm.[2]

Although fitting line-broadening of powder X-ray diffraction (XRD) patterns to the Scherer equation has been used to calculate nanoparticle sizes, the acquired size data is inherently inaccurate, and it is therefore impossible to obtain size distribution data.[3a] Other size characterization methods including dynamic light scattering (DLS) and small-angle X-ray scattering (SAXS) cannot accurately measure small-sized nanoparticles of < 5 nm.[3b,c]

Iron oxide nanoparticles exhibit very interesting size-dependent magnetic properties, and recently uniform-sized iron oxide nanoparticles with controlled sizes have been intensively investigated as magnetic resonance imaging (MRI) contrast agents.[4-5] For example, superparamagnetic iron oxide nanoparticles of 5 to 20 nm have been used as T_2 MRI contrast agents for diagnosis of cancers.[4d] 50 nm ferrimagnetic iron oxide nanoparticles (FION) were employed as MRI contrast agents for single cells and transplanted pancreas islet cells.[4e] Extremely small-sized iron oxide nanoparticles in the range of 1 to 5 nm, comprising of 100 to 10000 atoms, exhibit intermediate property between paramagnetic iron-oxo clusters and super-paramagnetic iron oxide nanoparticles.[5,6] Recently, uniform 3 nm iron oxide nanoparticles were developed as a highly sensitive T_1 MRI contrast agent for imaging blood vessels of < 0.2 mm.[5]

Understanding the nanoparticle formation mechanisms including

nucleation and growth processes is very important for developing new synthetic methods to obtain nanoparticles with desired characteristics.[7-9] For these mechanistic studies, the collection of size distribution data is critical. UV-visible absorption and photoluminescence spectroscopies have been successfully used to understand the formation mechanisms of semiconductor nanoparticles.[7] However, the elucidation of the formation mechanism of non-fluorescent nanoparticles, such as iron oxide nanoparticles is extremely difficult because there are no readily available tools to acquire size data of these oxide nanoparticles. In particular, the sizes of oxide nanoparticles smaller than 2 nm are hard to determine accurately.

Various mass spectrometric methods have been employed to characterize clusters and nanoparticles.[10] Most of the mass spectrometric characterizations have been focused on gold clusters, while there are only few reports on oxide nanoparticles of few nanometers. Herein, we report on the accurate characterization of sizes and size distributions of iron oxide nanoparticles of <5 nm using MS. Furthermore, we could use this mass spectrum technique to investigate the formation mechanism of extremely small iron oxide nanoparticles. Among the various MS techniques, MALDI-TOF MS was employed because the use of the matrix in the MALDI technique keeps the nanoparticles intact from fragmentation during the

ionization step and the TOF analyzer can theoretically cover an infinite range of masses.[11]

3.2 Experimental Section

3.2.1. Chemicals

90% oleic acid, 98% iron chloride hexahydrate ($FeCl_3 \cdot 6H_2O$), 1-octadecene, and 9-nitroanthracene were purchased from Aldrich. 95% sodium oleate, diphenyl ether, and oleyl alcohol were purchased from TCI. Acetone, *n*-hexane, and chloroform ($CHCl_3$) were purchased from Samchun Chem.

3.2.2. Synthesis of small-sized iron oxide nanoparticles

Extremely small-sized iron oxide nanoparticles were prepared following heat-up process.[12] Iron-oleate complexes had been prepared by reacting sodium oleate and iron(III) chloride hexahydrate.[10] For the synthesis of 3.1 nm nanoparticles, iron-oleate complex (1.8 g; 2 mmol), oleic acid (0.57 g; 2 mmol), and oleyl alcohol (1.61 g; 6 mmol) were dissolved in diphenyl ether (10 g) at room temperature. The mixture was heated to a 250 ^{o}C at a heating rate of 10 ^{o}C/min, and then kept for 30 min under Ar atmosphere. After the reaction, the reaction vessel was rapidly cooled to room temperature and washed by adding 5 mL of *n*-hexane and 50 mL of acetone. The nanocrystals were washed twice and dispersed in 10 mL of chloroform. To obtain 2.0 nm-

sized nanoparticles, iron-oleate complex (1.8 g; 2 mmol) and oleyl alcohol (3.22 g; 12 mmol) were dissolved in diphenyl ether (10 g). The mixture was heated to 250 ^{o}C at heating rate of 10 ^{o}C/min, and then kept at that temperature for 30 min. The washing step was same as the 3.1 nm scheme. When the aging was performed at 200 ^{o}C, 1.5 nm nanoparticles were generated. To obtain 3.8 nm-sized nanoparticles, iron-oleate complex (1.8 g; 2 mmol), oleic acid (0.57 g; 2 mmol), and oleyl alcohol (1.61 g; 6 mmol) were dissolved in 1-octadecene (10 g). The mixture was heated to 280 ^{o}C at heating rate of 10 ^{o}C/min, and then kept at that temperature for 30 min. The 3 nm iron oxide nanocrystals shown in Figure 3.11 were synthesized by thermal decomposition of iron-oleate complex (0.9 g; 1 mmol) in the presence of oleic acid (0.57 g; 2 mmol) and oleyl alcohol (1.61 g; 6 mmol) in diphenyl ether (10 g) at 250 °C for 30 min.

Extremely small-sized iron oxide nanoparticles were also obtained in the absent of oleyl alcohol. iron-oleate complex (1.8 g; 2 mmol) and oleic acid (0.57 g; 2 mmol) were dissolved in 1-octadecene (10 g). The mixture was heated to 300 ^{o}C at heating rate of 3.3 ^{o}C/min. When the reaction mixture was aged for 30 min and 35 min, 1.3 nm and 2.5 nm nanoparticles were synthesized, respectively. When the mixture was heated to 320 ^{o}C at heating

rate of 10 ^{o}C/min, and aged at that temperature for 30 min, 4.3 nm nanoparticles were obtained.

3.2.3. Characterization with MALDI-TOF MS

MALDI-TOF MS was performed on a Voyager-DE^{TM} STR Biospectrometry Workstation manufactured by Applied Biosystems Inc. in National Center for inter-University Research Facilities 9-nitroanthracene was used as a matrix. We used a standard sample preparation protocol for MALDI-TOF MS. Nanoparticle dispersion in chloroform (10 mg/mL) and 9-nitroanthracene solution in chloroform (10 mg/mL) were prepared. The nanoparticle dispersion and the 9-nitroanthracene matrix solution were mixed together by pipetting (1:1 volume ratio). 2 μL of the mixture was taken and spotted onto a target plate. Upon evaporation of the solvent, the nanoparticles are well-dispersed in the matrix. Desorption and ionization of the nanoparticles were achieved by absorbing pulsed nitrogen laser (337 nm, 3 ns pulses). The spectra were measured with the laser between 40% and 50% full power. After desorption, a 20 kV potential accelerated the ions into a 2.0 m flight tube (linear mode), which yielded a resolution of 3-5 *m*/*z* in the mass spectrum. The mass spectrum was smoothed with simple average of 100 data point.

3.2.4. Nanoparticle characterization

Iron oxide nanoparticles were analyzed using JEOL-2010 electron microscopes. Powder X-ray diffraction (XRD) pattern was collected with a Rigaku D/Max-3C diffractometer, equipped with a Cu Kα radiation source (λ = 0.15418 nm). Fourier transform infrared (FT-IR) spectra were obtained with a JASCO FT/IR 200. Thermogravimetric analysis (TGA) was performed with a Q-5000 IR manufactured from TA Instrument. Optical absorption was characterized using a JASCO V-550 UV-VIS spectrometer. Magnetic studies were carried out using a Vibrating Sample Magnetometer (VSM) equipped within Physical Property Measurement System (PPMS®) manufactured by Quantum Design.

3.2.5. Tracking growth mechanism

GM3: iron-oleate complex (1.8 g; 2 mmol), oleic acid (0.57 g; 2 mmol) and oleyl alcohol (1.61 g; 6 mmol) were dissolved in diphenyl ether (10 g) at room temperature. The mixture was heated to a 250 ^{o}C at a heating rate of 10 ^{o}C/min, and then kept for 30 min under inert atmosphere. To study growth mechanism, 0.1 mL of reaction mixture was collected by syringe during the heat-up process. The sample aliquots were washed twice with the

mixed solvent of 1 mL of acetone and 0.1 mL of hexane. The samples were separated by centrifugation and dispersed in 0.1 mL of chloroform.

GM2: iron-oleate complex (1.8 g; 2 mmol) and oleyl alcohol (3.22 g; 12 mmol) of were dissolved in diphenyl ether (10 g) at room temperature. The heat-up and sampling step was same with the **GM3**.

3.3 Result and Discussion

3.3.1 Preparation of Samples

Iron oxide nanoparticles with approximate sizes of 1, 2, 3, and 4 nm were synthesized by the thermal decomposition of iron-oleate complex via the heat-up process (Figure 3.1).[5] As-synthesized nanoparticle product contains not only oleate-stabilized iron oxide nanoparticles but also free oleic acid. Free oleic acid in final product can cause error in TGA, and thus the actual size of nanoparticle can be miscalculated. Consequently, free oleic acid should be removed before the MS analysis. Fourier-transform infrared spectroscopy (FT-IR) of the nanoparticles showed a very weak peak at 1710 cm^{-1} and strong peaks at 1558 and 1444 cm^{-1}, demonstrating that almost all free oleic acid was removed removed and coordinated oleate was remained through the washing process (Figure 3.2).[11b]

XRD patterns of the nanoparticles showd ferrite structure (Figure 3.3a). Based on previous report, small-sized iron oxide nanocrystals are considered as maghemite.[4a,b] UV-visible spectra showed no size-dependent optical properties (Figure 3.3b). The magnetic properties of iron oxide nanoparticles change dramatically according to their size. Nanoparticles of ≤ 2 nm size

exhibited nearly paramagnetic behavior, whereas 3 nm and 4 nm nanoparticles were weakly superparamagnetic (Figure 3.4).

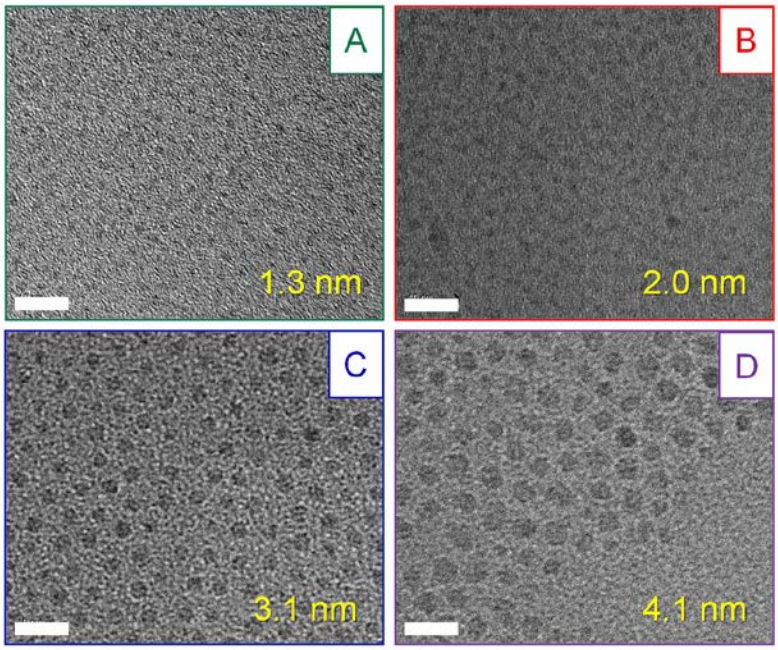

Figure 3.1. TEM images of 1 nm (A), 2 nm (B), 3 nm (C), and 4 nm (D) iron oxide nanoparticles. Scale bar is 10 nm.

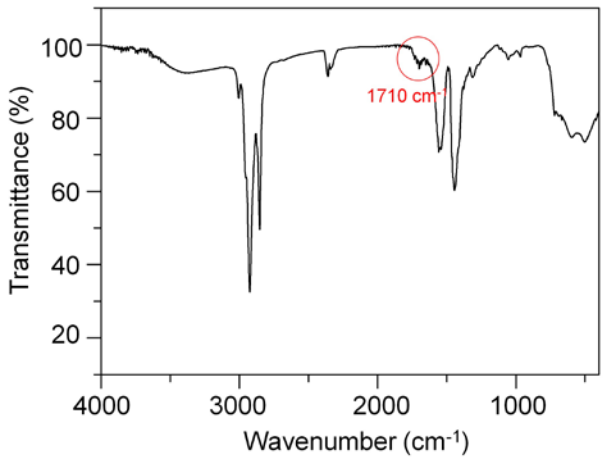

Figure 3.2. FT-IR spectrum of 3 nm iron oxide nanoparticles. The spectra shows a very weak peak at 1710 cm^{-1}, demonstrating that almost all free oleic acid was removed through the washing process.

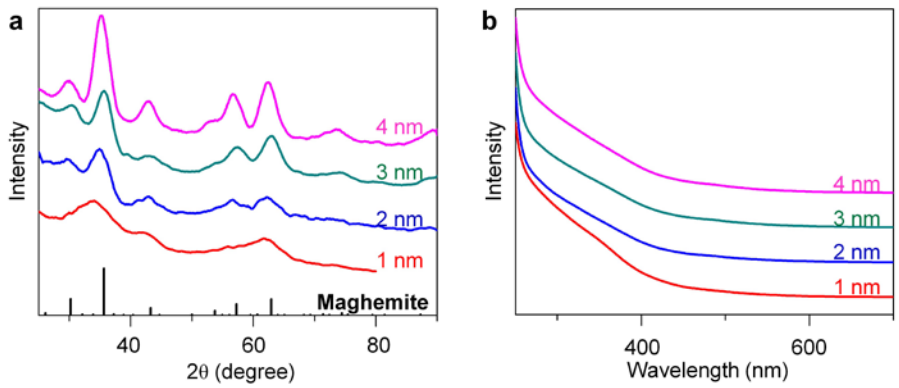

Figure 3.3 (a) XRD patterns, and (b) UV-visible spectra of 1 nm, 2 nm, 3 nm, and 4 nm iron oxide nanoparticles. The XRD patterns revealed the maghemite crystal structure. The UV-visible spectra showed no size-dependent optical properties.

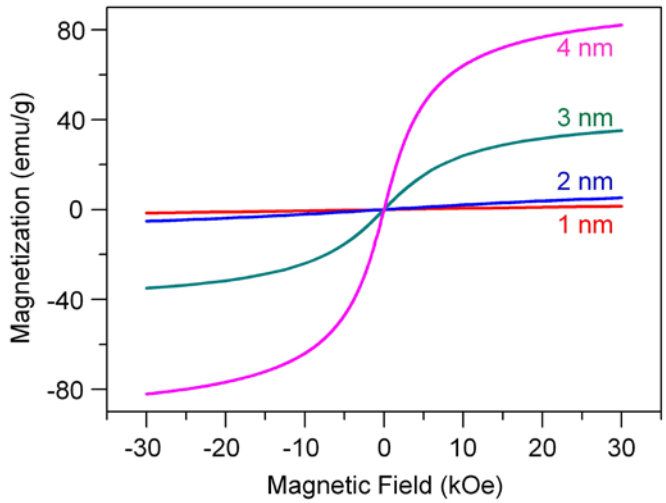

Figure 3.4 Field dependent magnetization curves (M-H) of 1 nm, 2 nm, 3 nm, and 4 nm iron oxide nanoparticles measured at room temperature. The iron oxide nanoparticles showed highly size-dependent magnetic property. 1 nm and 2 nm iron oxide nanoparticles exhibited nearly paramagnetic behavior, whereas 3 nm and 4 nm nanoparticles were weakly superparamagnetic.

3.3.2 Estimating Size of Extremely Small-sized Iron Oxide Nanoparticles by MALDI-TOF MS

To obtain highly resolved mass spectra of iron oxide nanoparticles, it is important to select an appropriate matrix. Aromatic carboxylic acids, which are the most popular matrix for MALDI-TOF MS, are inappropriate for the desorption and ionization of the iron oxide nanoparticles due to their reactivity with the iron oxide. Instead, non-acidic 9-nitroanthracene was used as the matrix. It enables the generation of intact iron oxide nanoparticle ions taking advantage of its minimal interaction and excellent miscibility with the hydrophobic nanoparticles. Using 9-nitroanthracene as a matrix, we successfully obtained MALDI-TOF mass spectra with the peak positions at 9.2, 23, 82, and 135 kDa for 1, 2, 3, and 4-nm nanoparticles, respectively (Figure 3.5), with the commonly used measurement procedure.

Since a single nanoparticle consists of both an inorganic core and an organic surfactant, its total mass can be written as $\boldsymbol{M} = \boldsymbol{M}_{\text{core}} + \boldsymbol{M}_{\text{ligand}}$, where $\boldsymbol{M}_{\text{core}}$ and $\boldsymbol{M}_{\text{ligand}}$ are the mass of the core and ligand parts, respectively. To determine the size of the inorganic core, the core mass fraction ($f = \boldsymbol{M}_{\text{core}}/\boldsymbol{M}$) was measured by thermogravimetric analysis (TGA) (Figure 3.6). The mass ratio of the sample mass before and after heating was taken as the core mass fraction because organic surfactants on the nanoparticles were assumed to be

totally removed by heating at 600 °C in air.[12] The diameter (***D***) of the spherical particles is determined from the total mass (***M***) directly obtained using MALDI-TOF spectra by the following equation;

$$\boldsymbol{D} = \sqrt[3]{\frac{6\boldsymbol{M}f}{\rho N_{\mathrm{A}}\pi}} \qquad \text{(Eq. 3.1)}$$

where ρ is density of the core (= 4.87×10^{-21} g nm^{-3} for maghemite),[13] and N_{A} is Avogadro's number (mol^{-1} = Da g^{-1}).

Given that the mass fraction of nanocrystals of 9.2 kDa was 0.35, the particle size calculated using eq 1 was 1.28 nm. This value is very close to the mean size measured by the TEM image (1.27 nm ± 0.22 nm; Figure 3.4). The diameters of nanocrystals of 23, 82, and 135 kDa were calculated to be 1.96, 3.28, and 3.91 nm (Figure 3.5), respectively, which also matched well with those values from TEM images (1.97 ± 0.37, 3.05 ± 0.63, and 4.13 nm ± 0.70 nm, respectively; Figure 3.5).

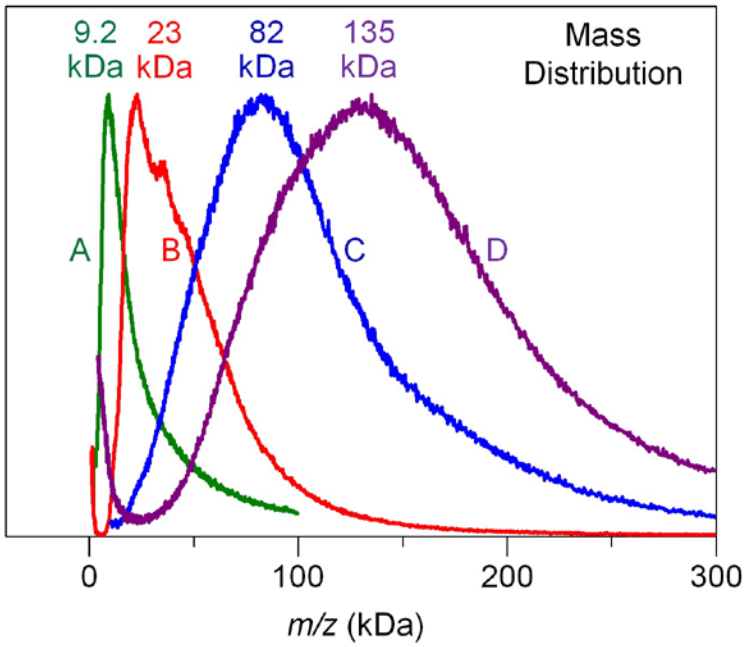

Figure 3.5 MALDI-TOF mass spectra of iron oxide nanoparticles shown in Figure 3.4.

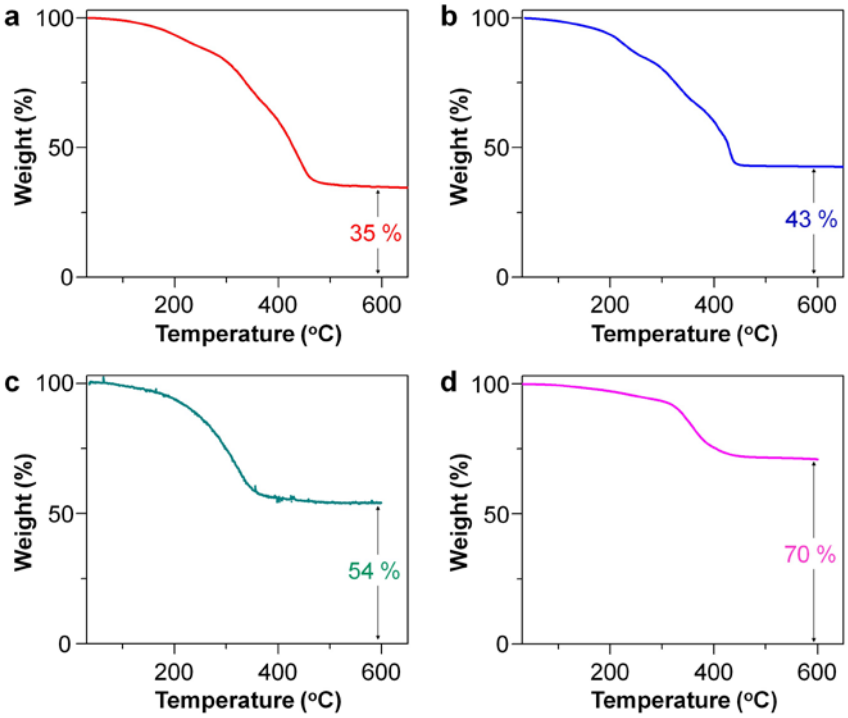

Figure 3.6 TGA data of (a) 1, (b) 2, (c) 3, and (d) 4 nm iron oxide nanoparticles.

3.3.3 Mass-to-size Estimation Method by Using Simple Equation

3.3.3.1 Derivation of Equation for Mass-to-size Estimation

Up to now, we suggested the size estimation method, which required not only mass data by MALDI-TOF but also core fraction data by TGA. To reduce the time-consuming TGA measurement, we aimed to devise mass-to-size conversion equation not containing core fraction (*f*) term. Then we expected to estimate size of nanoparticles from mass data directly through equation.

The total mass (***M***) is denoted as sum of core and ligand mass as follows

$$\boldsymbol{M} = \boldsymbol{M}_{\text{core}} + \boldsymbol{M}_{\text{ligand}} \qquad \text{(Eq. 3.2)}$$

The $\boldsymbol{M}_{\text{core}}$ is the product of density and volume, and the $\boldsymbol{M}_{\text{ligand}}$ is the product of surface density of ligand and molecular mass of ligand and surface area. Assuming that the particles is spherical, total mass of nanoparticle is expressed as the third order formula with respect to the diameter as follows:

$$\boldsymbol{M} = \frac{\rho N_{\text{A}} \pi \boldsymbol{D}^3}{6} + \sigma m \pi \boldsymbol{D}^2 = a\boldsymbol{D}^3 + b\boldsymbol{D}^2 \qquad \text{(Eq. 3.3)}$$

where ρ is density of the core (= 4.87×10^{-21} g nm^{-3} for maghemite), N_{A} is Avogadro's number (= 6.022×10^{-23} mol^{-1} = Da g^{-1}), ***D*** is diameter of the nanoparticles (nm), σ is surface number density of ligand (nm^{-2}), and *m* is molecular mass of ligand (281.5 Da for oleate). All of the coefficients except

σ were known. Assuming that surface number density of ligand (σ) is constant, σ can be derived by the data set of core mass fraction.

Core fraction (f) was represented as $\boldsymbol{M}_{\text{core}}/\boldsymbol{M}$:

$$f = \frac{\boldsymbol{M}_{\text{core}}}{\boldsymbol{M}} = \frac{\frac{\rho N_{\text{A}} \pi \boldsymbol{D}^3}{6}}{\frac{\rho N_{\text{A}} \pi \boldsymbol{D}^3}{6} + \sigma m \pi \boldsymbol{D}^2} \qquad \text{(Eq. 3.4)}$$

Taking the reciprocal of both sides, we can obtain the following:

$$\frac{1}{f} = \frac{6\sigma m}{\rho N_{\text{A}} \boldsymbol{D}} + 1 \qquad \text{(Eq. 3.5)}$$

The coefficient σ deduced from the slope of f^{-1} (measured by TGA) versus $\boldsymbol{D}^{-1}$ (measured by TEM) plot was 3.93 nm^{-2} (Figure 3.7), which is well agreed with the reported value, 3.8 nm^{-2}.[14]

Substituted the σ value, the third- and second-order coefficient (a and b, respectively) of $\boldsymbol{D}$ are obtained: $a = 1.54 \times 10^3$ $\text{Da}\cdot\text{nm}^{-3}$, $b = 3.46 \times 10^3$ $\text{Da}\cdot\text{nm}^{-2}$.

$$\boldsymbol{M} = \frac{\rho N_{\text{A}} \pi \boldsymbol{D}^3}{6} + \sigma m \pi \boldsymbol{D}^2 = a\boldsymbol{D}^3 + b\boldsymbol{D}^2 \qquad \text{(Eq. 3.6)}$$

The Eq. 3.6 is rearranged as follows.

$$a\boldsymbol{D}^3 + b\boldsymbol{D}^2 - \boldsymbol{M} = 0 \qquad \text{(Eq. 3.7)}$$

The cubic equation with respect to $\boldsymbol{D}$ can be solved using Cardano's method. We reduced the Eq. 3.7 by substituting $\boldsymbol{D}$ with ($t - b/3a$) to obtain a depressed cubic equation.

$$a\left(t-\frac{b}{3a}\right)^3+b\left(t-\frac{b}{3a}\right)^2-\boldsymbol{M}=0 \qquad \text{(Eq. 3.8)}$$

The equation was rearranged in the descending order of *t*.

$$t^3-\frac{b^2}{3b}t+\frac{2b^3}{27a^2}-\boldsymbol{M}=0 \qquad \text{(Eq. 3.9)}$$

To facilitate the calculation of the cubic equation, coefficients in Eq. 3.9 are substituted with *p* and *q*:

$$t^3+pt+q=0 \qquad \text{(Eq. 3.10)}$$

where $p = -b^2/3a$ and $q = 2b^3/27a^2 - \boldsymbol{M}$.

Variable *t* was denoted as sum of two variables (*u* and *v*), which satisfies the condition:

$$uv=-\frac{p}{3} \qquad \text{(Eq. 3.11)}$$

Eq. 3.10 was rearranged with respect to *u* and *v*.

$$(u+v)^3-3uv(u+v)+q=0 \qquad \text{(Eq. 3.12)}$$

By fabricating Eq. 3.11 and 1.12, we obtain Eq. 3.13 and 1.14, respectively.

$$u^3v^3=-\frac{p^3}{27} \qquad \text{(Eq. 3.13)}$$

$$u^3+v^3=-q \qquad \text{(Eq. 3.14)}$$

Solving the simultaneous equation for u^3 and v^3, we obtaine:

$$u^3 = -\frac{p}{2} + \sqrt{\frac{q^2}{4} + \frac{p^3}{27}} \qquad \text{(Eq. 3.15)}$$

$$v^3 = -\frac{p}{2} - \sqrt{\frac{q^2}{4} + \frac{p^3}{27}} \qquad \text{(Eq. 3.16)}$$

Since t is sum of u and v, we get

$$t = u + v = \sqrt[3]{-\frac{p}{2} + \sqrt{\frac{q^2}{4} + \frac{p^3}{27}}} + \sqrt[3]{-\frac{p}{2} - \sqrt{\frac{q^2}{4} + \frac{p^3}{27}}} \qquad \text{(Eq. 3.17)}$$

$$\boldsymbol{D} = t - \frac{b}{3a} = -\frac{b}{3a} + \sqrt[3]{-\frac{p}{2} + \sqrt{\frac{q^2}{4} + \frac{p^3}{27}}} + \sqrt[3]{-\frac{p}{2} - \sqrt{\frac{q^2}{4} + \frac{p^3}{27}}}$$

(Eq. 3.18)

As the diameter is real number, complex solutions were not needed.

Substituting p with $(-b^2/3a)$ and q with $(2b^3/27a^2 - \boldsymbol{M})$, the solution is written as follows:

$$\boldsymbol{D} = -\frac{b}{3a} + \sqrt[3]{-\frac{b^3}{27a^3} + \frac{1}{2a}\boldsymbol{M} + \sqrt{-\frac{b^3}{27a^4}\boldsymbol{M} + \frac{1}{4a^2}\boldsymbol{M}^2}}$$

$$+ \sqrt[3]{-\frac{b^3}{27a^3} + \frac{1}{2a}\boldsymbol{M} - \sqrt{-\frac{b^3}{27a^4}\boldsymbol{M} + \frac{1}{4a^2}\boldsymbol{M}^2}} \qquad \text{(Eq. 3.19)}$$

For conciseness, we introduce two coefficients, α and β.

$$\boldsymbol{D} = \alpha + \sqrt[3]{\alpha^3 + \beta\boldsymbol{M} + \sqrt{2\alpha^3\beta\boldsymbol{M} + \beta^2\boldsymbol{M}^2}} + \sqrt[3]{\alpha^3 + \beta\boldsymbol{M} - \sqrt{2\alpha^3\beta\boldsymbol{M} + \beta^2\boldsymbol{M}^2}}$$

(Eq. 3.20)

where

$$\alpha = -\frac{b}{3a} = \frac{-2\sigma m}{\rho N_A} \approx -0.754 \text{ (nm)} \qquad \text{(Eq. 3.21)}$$

$$\beta = \frac{1}{2a} = \frac{3}{\rho N_A \pi} \approx 3.25 \bullet 10^{-4} \text{ (nm}^3\text{Da}^{-1}\text{)} \qquad \text{(Eq. 3.22)}$$

Mass-to-diameter conversion data calculated using Eq. 3.20 is provided in Table 3.1 and Figure 3.8.

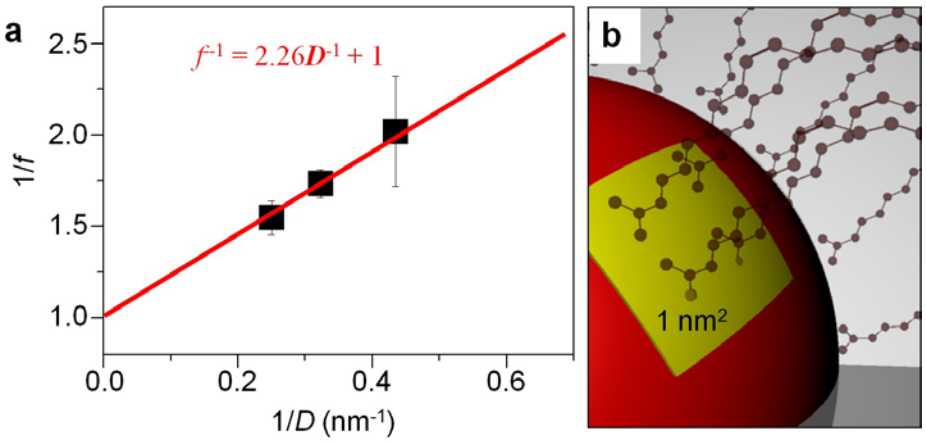

Figure 3.7 (a) Graph indicating the correlation between inverse diameter (1/***D***) and inverse core fraction (1/*f*). The slope was 2.26 nm ± 0.19 nm, approximated by least square analysis. (b) Schematics describing the coordinated ligand on the iron oxide nanoparticle surface with the packing density of ligand of 3.93 nm^{-2}.

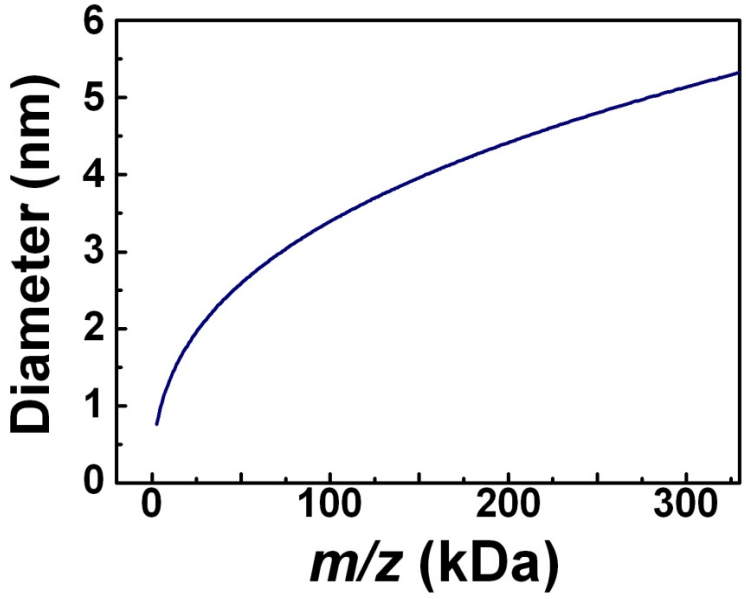

Figure 3.8 Mass-to-size estimation graph depicted from Eq. 3.20.

Mass (kDa)	Calculated Diameter (nm)
10	1.34
20	1.79
30	2.11
50	2.59
70	2.95
100	3.39
150	3.96

Table 3.1. Mass to diameter conversion data calculated from Eq. 3.20.

3.3.3.2 Determination of Sizes and Size Distributions Using Deviced Equation

Mass to diameter conversion data calculated from Eq. 3.20 were listed in Table 3.1 and depicted in Figure 3.8. To obtain the empirical relationship between the mass and the size of the nanoparticles, we prepared nanoparticles of various sizes from 70 batches of different synthetic conditions. The peak positions in the mass spectra were obtained from MALDI-TOF and their mean sizes were measured using TEM. It is difficult to obtain high-quality TEM images of nanocrystals of < 4 nm due to ablation by electron beam and intrinsic uncertainty of TEM. To obtain size distribution data as accurately as possible based on the TEM images, we measured size of each nanocrystal twice and took geometric mean using image J program (NIH). Each size distributions of 70 batches of iron oxide nanocrystals were obtained based on 70-100 particles in their TEM images.

In Figure 3.9, the mass and size data are indicated as red dots. Y-axis values of red dot in Figure 3.9 indicate the modes of the size distributions from TEM image.

Mass-diameter curve calculated with Eq. 3.20 (blue line in Figure 3.9) gives an excellent description of the empirical data. All 70 data sets of mass

spectra and TEM images for the nanoparticles are provided in Figure 3.9 and Table 3.2.

The mass-size relationship can be utilized to determine the size distribution of the nanoparticles in a quick and accurate way. We obtained the size distribution of iron oxide nanoparticles by measuring 807 nanoparticles on a TEM image (Figure 3.11). On the other hand, the mass spectrum of the same nanoparticles can be directly converted to the size distribution by Eq. 3.20. As shown in Figure 3.12, the size distributions from TEM image and the mass spectrum have good resemblance. Mass spectra of polydisperse iron oxide nanocrystals, which were prepared by mixing 1 nm- and 3 nm nanoparticles with various ratios, were obtained (Figure 3.13). As the ratio of 1 nm-sized nanoparticles decreases, 8.3 kDa (1.2 nm calculated by Eq. 3.20) peak continuously decreased simultaneously with a gradual increase in 95 kDa (3.3 nm calculated by Eq. 3.20) peak (Figure 3.14). The results clearly demonstrate that MALDI-TOF MS can be used for the size characterization of polydisperse nanoparticles. Our results clearly show that the mass spectrometry of nanoparticles provides a powerful tool for the fast and accurate determination of the nanoparticle size distribution with the resolution of few angstroms.

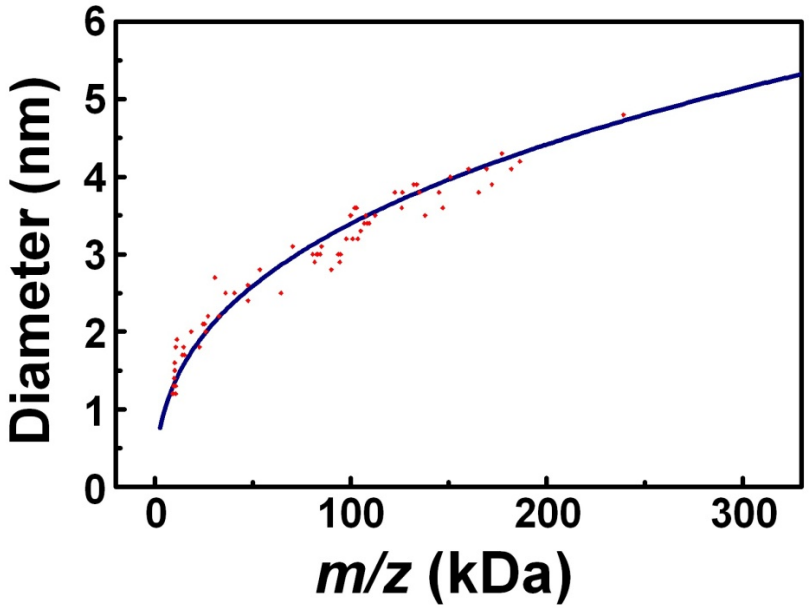

Figure 3.9 The solid blue curve indicates the mass-diameter relationship from Eq. 3.20. The position of each red dot represents the MS peak position (x-axis) and the mean diameter (y-axis) measured from TEM image of iron oxide nanoparticles synthesized from a single batch. There are a total of 70 data points in the plot, which corresponds to 70 batches of the nanoparticles with various sizes.

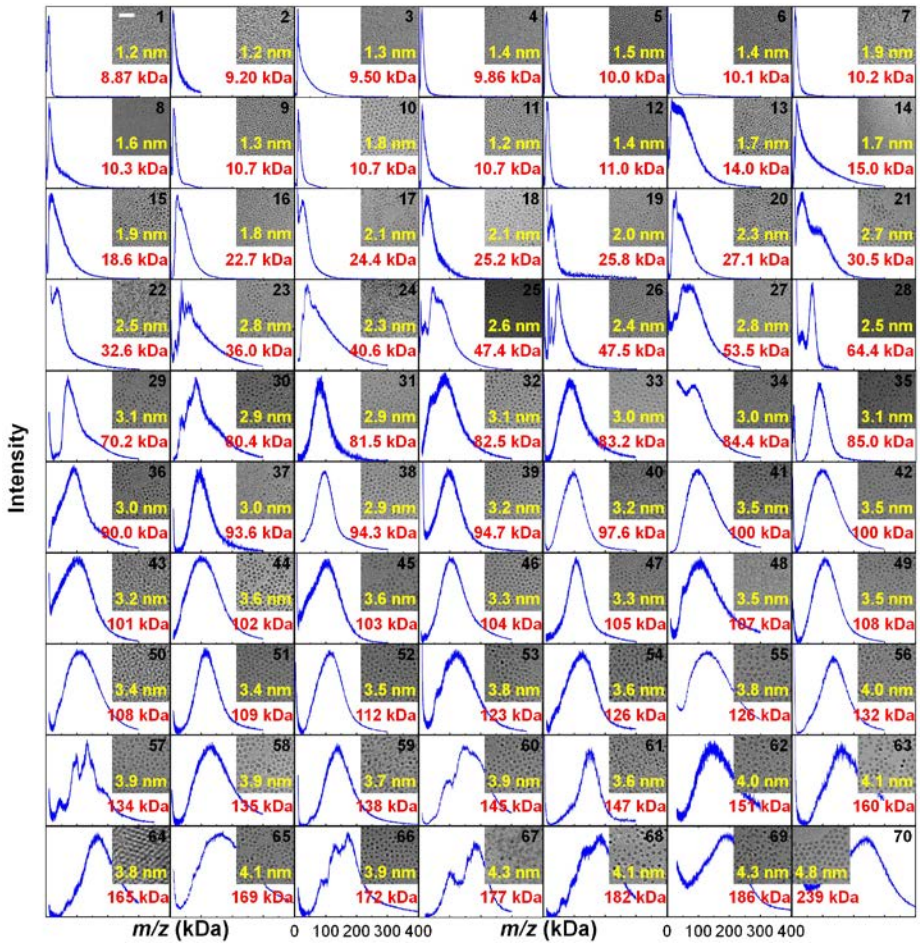

Figure 3.10. A total of 70 MALDI-TOF mass spectra and TEM images of iron oxide nanoparticles from 70 different batches in different synthetic conditions. Scale bar is 20 nm. Red numbers are peak positions from mass spectra and yellow numbers are the mean sizes from TEM images. The results are listed in Table 3.2 and plotted in Figure 3.9.

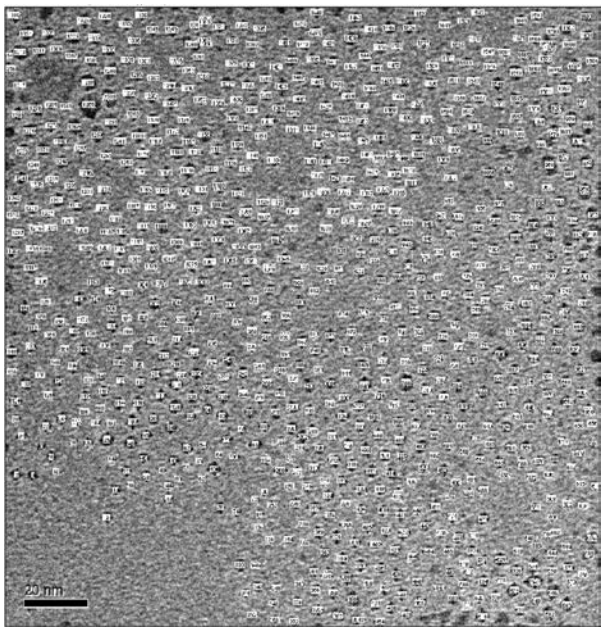

Figure 3.11 Process for obtaining size distribution of 807 particles from TEM image using Image J program (NIH). We measured size twice per each particle. The numbers on the particle represent measuring order. The histogram for size distribution as a result of the process is shown in Figure 3.12.

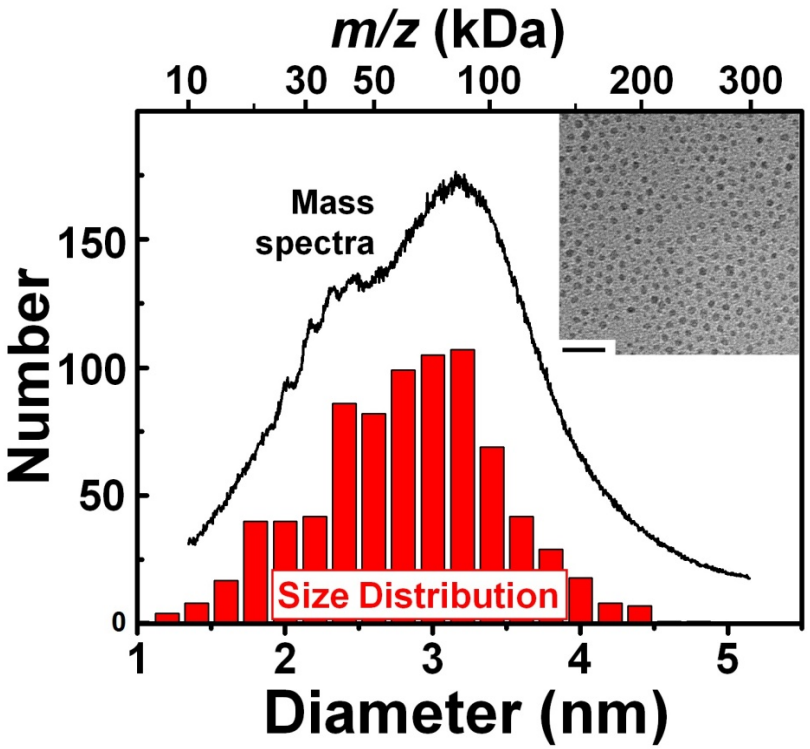

Figure 3.12 (bars) Size distribution of iron oxide nanoparticles measured from the TEM image in Figure 3.11. (line) The size distribution obtained from the mass spectrum of the same nanoparticle sample using Eq. 3.20. (inset) Corresponding TEM image.

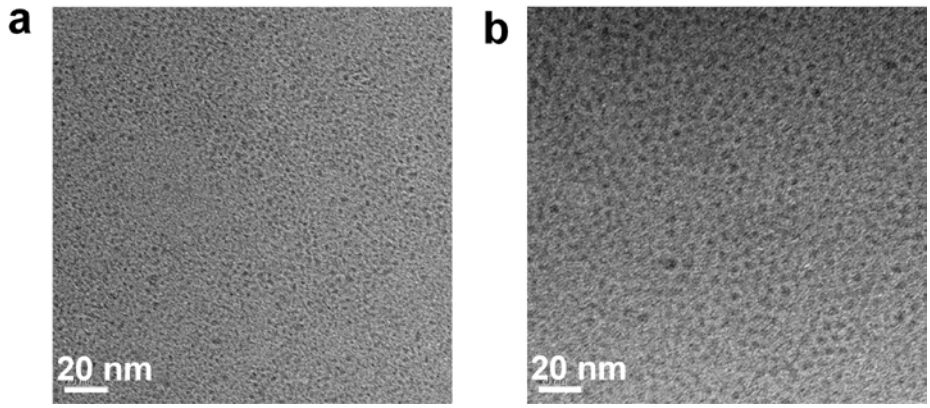

Figure 3.13. TEM images of (a) 1 and (b) 3 nm iron oxide nanoparticles, which were used to prepare polydisperse mixture. Mass spectra of the mixture are shown in Figure 3.14.

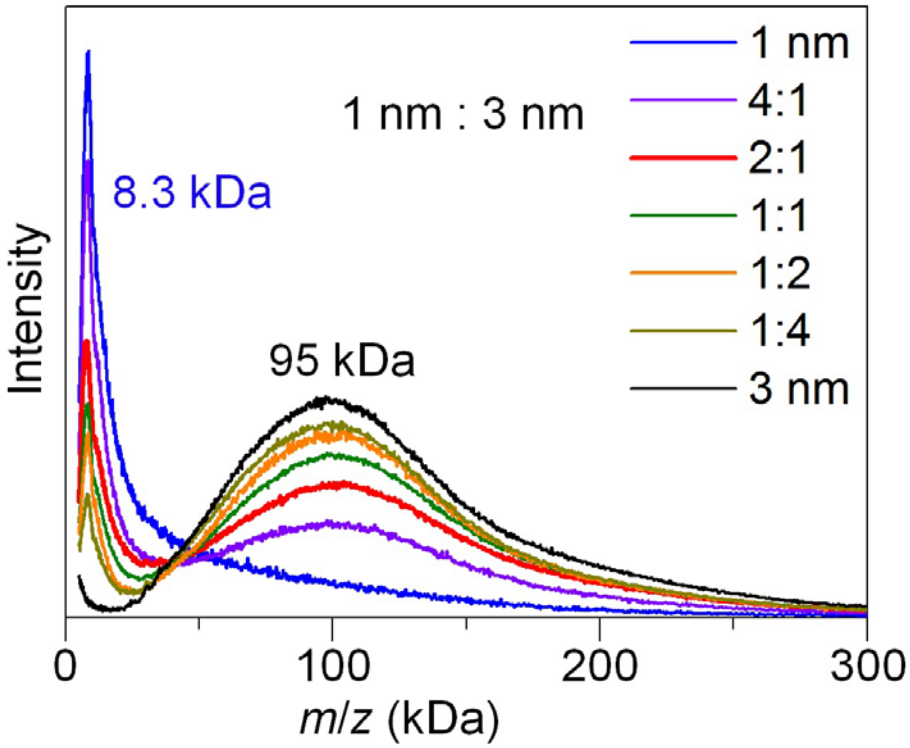

Figure 3.14 MALDI-TOF mass spectra of 1 and 3 nm iron oxide nanoparticles and their mixtures with different ratios of 4:1, 2:1, 1:1, 1:2, 1:4.

#	Mass (kDa)	Size from TEM (nm)	#	Mass (kDa)	Size from TEM (nm)
1	8.87	1.2	36	90.0	2.8
2	9.20	1.2	37	93.6	3.0
3	9.50	1.3	38	94.3	2.9
4	9.86	1.4	39	94.7	3.0
5	10.0	1.5	40	97.6	3.2
6	10.1	1.6	41	99.8	3.5
7	10.2	1.5	42	100	3.5
8	10.7	1.3	43	101	3.2
9	10.7	1.8	44	102	3.6
10	10.7	1.2	45	103	3.6
11	11.3	1.9	46	104	3.2
12	14.0	1.7	47	105	3.3
13	14.6	1.8	48	107	3.4
14	15.0	1.7	49	108	3.5
15	18.6	2.0	50	108	3.4
16	22.7	1.8	51	109	3.4
17	24.4	2.1	52	112	3.5
18	25.2	2.1	53	123	3.8
19	25.8	2.0	54	126	3.6
20	27.1	2.2	55	126	3.8
21	30.5	2.7	56	132	3.9
22	32.6	2.2	57	134	3.9
23	36.0	2.5	58	135	3.8
24	40.6	2.5	59	138	3.5
25	47.4	2.6	60	145	3.8
26	47.5	2.4	61	147	3.6
27	53.5	2.8	62	151	4.0

28	64.4	2.5	63	160	4.1
29	70.2	3.1	64	165	3.8
30	80.4	3.0	65	169	4.1
31	81.5	2.9	66	172	3.9
32	82.5	3.0	67	177	4.3
33	83.2	3.0	68	182	4.1
34	84.4	3.0	69	186	4.2
35	85.0	3.1	70	239	4.8

Table 3.2 The peak of MALDI-TOF mass spectra and the mode sizes of size distribution obtained from TEM images for 70 iron oxide nanoparticles. The mass spectra and TEM images were shown in Figure 3.10.

3.3.3.3 Advantages of the Mass-to-size Estimation Method

The difficulties in characterizing small sized nanoparticles can be overcome with MALDI-TOF MS. First, determining accurate diameter of the particles is enabled by MALDI-TOF MS. In Figure 3.15, a size distribution data obtained form MALDI-TOF mass spectra showed that a batch of iron oxide nanoparticles was composed of 1.7 nm, 2.0 nm, 2.4 nm, 2.5 nm particles. By employing MALDI-TOF MS, it was able to distinguish 0.1 nm differences, where it is difficult to confirm the accurate size of small nanoparticles by utilizing TEM. Because the core mass is proportional to the cube of the diameter, mass data were much more sensitive than diameter data.

Second, it is easy to obtain the size distribution by employing MALDI-TOF MS, as shown in Figure 3.7. The tedious manual process (counting 807 particles, measuring 1614 times) of obtaining the size distribution from the TEM image can be reduced simply by employing MALDI-TOF MS. Moreover, the resolution of the size distribution converted from MALDI-TOF mass spectra is high. Figure 3.13 showed that the particles, which were considered as uniform in TEM image, were indeed polydisperse based on the mass spectrum.

In addition, sub-nanometer sized clusters can be characterized by

MALDI-TOF MS. (Figure 3.16) Furthermore, data acquisition time with MALDI-TOF MS is 30 times faster than that with TEM.

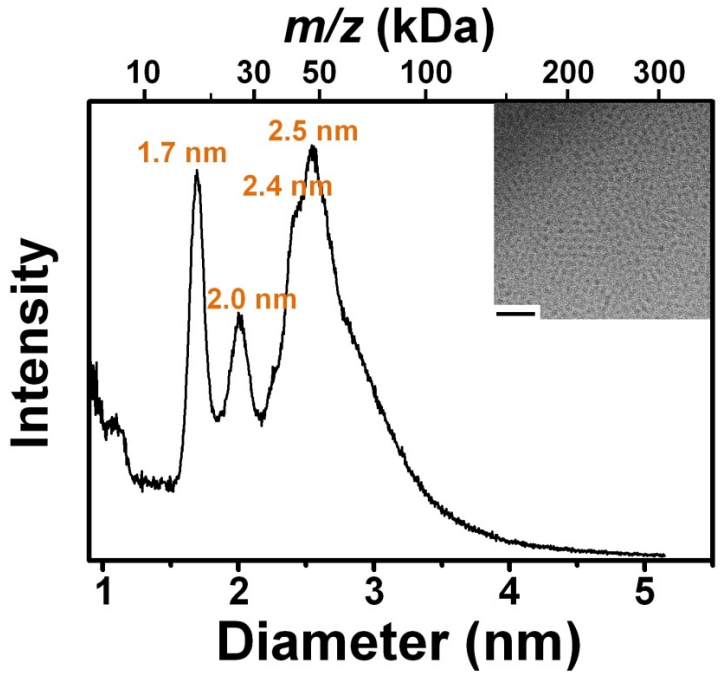

Figure 3.15 Size distribution converted from MALDI-TOF mass spectra of polydisperse iron oxide nanoparticles and (inset) corresponding TEM image. (Scale bar: 20 nm)

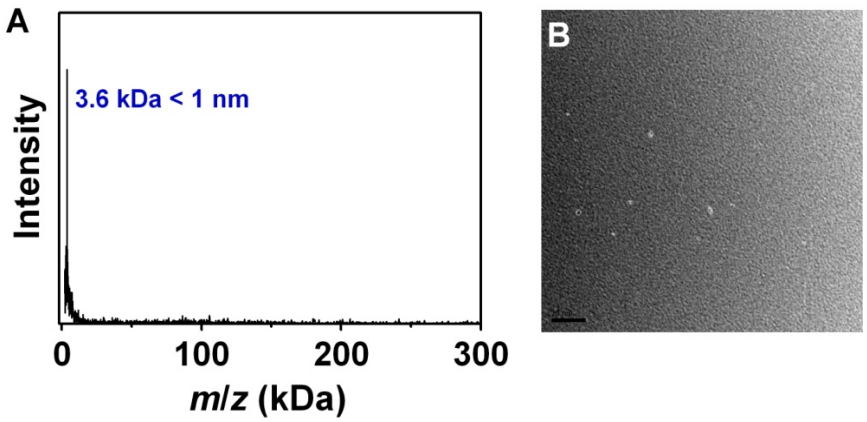

Figure 3.16 (a) MALDI-TOF mass spectra of sub-nanometer clusters and (b) TEM image. Scale bar is 20 nm.

3.3.3.4 Generalization of the Mass-to-size Estimation Method

We obtained mass spectra of various nanoparticles by utilizing MALDI-TOF MS. The mass data of small-sized FePt, manganese oxide, nickel, and gold nanoparticles were measured, and well-matched with TEM images (Figure 3.17).

The mass-to-size estimation equation (Eq. 3.20) can also applied non-spherical nanoparticles. Because it is very difficult to synthesize anisotropic extremely-small-sized iron oxide nanoparticles, we made anisotropic model nanoparticles and compared with spherical nanoparticles. Since iron oxide has face-centered-cubic (fcc) structure, we modeled cubic- or octahedral-shaped nanoparticles (Figure 3.18).

① Cubic shaped nanoparticles

The total mass (***M***) is denoted as the sum of the core and ligand masses as follows:

$$\boldsymbol{M} = \boldsymbol{M}_{\text{core}} + \boldsymbol{M}_{\text{ligand}} \qquad \text{(Eq. 3.23)}$$

The $\boldsymbol{M}_{\text{core}}$ is the product of density and volume, and the $\boldsymbol{M}_{\text{ligand}}$ is the product of packing density of ligand and molecular mass of ligand and surface area.

$$\boldsymbol{M} = \rho N_{\text{A}} (2h)^3 + \sigma m \cdot 6 \cdot (2h)^2 \qquad \text{(Eq. 3.24)}$$

where *h* is the half of the edge length (intercept of cubic; Figure 3.18a). It is necessary to convert edge length to average diameter in order to compare the

equation of spherical particles. We calculated root mean square radius instead of mean radius because calculation of average diameter of cube is extremely arduous.

$$\boldsymbol{D} \approx 2\sqrt{\langle \boldsymbol{r} \rangle^2} \qquad \text{(Eq. 3.25)}$$

We calculated root mean square radius of top face of cube (blue color in Figure 3.18a).

$$\sqrt{\langle \boldsymbol{r} \rangle^2} = \sqrt{\frac{\int_{-h}^{h}\int_{-h}^{h} \boldsymbol{r}^2 \boldsymbol{dxdy}}{\int_{-h}^{h}\int_{-h}^{h} \boldsymbol{dxdy}}} = \sqrt{\frac{\int_{-h}^{h}\int_{-h}^{h} \left(\sqrt{\boldsymbol{x}^2 + \boldsymbol{y}^2 + \boldsymbol{h}^2}\right)^2 \boldsymbol{dxdy}}{\int_{-h}^{h}\int_{-h}^{h} \boldsymbol{dxdy}}} \qquad \text{(Eq. 3.26)}$$

$$2\sqrt{\langle \boldsymbol{r} \rangle^2} = 2\sqrt{\frac{5}{3}}\boldsymbol{h} \approx \boldsymbol{D} \qquad \text{(Eq.3.27)}$$

The result can be regarded as root mean square radius of the cube as six faces of cube are equivalent. Putting the Eq. 3.27 into Eq. 3.24, the total mass of the nanoparticles is expressed as a third order formula with respect to the diameter as follows:

$$\boldsymbol{M} = \left(\frac{3}{5}\right)^{\frac{3}{2}} \rho N_{\mathrm{A}} \boldsymbol{D}^3 + \frac{18}{5}\sigma m \boldsymbol{D}^2 = a\boldsymbol{D}^3 + b\boldsymbol{D}^2 \qquad \text{(Eq. 3.28)}$$

Eq. 3.24 was rearranged using Cardano's method, resulting as follows:

$$\boldsymbol{D} = \alpha + \sqrt[3]{\alpha^3 + \beta\boldsymbol{M} + \sqrt{2\alpha^3\beta\boldsymbol{M} + \beta^2\boldsymbol{M}^2}} + \sqrt[3]{\alpha^3 + \beta\boldsymbol{M} - \sqrt{2\alpha^3\beta\boldsymbol{M} + \beta^2\boldsymbol{M}^2}}$$

(Eq. 3.29)

where

$$\alpha = -\frac{b}{3a} = -\frac{2\sqrt{5}\sigma m}{\sqrt{3}\rho N_{\mathrm{A}}} \approx -0.974 \text{ (nm)} \qquad \text{(Eq. 3.30)}$$

$$\beta = \frac{1}{2a} = \frac{5\sqrt{5}}{6\sqrt{3}\rho N_{\mathrm{A}}} \approx 3.67\times10^{-4} \text{ (nm}^3\text{Da}^{-1}\text{)} \qquad \text{(Eq. 3.31)}$$

② Octahedral-shaped particles

Size-to-mass conversion equation for octahedral nanoparticles was derived by applying a similar procedure as for cubic particles.

The total mass (***M***) is denoted as follow:

$$\boldsymbol{M} = \rho N_{\mathrm{A}} \cdot \frac{4}{3}h^3 + \sigma m \cdot 8 \cdot 2\sqrt{3}h^2 \qquad \text{(Eq. 3.32)}$$

where *h* is the half of the axis length (intercept of Figure 3.18b).

We calculated root mean square radius by taking of one face of octahedron.

$$\sqrt{\langle \boldsymbol{r} \rangle^2} = \sqrt{\frac{\int_0^{\boldsymbol{h}}\int_0^{\boldsymbol{h}-\boldsymbol{y}} \boldsymbol{r}^2 \boldsymbol{dxdy}}{\int_0^{\boldsymbol{h}}\int_0^{\boldsymbol{h}-\boldsymbol{y}} \boldsymbol{dxdy}}} = \sqrt{\frac{\int_0^{\boldsymbol{h}}\int_0^{\boldsymbol{h}-\boldsymbol{y}} \left(\sqrt{\boldsymbol{x}^2+\boldsymbol{y}^2+(\boldsymbol{h}-\boldsymbol{x}-\boldsymbol{y})^2}\right)^2 \boldsymbol{dxdy}}{\int_0^{\boldsymbol{h}}\int_0^{\boldsymbol{h}-\boldsymbol{y}} \boldsymbol{dxdy}}}$$

(Eq. 3.33)

$$2\sqrt{\langle \boldsymbol{r} \rangle^2} = \sqrt{2}\boldsymbol{h} \approx \boldsymbol{D} \qquad \text{(Eq. 3.34)}$$

The result can be regarded as total root mean square radius as the eight faces of octahedron are equivalent. Putting Eq. 3.34 into Eq. 3.32, the total mass of the nanoparticles is expressed as a third order formula with respect to the diameter as follows:

$$\boldsymbol{M} = \frac{\sqrt{2}}{3}\rho N_{\mathrm{A}}\boldsymbol{D}^3 + 2\sqrt{3}\sigma m\boldsymbol{D}^2 = a\boldsymbol{D}^3 + b\boldsymbol{D}^2 \qquad \text{(Eq. 3.35)}$$

Eq. 3.35 was rearranged using Cardano's method, resulting in as follow:

$$\boldsymbol{D} = \alpha + \sqrt[3]{\alpha^3 + \beta\boldsymbol{M} + \sqrt{2\alpha^3\beta\boldsymbol{M} + \beta^2\boldsymbol{M}^2}} + \sqrt[3]{\alpha^3 + \beta\boldsymbol{M} - \sqrt{2\alpha^3\beta\boldsymbol{M} + \beta^2\boldsymbol{M}^2}}$$

(Eq. 3.36)

where

$$\alpha = -\frac{b}{3a} = -\frac{\sqrt{6}\sigma m}{\rho N_{\mathrm{A}}} \approx -0.924 \text{ (nm)} \qquad \text{(Eq. 3.37)}$$

$$\beta = \frac{1}{2a} = \frac{3}{2\sqrt{2}\rho N_{\mathrm{A}}} \approx 3.62\times10^{-4} \text{ (nm}^3\text{Da}^{-1}\text{)} \qquad \text{(Eq. 3.38)}$$

The solution of size-to-mass conversion equations for cubic (Eq. 3.36), octahedral (Eq. 3.29) and spherical particles (Eq. 3.20) are plotted in Figure 3.19. Although the equations were derived using root mean square radius, the resulting equations for cubic and octahedral particles are very similar to that of spherical particles. Consequence, it is expected that the size-to-mass conversion equation can also be adopted for cubic or octahedral nanoparticles.

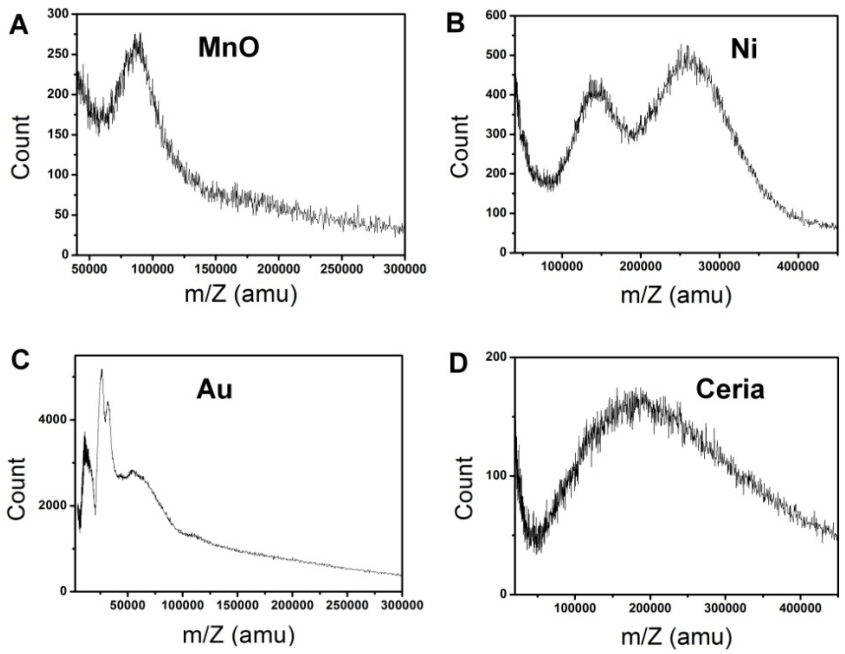

Figure 3.17 MALDI-TOF mass spectra of (a) MnO, (b) Ni, (c) Au, and (d) ceria nanoparticles.

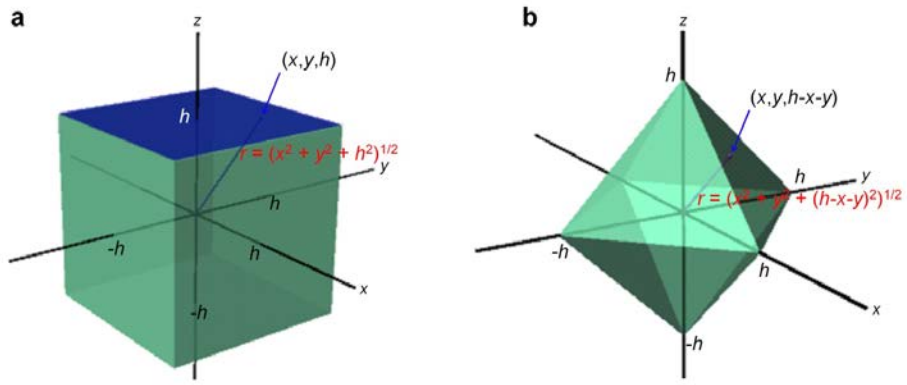

Figure 3.18 (a) Cubic and (b) octahedral model nanoparticles in the rectangular coordinates.

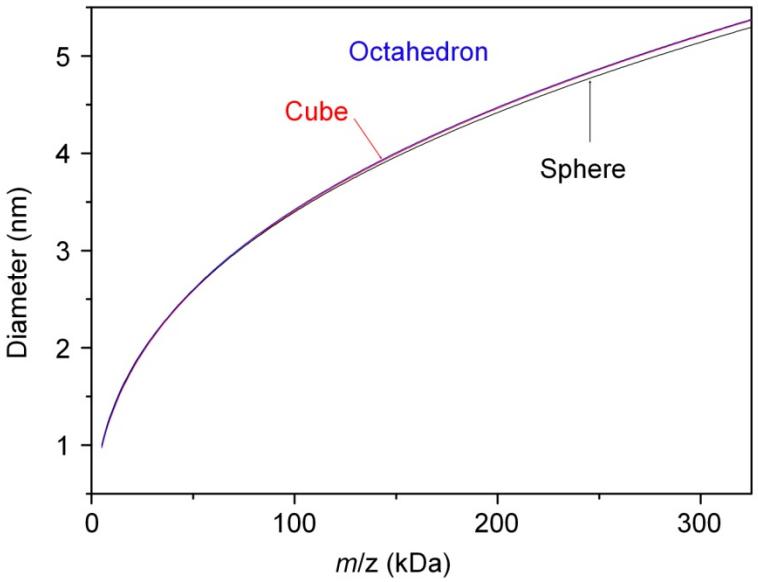

Figure 3.19 Mass-to-size estimation curves for iron oxide nanoparticles with spherical, cubic, and octahedral shapes.

3.3.4 Growth Mechanism

It is important to understand the formation mechanism of nanoparticles in order to exploit the synthesis of desired sized particles and their size distribution. To date, kinetic studies have revealed that the burst nucleation of monomers induced uniform particles on the basis of classical LaMer model. Molecular mechanisms of semiconductor nanoparticles have been investigated by confirming the size-dependent absorption peak. Unlike semiconductor nanoparticles, during the synthesis of metal oxide nanoparticles, it is extremely difficult to monitor the transition from the molecular precursor to the nanoparticles because the nuclei and particles in initial stage are too small to be readily characterized. Our mass spectrum-based size estimation method is very useful especially for the observation of extremely small nanoparticles and clusters. Mass-to-size estimation using MALDI-TOF MS enables us to measure precisely any size changes in range from sub-nanometer to few nanometers, which is unprecedentedly useful technique for the mechanistic study of the nanoparticle formation.

As we wrote in chapter 2 in this thesis, 2.2 nm and 3 nm iron oxide nanoparticless were successfully synthesized by thermal decomposition of iron oleate complex in presence of oleyl alcohol. When the 2 mmol of iron oleate, 2 mmol of oleic acid, and 6 mmol of oleyl alcohol were reacted, 3 nm

iron oxide nanoparticles were synthesized while 2.2 nm particles were obtained through the reaction with 2 mmol of iron oleate and 12 mmil of oleyl alcohol in absence of oleic acid. The growth mechanism of 3 nm and 2.2 nm-sized iron oxide nanoparticles will be referred as **GM3** and **GM2** respectively.

To monitor the formation mechanism, we carried out *ex-situ* measurement on the sample aliquots drawn from the reaction mixture of **GM3** and **GM2** during the heat-up process using MALDI-TOF MS. The mass spectrum data in Figure 3.20 give very important information on the iron oxide nanoparticle formation, **GM3**. Actually, this data clearly show that how iron-oleate precursors were transformed to clusters, and then to the final nanoparticles during heating. At the temperatures higher than 230 °C, the increase in the 3.5 kDa peak intensity indicates that the clusters are produced from iron-oleate complexes and accumulated in the solution. At 250 °C, nucleation takes place from those clusters and some of the larger clusters grow into nanoparticles which are detected at 23 kDa (1.9 nm).[15] During aging at 250 °C, those nanoparticles grow further to 95 kDa (3.3 nm). At 60 min aging, all nanoparticles were grown to 3.3 nm consuming almost all clusters and there is only one peak at 95 kDa in the mass spectrum. Interestingly, the growth of nanoparticles from 1.9 to 3.3 nm is not

continuous (Figure 3.21). Instead, it seems that the size of the nanoparticles was shifted from the small to the large. We think that those 1.9 and 3.3 nm nanoparticles are so-called “magic-sized nanoparticles” that have extra stability with thermodynamically favored structures.[14,15]

In **GM2**, small particles, regarded as nuclei, were begun to form from 200 ^{o}C, based on appearance of 10 kDa (1.4 nm) peak (Figure 3.22). As reaction proceeds, 35 kDa (2.2 nm) and 69 kDa (2.9 nm) peaks increases gradually (Figure 3.22). During **GM2**, there also existed magic size particles, but the nucleation temperature and size distribution were differed from **GM3**. The observed differences may be associated with lack of oleic acid as a surfactant and twice amount of oleyl alcohol as mild reductant. In presence of oleic acid (**GM3**), accumulation of monomers and suppression of nucleation reaction was expected in that the coordination of carboxylic acid is known as monomer stabilizer.[16] On the other hand, in **GM2**, since large portion of monomers were destabilized at nucleation temperature for lack of oleic acid, nucleation reaction was occurred at lower temperature and more nuclei were generated than those in **GM3**. The abundant oleyl alcohol as reaction promoter had a synergistic effect on low nucleation temperature. The fast monomer consuming during **GM2** can be confirmed by disappearance of 3.6 kDa peaks whereas the peaks continued prominent in **GM3**. Generating

smaller sized particles in **GM2** can be explained that more nuclei shares smaller amount of monomers for the growth and the total amount of monomers are small. It was also appeared that the size distribution of nanoparticles became monodisperse during **GM3** (Figure 3.20). In **GM3**, monomers were continuously provided to the small particles, resulting in 'size focusing' during growth stage as early former mechanistic studies suggested. On the other hand, the size distribution became broader during **GM2** due to total consumption of monomers (Figure 3.22). The MALDI-TOF MS data of the iron oxide magic size cluster and particle met the classical nucleation and growth model which was hard to discover using TEM images (Figure 3.23).

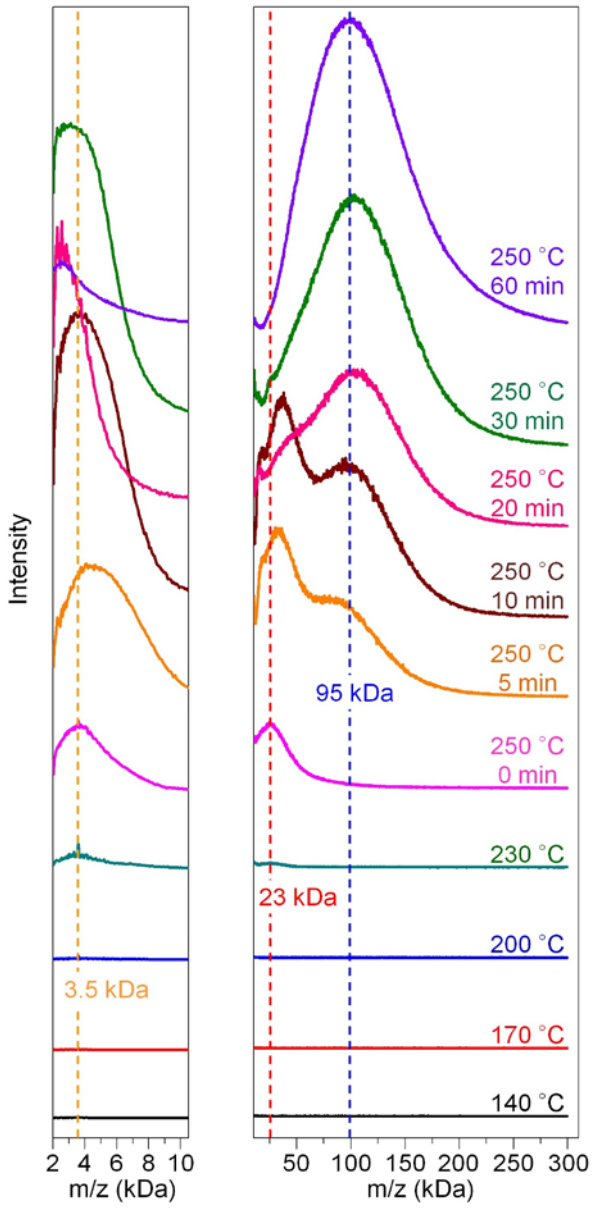

Figure 3.20 MALDI-TOF mass spectra of the sample aliquots drown form **GM3** taken at temperature 140 ^{o}C, 170 ^{o}C, 200 ^{o}C, 230 ^{o}C, 250 ^{o}C at 0 min, 5 min, 10 min, 20 min, 30 min, and 60 min during heating.

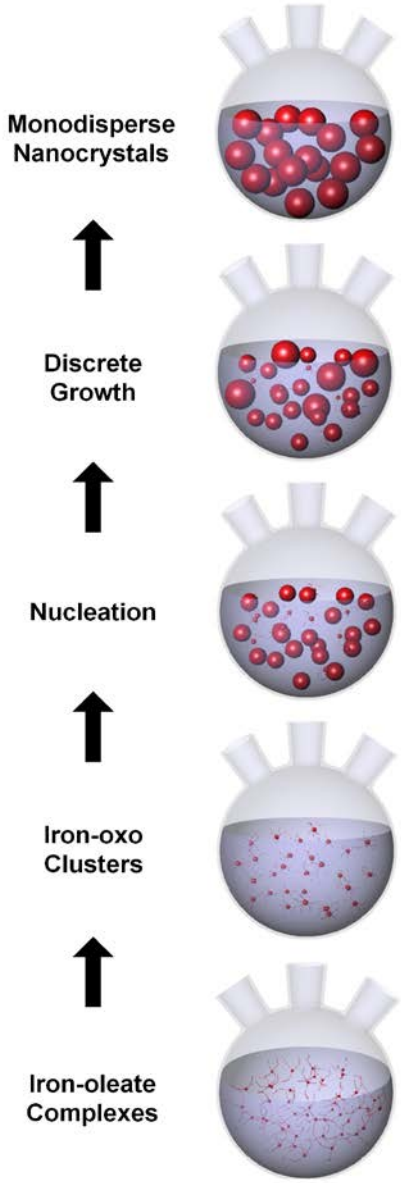

Figure 3.21 Schematics describing the proposed formation mechanism based on the *ex situ* mass spectra measurement.

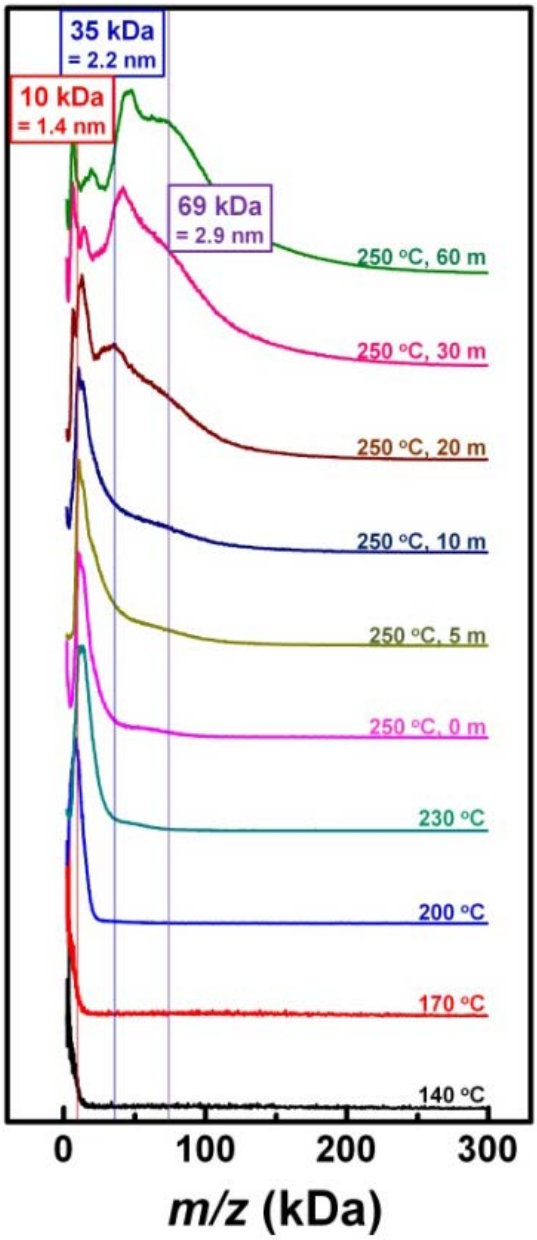

Figure 3.22 MALDI-TOF mass spectra of sample aliquots drown from **GM2** taken at temperature 140 ^{o}C, 170 ^{o}C, 200 ^{o}C, 230 ^{o}C, 250 ^{o}C at 0 min, 5 min, 10 min, 20 min, 30 min, and 60 min during heating.

(a)

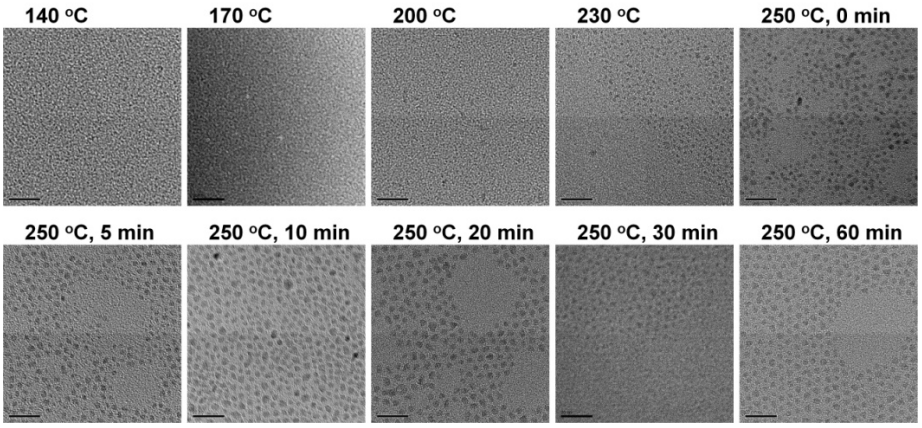

(b)

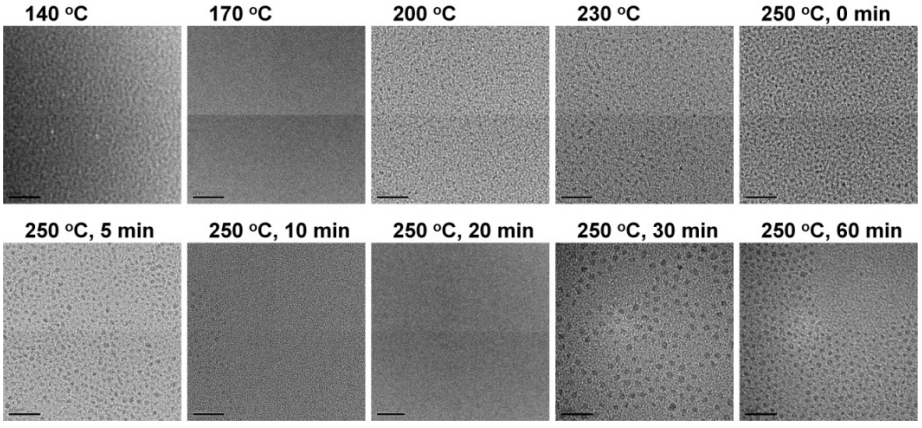

Figure 3.23 TEM images of aliquots drown from (a) **GM3** and (b) **GM2**. Scale bar is 20 nm.

3.4 Conclusion

In conclusion, we demonstrated that MALDI-TOF MS is a powerful technique for the precise measurement of nanoparticle size. Combining the relationship between mass and size of nanoparticles and empirical data, we devised a mass-to-size estimation method, which enabled accurate, reliable, and fast characterization of extremely small-sized iron oxide nanoparticles. We utilized this technique to monitor the formation process of 3-nm iron oxide nanoparticles. *Ex situ* measurements showed that the formation of iron-oxo clusters leads to the nucleation of iron oxide nanoparticles, and that the nanoparticles of only few nanometers grow discretely from the smaller to the larger sizes. We expect that our mass-to-size estimation will be found as easy and accurate analytical tool for various purposes including not only the characterization of size-dependent properties of nanoparticles but also the formation mechanism studies to develop new synthetic methods for various kinds of nanoparticles with desired characteristics.

3.5 References

[1] (a) Murray, C. B.; Norris, D. J.; Bawendi, M. G. *J. Am. Chem. Soc.* **1993**, *115*, 8706. (b) Alivisatos, A. P. *Science* **1996**, *271*, 933. (c) Talapin, D. V.; Lee, J.-S.; Kovalenko, M. V.; Shevchenko, E. V. *Chem. Rev.* **2010**, *110*, 389. (d) Joo, S. H.; Park, J. Y.; Renzas, J. R.; Butcher, D. R.; Huang, W.; Somorjai, G. A. *Nano Lett.* **2010**, *10*, 2709.

[2] Wilcoxon, J. P.; Martin, J. E.; Provencio, P. *J. Chem. Phys.* **2001**, *115*, 998.

[3] Cullity, B. D.; Stock, S. R. *Element of X-Ray Diffraction*, 3rd Ed.; Prentice Hall: New York, **2001**. (b) Grabs, I.-M.; Bradtmöller, C.; Menzel, D.; Garnweitner, G. *Cryst. Growth Des.* **2012**, *12*, 1499. (c) Saunders, A. E.; Sigman Jr., M. B.; Korgel, B. A. *J. Phys. Chem. B* **2004**, *108*, 193. (b) Grabs, I.-M.; Bradtmöller, C.; Menzel, D.; Garnweitner, G. *Cryst. Growth Des.* **2012**, *12*, 1499. (c) Saunders, A. E.; Sigman Jr., M. B.; Korgel, B. A. *J. Phys. Chem. B* **2004**, *108*, 193.

[4] (a) Park, J.; An, K.; Hwang, Y.; Park, J.-G.; Noh, H.-J.; Kim, J.-Y.; Park, J.-H.; Hwang, N.-M.; Hyeon, T. *Nat. Mater.* **2004**, *3*, 891. (b) Sun, S.; Zeng, H. *J. Am. Chem. Soc.* **2002**, *124*, 8204. (c) Jun, Y.-w.; Huh, Y.-M.; Choi, J.-s.; Lee, J.-H.; Song, H.-T.; Kim, S.; Yoon, S.; Kim, K.-S.; Shin, J.-S.; Suh, J.-S.; Cheon, J. *J. Am. Chem. Soc.* **2005**, *127*, 5732. (d) Lee, N.; Hyeon, T. *Chem. Soc. Rev.* **2012**, *41*, 2575. (e) Lee, N.; Kim, H.; Choi, S. H.; Park, M.; Kim, D.; Kim, H.-C.; Choi, Y.; Lin, S.; Kim, B. H.; Jung, H. S.; Kim, H.; Park, K. S.; Moon, W. K.; Hyeon, T. *Proc. Natl. Acad. Sci. U.S.A.* **2011**, *108*, 2662. (f) Park, J.; Lee, E.; Hwang, N.-M.; Kang, M.; Kim, S. C.; Hwang, Y.; Park, J.-G.; Noh, H.-J.; Kim, J.-Y.; Park, J.-H.; Hyeon, T. *Angew. Chem., Int. Ed*. **2005,** *44*, 2872.

[5] Kim, B. H.; Lee, N.; Kim, H.; An, K.; Park, Y. I.; Choi, Y.; Shin, K.; Lee, Y.; Kwon, S. G.; Na, H. B.; Park, J.-G.; Ahn T.-Y.; Kim, Y.-W.; Moon, W. K.; Choi, S. H.; Hyeon T. *J. Am. Chem. Soc.* **2011**, *133*, 12624.

[6] Gatteschi, D.; Fittipaldi, M.; Sangregorio, C.; Sorace, L. *Angew. Chem. Int. Ed.* **2012**, *51*, 4792.

[7] (a) Talapin, D. V.; Rogach, A. L.; Shevchenko, E. V.; Kornowski, A.; Haase, M.; Weller, H. *J. Am. Chem. Soc.* **2002**, *124*, 5782. (b) Peng, X.; Wickham, J.; Alivisatos, A. P. *J. Am. Chem. Soc.* **1998**, *120*, 5343. (c) Peng, Z. A.; Peng, X. *J. Am. Chem. Soc.* **2002**, *124*, 3343. (d) Kudera, S.; Zanella, M.; Giannini, C.; Rizzo, A.; Li, Y.; Gigli, G.; Cingolani, R.; Ciccarella, G.; Spahl, W.; Parak, W. J.; Manna, L. *Adv. Mater.* **2007**, *19*, 548.

[8] Kwon, S. G.; Piao, Y.; Park, J.; Angappane, S.; Jo, Y.; Hwang, N.-M.; Park, J.-G.; Hyeon, T. *J. Am. Chem. Soc.* **2007**, *129*, 12571.

[9] (a) Zheng, H.; Smith, R. K.; Jun, Y.-w.; Kisielowski, C.; Dahmen, U.; Alivisatos, A. P. *Science* **2009**, *324*, 1309. (b) Yuk, J. M.; Park, J.; Ercius, P.; Kim, K.; Hellebusch, D. J.; Crommie, M. F.; Lee, J. Y.; Zettl, A.; Alivisatos, A. P. *Science* **2012**, *336*, 61.

[10] (a) Khitrov, G. A.; Strouse, G. F. *J. Am. Chem. Soc.* **2003**, *125*, 10465. (b) Levi-Kalisman, Y.; Jadzinsky, P. D.; Kalisman, N.; Tsunoyama, H.; Tsukuda, T.; Bushnell, D. A.; Kornberg, R. D. *J. Am. Chem. Soc.* **2011**, *133*, 2976. (c) Whetten, R. L.; Khoury, J. T.; Alvarez, M. M.; Murthy, S.; Vezmar, I.; Wang, Z. L.; Stephens, P. W.; Cleveland, C. L.; Luedtke, W. D.; Landman, U. *Adv. Mater.* **1996,** *8*, 428. (d) Alvarez, M. M.; Khoury, J. T.; Schaaff, T. G.; Shafigullin, M. N.; Vezmar, I.; Whetten, R. L. *J. Phys. Chem. B* **1997,** *101*, 3706. (e) Dass, A.; Stevenson, A.; Dubay, G. R.; Tracy, J. B.; Murray, R. W. *J. Am. Chem. Soc.* **2008**, *130*, 5940. (f) Chaki, N. K.; Negishi, Y.; Tsunoyama, H.; Shichibu, Y.; Tsukuda, T. *J. Am. Chem. Soc.* **2008**, *130*, 8608.

[11] Skoog, D. A.; Holler, F. J.; Nieman, T. A. *Principles of Instrumental Analysis*, 5th ed.; Harcourt College Publishers: Orlando, **1998**.

[12] Qian, H.; Zhu, Y.; Jin, R. *Proc. Natl. Acad. Sci. USA* **2012**, *109*, 696.

[13] Cornell, R. M.; Schwertmann, U. *The Iron Oxides: Structure, Properties, Reactions, Occurrences and Uses*, 2nd Ed.; Wiley-VCH: Weinheim, Germany, 2003.

[14] Viali, W. R.; Alcantara, G. B.; Sartoratto, P. P. C.; Soler, M. A. G.; Mosiniewicz-Szablewska, E.; Andrzejewski, B.; Morais, P. C. *J. Phys. Chem. C* **2010**, *114*, 179.

[15] Sugimoto, T. *Monodispersed particles*; Elsevier: New York, 2001.

[16] van Embden, J.; Mulvaney, P. *Langmuir* **2005,** *21*, 10226.

Bibliography

1. International Publications

1) **Byung Hyo Kim**, Nohyun Lee, Hyoungsu Kim, Kwangjin An, Yong Il Park, Yoonseok Choi, Kwangsoo Shin, Youjin Lee, Soon Gu Kwon, Hyon Bin Na, Je-Geun Park, Tae-Young Ahn, Young-Woon Kim, Woo Kyung Moon, Seung Hong Choi, Taeghwan Hyeon
"Large-scale Synthesis of Uniform and Extremely Small-sized Iron Oxide Nanoparticles for High-resolution T_1 Magnetic Resonance Imaging Contrast Agents"
Journal of American Chemical Society, **2011**, *133*, 12646-12653. (Article)

2) **Byung Hyo Kim**, Kwang Soo Shin, Soon Gu Kwon, Youngjin Jang, Hyun-Seok Lee, Hyunjae Lee, Samuel W. Jun, Jisoo Lee, Sang Yun Han, Yong-Hyeon Yim, Dae-Hyoung Kim, Taeghwan Hyeon*
"Determining size distribution and tracking growth mechanism of iron oxide nanoparticles by mass spectrometry"
Journal of American Chemical Society, Accepted. (Communication)

3) Jeong Ah Kim, Nohyun Lee, **Byung Hyo Kim**, Won Jong Rhee, Sungjun Yoon, Taeghwan Hyeon, Tai Hyun Park
"Enhancement of neurite outgrowth in PC12 cells by iron oxide nanoparticles"

Biomaterials, **2011**, *32*, 2871-2877.

4) In Su Lee, Nohyun Lee, Jongnam Park, **Byung Hyo Kim**, Yong-Weon Yi, Taeuk Kim, Tae Kook Kim, In Hwan Lee, Seung R. Paik, Taeghwan Hyeon
"Ni/NiO core/shell nanoparticles for selective binding and magnetic separation of histidine-tagged proteins"
Journal of American Chemical Society, **2006**, *128*, 10658-10659.

5) Dokyoon Kim, Nohyun Lee, Mihyun Park, **Byung Hyo Kim**, Kwangjin An, Taeghwan Hyeon,
"Synthesis of Uniform Ferrimagnetic Magnetite Nanocubes"
Journal of American Chemical Society, **2009**, *131*, 454-455.

6) Youngjin Jang, Seyoung Kim, Samuel Woojoo Jun, **Byung Hyo Kim**, Sunhwan Hwang, In Kyu Song, B. Moon Kim and Taeghwan Hyeon
"Simple one-pot synthesis of Rh–Fe_3O_4 heterodimer nanocrystals and their applications to a magnetically recyclable catalyst for efficient and selective reduction of nitroarenes and alkenes"
Chemical Communications, **2011**, *47*, 3601-3603.

7) Ji Eun Lee, Dong Jun Lee, Nohyun Lee, **Byung Hyo Kim**, Seung Hong Choi, Taeghwan Hyeon
"Multifunctional Mesoporous Silica Nanocomposite Nanoparticles for pH Controlled Drug Release and Dual Modal Imaging"

Journal of Materials Chemistry, **2011**, *21*, 16869-16872.

8) Jinkyung Park, Soon Gu Kwon, Samuel Woojoo Jun, **Byung Hyo Kim**, Taeghwan Hyeon
"Large-Scale Synthesis of Ultra-Small-Sized Silver Nanoparticles"
ChemPhysChem, **2012**, *13*, 2540-2543.

9) Youngjin Jang, Jooyoung Chung, Seyoung Kim, Samuel Woojoo Jun, **Byung Hyo Kim**, Dong Won Lee, B. Moon Kim and Taeghwan Hyeon
"Simple synthesis of Pd–Fe_3O_4 heterodimer nanocrystals and their application as a magnetically recyclable catalyst for Suzuki cross-coupling reactions"
Physical Chemistry Chemical Physics, **2011**, *13*, 2512-2516

10) Yong Il Park, Yuanzhe Piao, Nohyun Lee, Byeongjun Yoo, **Byung Hyo Kim**, Seung Hong Choi, Taeghwan Hyeon,
"Transformation of hydrophobic iron oxide nanoparticles to hydrophilic and biocompatible maghemite nanocrystals for use as highly efficient MRI contrast agents",
Journal of Materials Chemistry, **2011**, *21*, 11472-11477.

11) Taekyung Yu, Jaewon Moon, Jinkyung Park, Yong Il Park, Hyon Bin Na, **Byung Hyo Kim**, In Chan Song, Woo Kyung Moon, Taeghwan Hyeon,

"Various-Shaped Uniform Mn_3O_4 Nanocrystals Synthesized at Low Temperature in Air Atmosphere",

Chemisty of Materials, **2009**, *21*, 2272-2279.

12) Nohyun Lee, Hye Rim Cho, Myoung Hwan Oh, Soo Hong Lee, Kangmin Kim, **Byung Hyo Kim**, Kwangsoo Shin, Tae-Young Ahn, Jin Woo Choi, Young-Woon Kim, Seung Hong Choi, Taeghwan Hyeon,

"Multifunctional Fe_3O_4/TaO_x Core/Shell Nanoparticles for Simultaneous Magnetic Resonance Imaging and X-ray Computed Tomography"

Journal of American Chemical Society, **2012**, *134*, 10309-10312.

13) Nohyun Lee, Hyoungsu Kim, Seung Hong Choi, Mihyun Park, Dokyoon Kim, Hyo-Cheol Kim, Yoon Seok Choi, Shunmei Lin, **Byung Hyo Kim**, Hye Seung Jung, Hyeonjin Kim, Kyong Soo Park, Woo Kyung Moon, Taeghwan Hyeon,

"Magnetosome-like ferrimagnetic iron oxide nanocubes for highly sensitive MRI of single cells and transplanted pancreatic islets",

Proceeding of the National Academy of Science of the Unisted State of America, **2011**, *108*, 2662-2667.

2. International Conferences

1) Taeghwan Hyeon, **Byung Hyo Kim**, Mihyun Park, Ji Eun Lee
"Large-scale synthesis of uniform-sized nanocrystals and their designed assembly for multifunctional biomedical applications"
240th ACS National Meeitng & Exposition, Boston, MA, USA, August 22-26, 2010.

2) **Byung Hyo Kim**, Taeghwan Hyeon
"Large-scale Synthesis of Uniform and Extremely Small-sized Iron Oxide Nanoparticles for High-resolution T_1 Magnetic Resonance Imaging Contrast Agents"
10th IEEE International Conference on Nanotechonology Joint symposium with NANO KOREA 2010, KINTEX, Goyang, Korea, Aug. 17-20, 2010.

3) **Byung Hyo Kim**, Nohyun Lee, Taeghwan Hyeon
"Large-scale Synthesis of Uniform Extremely Small Iron Oxide Nanoparticles and their Applications to T1 Magnetic Resonance Imaging Contrast Agent"
The 15th Korea-Japan Joint Symposium on Organometallic and Coordination Chemistry for Renewable Energy Research, Jeju, Korea, Oct. 6-8, 2011.

4) **Byung Hyo Kim**, Taeghwan Hyeon
"Synthesis and MRI application of extremely small-sized iron oxide nanoparticles"
SPIE Nanosystems in Engineering and Medicine, Incheon, Korea, Sep. 10-12, 2012

3. Domestic Conference

Byung Hyo Kim, Taeghwan Hyeon

"Large-scale Synthesis of Uniform and Extremely Small-sized Iron Oxide Nanoparticles for High-resolution T_1 Magnetic Resonance Imaging Contrast Agents"

2011 The Korean Society of Industrial and Engineering Chemistry Spring Meeting, ICC Jeju, Jeju, Koera, May 11-13, 2011.

초 록

최근, 3 nm 이하의 작은 크기를 가지는 극소 나노입자가 중요한 물질로 각광받고 있는데, 이는 극소나노입자는 큰 나노입자나 분자와 다른, 독특한 광학적, 자기적, 촉매적 성질을 보이기 때문이다. 극소 나노입자의 물성은 크기에 따라서 크게 변하므로 크기를 정밀하게 조절하는 합성법은 필수적이라고 할 수 있다. 한편, 유용한 자성을 가지는 산화철 나노입자는 매우 중요한 재료이다. 극소 산화철 나노입자는 작은 자성을 가지는데, 이러한 작은 자성이 필요한 분야에 응용될 수 있을 것이다. 이 학위 논문에서는 극소 산화철 나노입자의 합성 분석 및 응용에 관하여 논하였다. 철-올레산 착화합물의 열분해법으로 극소 산화철 나노입자를 합성하였고 T1 자기공명영상(MRI) 조영제로 응용하였다. 말디토프 질량분석법으로 극소 산화철 나노입자의 크기와 크기분포를 정확하게 측정하였다.

첫번째로, 철-올레산 착화합물을 올레일알코올 존재하에 열분해하여 극소산화철 나노입자를 대용량으로 합성하였다. 자기장-자화도 측정 결과, 스핀 기울어짐 효과로 인해 극소 나노입자는 일반적인 나노입자에 비해 훨씬 약한 자화도를 가짐을 확인하였고, 이로 인해 T1 자기공명영상 조영 효과가 나타났다. 극소 산화철 나노입자를 조영제로 사용하여 얻은 T1 생체 영상에서, 강한 T1 신호가 상당히 긴 시간동안 지속되는 것을 볼 수 있다. 이는 극소 산화철

나노입자의 적절한 크기 때문이다. 극소 산화철 나노입자 조영제는 긴 측정시간을 가지므로, 고해상도의 혈관 MRI 영상을 얻을 수 있었다.

둘째로, 질량 분석법으로 극소 산화철 나노입자의 크기 및 크기 분포를 빠르고 신뢰도 있게 얻었다. 나노입자의 질량을 크기로 바꾸는 공식을 유도하였고, 이 공식을 이용해 말디토프 질량분석기로 얻은 질량분포를 크기분포로 변환시켰는데, 이는 TEM으로 얻은 크기분포와 잘 맞았다. TEM 사진으로 크기분포를 얻기 위해 많은 시간과 노력이 필요한 반면, 질량분석기로 크기분포를 얻는 이 방법은 빠르고 간편한 이점이 있다. 또한 질량분석기로부터 얻은 크기분포는 해상도가 높아서 수 옹스트롬의 크기차이도 구분할 수 있었다. 이러한 질량분석법 기술을 이용해 산화철 나노입자의 형성 기작을 분석하였다. 추출실험으로 얻은 질량분포 결과를 보면, 철-올레산 착화합물로부터 철-산소 클러스터가 형성되고 불연속적인 성장을 통해 최종적으로 3 nm 크기의 나노입자가 합성됨을 발견하였다.

주요어: 산화철, 극소 나노입자, 자기공명영상, 질량분석법, 형성 기작

학번: 2006-21331